

AFRL-RQ-WP-TR-2019-0170

NUMERICAL INVESTIGATION OF TURBULENT JUNCTION FLOWS

Zachary D. Robison, John-Paul G. Mosele, and Andreas J. Gross

New Mexico State University
Mechanical and Aerospace Engineering Department

SEPTEMBER 2019
Final Report

DISTRIBUTION STATEMENT A. Approved for public release.
Distribution is unlimited.

STINFO COPY

AIR FORCE RESEARCH LABORATORY
AEROSPACE SYSTEMS DIRECTORATE
WRIGHT-PATTERSON AIR FORCE BASE, OH 45433-7542
AIR FORCE MATERIEL COMMAND
UNITED STATES AIR FORCE

NOTICE AND SIGNATURE PAGE

Using Government drawings, specifications, or other data included in this document for any purpose other than Government procurement does not in any way obligate the U.S. Government. The fact that the Government formulated or supplied the drawings, specifications, or other data does not license the holder or any other person or corporation; or convey any rights or permission to manufacture, use, or sell any patented invention that may relate to them.

This report is the result of contracted fundamental research deemed exempt from public affairs security and policy review in accordance with SAF/AQR memorandum dated 10 Dec 08 and AFRL/CA policy clarification memorandum dated 16 Jan 09. This report is available to the general public, including foreign nationals.

Copies may be obtained from the Defense Technical Information Center (DTIC) (https://discover.dtic.mil/).

AFRL-RQ-WP-TR-2019-0170 HAS BEEN REVIEWED AND IS APPROVED FOR PUBLICATION IN ACCORDANCE WITH ASSIGNED DISTRIBUTION STATEMENT.

*//Signature//

CHRISTOPHER R. MARKS
Work Unit Manager
Turbomachinery Branch

//Signature//

ROLF SONDERGAARD, PhD
Chief, Turbomachinery Branch
Turbine Engine Division

//Signature//

GREGORY S. BLOCH, PhD
Chief Engineer, Turbine Engine Division
Aerospace Systems Directorate

This report is published in the interest of scientific and technical information exchange and its publication does not constitute the Government's approval or disapproval of its ideas or findings.

*Disseminated copies will show "//Signature//" stamped or typed above the signature blocks.

REPORT DOCUMENTATION PAGE

Form Approved
OMB No. 0704-0188

The public reporting burden for this collection of information is estimated to average 1 hour per response, including the time for reviewing instructions, searching existing data sources, gathering and maintaining the data needed, and completing and reviewing the collection of information. Send comments regarding this burden estimate or any other aspect of this collection of information, including suggestions for reducing this burden, to Department of Defense, Washington Headquarters Services, Directorate for Information Operations and Reports (0704-0188), 1215 Jefferson Davis Highway, Suite 1204, Arlington, VA 22202-4302. Respondents should be aware that notwithstanding any other provision of law, no person shall be subject to any penalty for failing to comply with a collection of information if it does not display a currently valid OMB control number. **PLEASE DO NOT RETURN YOUR FORM TO THE ABOVE ADDRESS**.

1. REPORT DATE *(DD-MM-YY)*	2. REPORT TYPE	3. DATES COVERED *(From - To)*
September 2019	Final	25 October 2017 – 13 September 2019

4. TITLE AND SUBTITLE
NUMERICAL INVESTIGATION OF TURBULENT JUNCTION FLOWS

5a. CONTRACT NUMBER
FA8650-17-2-2226

5b. GRANT NUMBER

5c. PROGRAM ELEMENT NUMBER
62201F

6. AUTHOR(S)
Zachary D. Robison, John-Paul G. Mosele, and Andreas J. Gross

5d. PROJECT NUMBER
N/A

5e. TASK NUMBER

5f. WORK UNIT NUMBER
Q1X8

7. PERFORMING ORGANIZATION NAME(S) AND ADDRESS(ES)
New Mexico State University, Mechanical and Aerospace Engineering Department
P.O. Box 30001/MSC 3450
1040 S Horseshoe Street
Las Cruces, NM 88003

8. PERFORMING ORGANIZATION REPORT NUMBER

9. SPONSORING/MONITORING AGENCY NAME(S) AND ADDRESS(ES)
Air Force Research Laboratory
Aerospace Systems Directorate
Wright-Patterson Air Force Base, OH 45433-7542
Air Force Materiel Command
United States Air Force

10. SPONSORING/MONITORING AGENCY ACRONYM(S)
AFRL/RQTT

11. SPONSORING/MONITORING AGENCY REPORT NUMBER(S)
AFRL-RQ-WP-TR-2019-0170

12. DISTRIBUTION/AVAILABILITY STATEMENT
DISTRIBUTION STATEMENT A. Approved for public release. Distribution is unlimited.

13. SUPPLEMENTARY NOTES
PA Clearance Number: 88ABW-2019-6030; Clearance Date: 19 December 2019.

This report contains .pdf attachments related to the research effort. Click the paperclip icon in the left vertical toolbar, and double click the referenced attachment. The file names correspond to numbered publications resulting from grants. For reference items that are not attached, Government personnel may make requests from a military library resource, such as the D'Azzo Research Library at Wright-Patterson Air Force Base, OH.

Some included materials in this report are the result of contracted fundamental research, which is deemed exempt from Public Affairs Office security and policy review in accordance with Deputy Assistant Secretary of the Air Force (Science, Technology, Engineering) (SAF/AQR) memorandum dated 10 Dec 08 and Air Force Research Laboratory Executive Director (AFRL/CA) policy clarification memorandum dated 16 Jan 09.

14. ABSTRACT
Large-eddy simulations for a canonical junction flow geometry (Rood wing) were carried out for a Reynolds number based on approach flow velocity and maximum thickness of 7,000. The mean flow data were in good agreement with particle image velocimetry measurements at Penn State University. Instantaneous flow visualizations reveal a forward and backward motion of the horseshoe vortex and an intermittent loss of coherence. Upstream boundary layer events which were detected with the variable-interval time-averaging method, were found to be correlated with an intermittent strengthening of the horseshoe vortex. To test if the bimodal behavior is correlated with upstream boundary layer events, pulsed disturbances were deliberately introduced upstream of the junction. The correlation between the forced boundary layer events and the circulation of the horseshoe vortex was weak which may be attributed to the chosen forcing method. In addition, simulations with two different circular endwall fillets were carried out. In accordance with the literature, the fillets were found to suppress the bimodal behavior. In summary, the present results support earlier research that suggests that the bimodal behavior is triggered by upstream boundary layer events.

15. SUBJECT TERMS turbulent junction flow, large-eddy simulation, bimodal behavior, active and passive flow control

16. SECURITY CLASSIFICATION OF:			17. LIMITATION OF ABSTRACT:	18. NUMBER OF PAGES	19a. NAME OF RESPONSIBLE PERSON (Monitor)
a. REPORT	b. ABSTRACT	c. THIS PAGE			Christopher R. Marks
Unclassified	Unclassified	Unclassified	SAR	93	19b. TELEPHONE NUMBER (Include Area Code) N/A

TABLE OF CONTENTS

1 SUMMARY 1
2 INTRODUCTION 2
3 METHODOLOGY 5
3.1 Numerical Method 5
3.2 Turbulence Modeling 5
3.3 Non-Dimensionalization 6
3.4 Simulation Setup 6
3.5 Computational Grids 7
3.6 Temporal Boundary Layer Simulation 13
3.7 Boundary Conditions 14
3.8 Identification of Boundary Layer Events 14
3.9 Proper Orthogonal Decomposition (POD) 15
4 FLOW FIELD DESCRIPTION AND COMPARISON OF EXPERIMENT AND SIMULATION 16
4.1 Experiments at PSU 16
4.2 Approach Flow 16
4.3 Mean Flow Comparison 20
4.4 Analysis of Unsteady Flow 28
4.5 Simulation of Laminar Junction Flow 40
5 ACTIVE FLOW CONTROL 43
5.1 Generation of Boundary Layer Events - Active Flow Control 43
5.2 Horseshoe Vortex Behavior Cross-Correlations 48
5.3 Proper Orthogonal Decomposition 59
6 PASSIVE FLOW CONTROL 67
6.1 Effect of Fillet on Mean Flow 67
6.2 Effect of Fillet on Unsteady Flow 72
7 CONCLUSIONS 74
8 ACKNOWLEDGMENTS 76
9 STUDENTS SUPPORTED BY GRANT 77
10 PUBLICATIONS RESULTING FROM GRANT 78
10.1 Conference Publications 78
10.2 Journal Publications 78
NOMENCLATURE 79
12 REFERENCES 82

DISTRIBUTION STATEMENT A. Approved for public release. Distribution is unlimited.

LIST OF FIGURES

Figure 1: a) Grid 1 and b) grid 2. 7
Figure 2: Outlines of 3-D computational domain for a) grid 1 and b) grid 2. Inflow is on the lower left. 9
Figure 3: Computational grid in symmetry plane (z = 0) for a) fillet 1 (r = 0.1) and b) fillet 2 (r = 0.2). 11
Figure 4: Approach flow boundary layer near-wall resolution in wall units. 12
Figure 5: Streamwise (a), crossflow (b), and spanwise (c) near-wall grid resolution in wall units for grid 2. 13
Figure 6: Instantaneous iso-surfaces of Q flooded by streamwise velocity for a) grid 1 (Q=0.1) and b) grid 2 (Q=0.5). 17
Figure 7: Approach boundary layer a) displacement and momentum thickness Reynolds number and shape factor, and b) skin-friction coefficient. 18
Figure 8: a) Approach boundary layer velocity profiles in wall units (x = 5 for grid 1 and x = 4.24 for grid 2). b) Velocity profiles one chord length upstream of Rood wing. 20
Figure 9: Floods (simulation) and contours (PIV measurements [16, 17, 18]) of a) streamwise and b) spanwise velocity as well as c) turbulent kinetic energy and d) $\boldsymbol{u'w'}$ Reynolds stress in symmetry plane 23
Figure 10: Velocity profiles in interaction region. a) x=0.1 and b) z=0.15. 24
Figure 11: Streamlines in symmetry plane. 25
Figure 12: Skin-friction coefficient magnitude iso-contours and skin-friction lines for a) time-average and b) instantaneous flow. 26
Figure 13: Stanton number computed from a) time-averaged and b) instantaneous flow field. 27
Figure 14: Iso-surfaces of a) Q=0.5 flooded by streamwise velocity (instantaneous flow) and b) Q=6 flooded by pitchwise vorticity, ω_y (time-averaged flow). 28
Figure 15: Instantaneous turbulence kinetic energy. 29
Figure 16: Instantaneous iso-surfaces of a) Q=1 (top) and b) 100 (bottom). 30
Figure 17: Instantaneous iso-surfaces of a) Q=1 (top) and b) 100 (bottom). 31
Figure 18: Instantaneous iso-surfaces of a) Q=1 (top) and b) 100 (bottom). 32
Figure 19: Histogram of velocity fluctuations at (x,y,z) = (0.1,0,0.025) and Stanton number fluctuations at (x,y,z) = (0.1,0,0). 33
Figure 20: Vortex core location, maximum Q-criterion, and circulation of horseshoe vortex. 34
Figure 21: Instantaneous iso-surfaces of Q=1, Q=100, and iso-contours of pitchwise vorticity, ω_y, in symmetry plane. 35
Figure 22: Instantaneous iso-surfaces of Q=1. 36
Figure 23: Iso-surfaces of Q=1 (top) and 10 (bottom) flooded by streamwise velocity. Box indicates area over which VITA data for x=1 in Figure 26 were averaged. 37
Figure 24: Iso-contours of 0< VITA < 6 (with T^+=8.6) computed from $c_{f,x}$. 38
Figure 25: Iso-contours of 0 ≤ VITA ≤ 6 (with T^+=1) computed from a) c_p, b) $c_{f,x}$, and c) St. 39
Figure 26: Averages of VITA data (T^+=1, dotted line is for T^+=8.6) for three upstream locations and HV circulation. 40

DISTRIBUTION STATEMENT A. Approved for public release. Distribution is unlimited.

Figure 27: Laminar junction ow: a) Iso-surfaces of Q=0.5 and u-velocity contours in symmetry plane. b) Iso-surfaces of Q=2.....41
Figure 28: Laminar junction flow: Streamwise core position and circulation of HV in symmetry plane.....42
Figure 29: Jet locations. Cases a, b, c, e: Black circle; Case d: Blue circle; Case f: Black and red circles; Case g: Black and green circles. Green "+" symbol indicates saddle point of skin-friction lines. 44
Figure 30: Endwall areas for averaging of VITA value. Saddle point illustrated by green "+" symbol. 45
Figure 31: Case b: Dependence of VITA value on endwall area (Figure 30) and time averaging interval, T_{av}. 46
Figure 32: Cross-correlation of VITA value with normalized forcing signal for a) case a, b) case b, c) case e and d) case f.Horseshoe Vortex Behavior Cross-Correlations 48
Figure 33: Case a: Iso-surfaces of Q=2 (top two rows) and Q=8 (bottom two rows). BL event is highlighted by red box.....50
Figure 34: Case f: Iso-surfaces of Q=2 (top two rows) and Q=8 (bottom two rows). BL event is highlighted by red box.....51
Figure 35: Case g: Iso-surfaces of Q=2 (top two rows) and Q=8 (bottom two rows). BL event is highlighted by red box.....52
Figure 36: Uncontrolled flow: VITA (left), circulation (middle), and cross-correlation of VITA and circulation (right). Signals (top) and spectra (bottom). 54
Figure 37: Case a: VITA (left), circulation (middle), and cross-correlation of VITA and circulation (right). 55
Figure 38: Case b: VITA (left), circulation (middle), and cross-correlation of VITA and circulation (right). 55
Figure 39: Case c: VITA (left), circulation (middle), and cross-correlation of VITA and circulation (right). 56
Figure 40: Case d: VITA (left), circulation (middle), and cross-correlation of VITA and circulation (right). 56
Figure 41: Case e: VITA (left), circulation (middle), and cross-correlation of VITA and circulation (right). 57
Figure 42: Case f: VITA (left), circulation (middle), and cross-correlation of VITA and circulation (right). 57
Figure 43: Case g: VITA (left), circulation (middle), and cross-correlation of VITA and circulation (right). 58
Figure 44: Areas analyzed with POD and jet locations 59
Figure 45: Uncontrolled flow: POD time-coefficients, eigenvalues, and modes 1-6 (iso-surfaces of $\boldsymbol{w = \pm 0.01}$) for red area in Figure 44.....61
Figure 46: Uncontrolled flow: POD time-coefficients, eigenvalues, and modes 1-6 (iso-surfaces of Q=1) for blue area in Figure 44.....62
Figure 47: Case b: POD time-coefficients, eigenvalues, and modes 1-6 (iso-surfaces of $\boldsymbol{w = \pm 0.01}$) for red area in Figure 44. 63
Figure 48: Case b: POD time-coefficients, eigenvalues, and modes 1-6 (iso-surfaces of Q=1) for blue area in Figure 44. 64
Figure 49: Case f: POD time-coefficients, eigenvalues, and modes 1-6 (iso-surfaces of $\boldsymbol{w = \pm 0.01}$) for red area in Figure 44. 65

DISTRIBUTION STATEMENT A. Approved for public release. Distribution is unlimited.

Figure 50: Case f: POD time-coefficients, eigenvalues, and modes 1-6 (iso-surfaces of Q=1) for blue area in Figure 44. 66
Figure 50: Iso-surfaces of Q=100 for cases NF (left), F1 (center) and F2 (right) obtained from a) instantaneous flow fields and b) time-averages. 67
Figure 51: Iso-contours of streamwise velocity in symmetry plane for cases a) NF, b) F1, and c) F2. 69
Figure 52: Streamlines in symmetry plane for cases a) NF, b) F1, and c) F2a) 70
Figure 53: Iso-contours of skin-friction coefficient magnitude and skin-friction lines obtained from time-averages for cases a) NF, b) F1, and c) F2 71
Figure 54: Wall pressure coefficient in symmetry plane. 71
Figure 55: Iso-contours of wall pressure coefficient for cases a) NF, b) F1, and c) F2. 72
Figure 56: Vortex core location and circulation for cases a) NF and b) F1 and F2....73

DISTRIBUTION STATEMENT A. Approved for public release. Distribution is unlimited.

LIST OF TABLES

Table 1: Streamwise positions of inflow and outflow boundaries.....8
Table 2: Number of cells.....9
Table 3: Forcing parameters. 44
Table 4: Endwall areas for averaging of VITA value.....46
Table 5: Mean and standard deviation of streamwise core location, x_c, and circulation, of horseshoe vortex as well as dominant period. 73

DISTRIBUTION STATEMENT A. Approved for public release. Distribution is unlimited.

1 SUMMARY

Turbulent junction flows can be observed in nature and are also common to many engineering applications such as linear low-pressure turbine cascades where horseshoe vortices form around the blunt leading edges of the turbine blades. Earlier research has suggested that the horseshoe vortices demonstrate a bimodal behavior. This behavior can be described as a more or less random switching between a zero-flow and a back-flow state. To obtain further insight into this phenomenon, large-eddy simulations for a canonical junction flow geometry (Rood wing) were carried out for a Reynolds number based on approach flow velocity and maximum thickness of 7,000. The mean flow data were in good agreement with particle image velocimetry measurements at Penn State University. Instantaneous flow visualizations reveal a forward and backward motion of the horseshoe vortex and an intermittent loss of coherence. Upstream boundary layer events which were detected with the variable-interval time-averaging method, were found to be correlated with an intermittent strengthening of the horseshoe vortex. This suggests that the bimodal behavior may be correlated with upstream boundary layer events. To test this hypothesis, pulsed disturbances were deliberately introduced upstream of the junction to generate deterministic boundary layer events. The correlation between the forced boundary layer events and the circulation of the horseshoe vortex was weak which may be attributed to the chosen forcing method. In addition, simulations with two different circular endwall fillets were carried out. In accordance with the literature, the fillets were found to suppress the bimodal behavior. In summary, the present results supports earlier research that suggest that the bimodal behavior is triggered by upstream boundary layer events.

DISTRIBUTION STATEMENT A. Approved for public release. Distribution is unlimited.

2 INTRODUCTION

For today's high bypass jet engines, a large portion of the thrust is generated by the fan which is driven by a massive and heavy low-pressure turbine (LPT). Advanced highly-loaded LPT blade designs, such as the L2F blade by the Air Force Research Laboratory at Wright-Patterson Air Force Base [1], are promising larger LPT efficiencies but were found to suffer from increased endwall losses compared to mid- and aft-loaded airfoils. The losses were attributed to the secondary flow, increased turbulence production, and a strong passage vortex (PV) [2]. When a turbulent boundary layer (BL) interacts with a body, such as for example a turbine blade, a horseshoe vortex (HV) forms around the leading edge of the body. Such turbulent junction flows can exhibit a bimodal behavior which is characterized by the more or less random alternation between a zero-flow state with weak HV and a back-flow state with strong HV that is located closer to the leading edge [3]. Wang et al. [4] performed smoke line visualizations for a linear turbine cascade at a Reynolds number of 10,000 that clearly displayed a bimodal behavior of the HV with a frequency (based on axial chord length and inlet velocity) of $fC_{ax}/v_{in} = 0.6$. Measurements for a L2F cascade by Marks and co-workers [5, 6, 7] and simulations by Gross et al. [8] revealed an intermittent loss of coherence of the PV that appeared related to the bimodal behavior. Since the PV is a large contributor to the losses, this suggests that the junction flow and in particular the bimodal behavior have a strong impact on the overall efficiency of the LPT.

Devenport and Simpson [3] investigated the bimodal behavior for a Rood wing/endwall configuration at a chord Reynolds number of 1.15×10^5. The Rood wing airfoil is named after E.P. Rood and consists of a 3:2 ellipse that is joined with a NACA 0020 airfoil at the maximum thickness. The frequency of the mode switching based on BL thickness, δ, and freestream velocity, U, was $f\delta/U \approx 0.05$. The mode switching was found to be aperiodic which might be expected for a turbulent flow. Devenport and Simpson [3] remarked that the mode switching can lead to increased heat transfer rates (up to 300% for high-pressure turbines), stronger pressure fluctuations, and larger turbulence intensities. This provides additional motivation for research aimed at an improved understanding of the physics of turbulent junction flows. Devenport and Simpson [3] also suggested that the bimodal behavior may be related to turbulent BL bursting events. Finally, the bimodal behavior was determined to be more dependent on the nose bluntness (which sets the adverse pressure gradient) than the Reynolds number as also shown by Mehta [9] and Olcmen and Simpson [10].

Simpson [11] provided a review paper on turbulent junction flows. Although turbulent junction flows are fairly common, the associated physics are still not fully understood. Experiments by Agui and Andreopoulos [12] indicated that large-scale turbulent BL structures may be responsible for an aperiodic displacement of the HV in the streamwise direction that is followed by an eruption of near-wall fluid and the formation of a smaller counter-rotating secondary vortex (SV). Praisner and Smith [13] took measurements near a symmetric airfoil with a cylindrical leading edge and 5:1 trailing edge fairing. They found a reoccurring sudden strengthening of the HV that was linked to a HV displacement towards the leading edge (back-flow state) and a concomitant strengthening of the SV. As the HV gets closer to the leading edge, through induction it causes the SV to move rapidly away from the endwall, thus leading to the zero-flow state. These events have a period of approximately 115-120t^+ in wall units which is close to the period of the bursting events of the undisturbed impinging turbulent BL which

DISTRIBUTION STATEMENT A. Approved for public release. Distribution is unlimited.

suggests that the BL events may be related to the bimodal behavior. Bursts in turbulent BLs refer to the quasi-periodic ejection of near-wall fluid. Particle image velocimetry (PIV) measurements of a flat plate turbulent BL by Adrian et al. [14] suggest that the bursting events are related to hairpin packets. Turbulent junction flow experiments for a tapered cylinder by Sabatino and Smith [15] revealed a correlation between the HV mode switching period and the turbulent BL statics. In the symmetry plane, the dominant period of the HV motion was $260t^+$ and the period of the surface temperature variation was $200t^+$. Sabatino and Smith [15] also proposed that the ingestion of hairpin vorticity by the HV strengthened the HV and led to a HV movement towards the junction and the ejection of the SV. More recently, Lynch and co-workers at Penn State University (PSU) conducted Rood wing junction flow experiments for a Reynolds number range of 7,000 to 80,000 based on approach flow velocity and maximum wing thickness [16, 17, 18]. In the experiments, the region of interest ahead of the junction was fully optically accessible to allow for high-speed stereo PIV measurements. The set-up also included a laser Doppler velocimetry (LDV) system that was used for acquiring BL data, i.e. mean and fluctuating velocity components and Reynolds stresses, upstream of the junction. Conditionally sampled PIV data revealed a bimodal behavior of the HV. The mean HV location was found to depend only weakly on the Reynolds number. However, both the dimensionless turbulent kinetic energy below the HV core and the unsteadiness of the HV was shown to increase with Reynolds number.

Direct numerical simulations (DNS), large-eddy simulations (LES), and hybrid simulations (combination of DNS and LES) constitute another means to investigate the physics of turbulent junction flows. Detached eddy simulations (DES) by Paik et al. [19] for a Rood wing/endwall geometry at Re=115,000 clearly revealed the back-flow state with coherent HV and a state in which three-dimensional (3-D) BL hairpin vorticity is "wrapped around" the HV and "amplified". The amplification was attributed to a centrifugal Görtler-like instability. It is argued that the ingestion and amplification of 3-D vorticity by the HV leads to a loss of coherence of the HV and the establishment of the zero-flow state. Eventually a new weaker coherent HV forms upstream of the junction. The simulations were in reasonable agreement with the experiments by Devenport and Simpson [3]. Allen and Naitoh [20] conducted a fundamental investigation of the HV stability and found that the velocity profile between the endwall and the point of maximum reverse flow velocity satisfies the Rayleigh criterion and that centrifugal instability occurs for Görtler numbers larger than one. Wind tunnel experiments and LES by Gand et al. [21] for a wing junction geometry at $Re = 2.8\times10^5$ displayed a bimodal behavior with a frequency of $0.05<f\delta/U< 0.1$. Escauriaza and Sotiropoulos [22] performed DES of the flow past a circular cylinder. Instantaneous flow visualizations revealed eruptions of near-wall vorticity whose intensity and frequency increased with Reynolds number. These eruptions were related to hairpin vortices that "rolled up" around the HV and led to a loss of coherence of the HV. Schwänen et al. [23] performed a DNS of the turbulent flow through a first stage high-pressure stator cascade at Re=10,000. The simulation revealed a pronounced aperiodic motion of the HV. Cui et al. [24] carried out LES of a T106a cascade which indicated an instability of the HV system ahead of the leading edge that was characterized by "multiple separations."

Smith and Walker [27] conducted a detailed analysis of passive and active control strategies for turbulent junction flows. The addition of an endwall fillet weakens the HV by reducing the adverse pressure gradient ahead of the junction (e.g., Devenport et al. [28]). The HV can also be

DISTRIBUTION STATEMENT A. Approved for public release. Distribution is unlimited.

effectively eliminated with suction (e.g., Johnson et al. [29], Seal and Smith [30]). Other forms of passive flow control were employed to reduce the junction flow unsteadiness. For example, Olcmen and Simpson [31] used fences and Apsilidis et al. [32] investigated the effect of wall roughness.

DISTRIBUTION STATEMENT A. Approved for public release. Distribution is unlimited.

3 METHODOLOGY

3.1 Numerical Method

The present simulations were carried out with a research computational fluid dynamics code by Gross and Fasel [33]. The code solves the compressible Navier-Stokes equations in curvilinear coordinates. For robustness, especially on highly distorted grids, a finite volume formulation is employed. The convective terms of the Navier-Stokes equations are discretized with a ninth-order-accurate scheme. Details regarding the higher-order-accurate weighted essentially non-oscillatory discretization of the convective terms are provided in Ref. [34]. The viscous terms are discretized with fourth-order-accuracy. The implicit second-order-accurate trapezoid rule is employed for time integration.

3.2 Turbulence Modeling

The subgrid stress (SGS) tensor,

$$\boldsymbol{\tau_{ij}} = \overline{\boldsymbol{\rho}}\left(\widetilde{\boldsymbol{u_i u_j}} - \widetilde{\boldsymbol{u_i}}\widetilde{\boldsymbol{u_j}}\right) \quad \textbf{(1)}$$

is modeled as

$$\boldsymbol{\tau_{ij}} = -2\boldsymbol{\mu_T}\left(\boldsymbol{S_{ij}} - \frac{\mathbf{1}}{\mathbf{3}}\boldsymbol{S_{kk}}\boldsymbol{\delta_{ij}}\right) + \frac{\mathbf{1}}{\mathbf{3}}\boldsymbol{\tau_{kk}}\boldsymbol{\delta_{ij}} \quad \textbf{(2)}$$

Where

$$\boldsymbol{S_{ij}} = \frac{\mathbf{1}}{\mathbf{2}}\left(\frac{\boldsymbol{\partial u_i}}{\boldsymbol{\partial x_j}} + \frac{\boldsymbol{\partial u_j}}{\boldsymbol{\partial x_i}}\right) \quad \textbf{(3)}$$

is the strain rate tensor of the resolved scales. The deviatoric part is proportional to a SGS (unresolved) eddy-viscosity, μ_T. According to Erlebacher et al. [35], the isotropic part, τ_{kk}, is very small compared to the thermodynamic pressure and hence neglected. The heat flux is computed as

$$\boldsymbol{q_i} = -\boldsymbol{c_p}\left(\frac{\boldsymbol{\mu}}{\boldsymbol{Pr}} + \frac{\boldsymbol{\mu_T}}{\boldsymbol{Pr_T}}\right)\frac{\boldsymbol{\partial T}}{\boldsymbol{\partial x_i}} \quad \textbf{(4)}$$

For the wall-adapting local eddy-viscosity (WALE) model by Nicoud and Ducros [36], the subgrid (unresolved) viscosity is modeled as

$$\boldsymbol{\mu_T} = \overline{\boldsymbol{\rho}}\boldsymbol{\Delta^2 C_w^2}\frac{\left(\boldsymbol{S_{ij}^* S_{ij}^*}\right)^{\frac{\mathbf{3}}{\mathbf{2}}}}{\left(\boldsymbol{S_{ij}S_{ij}}\right)^{\frac{\mathbf{5}}{\mathbf{2}}} + \left(\boldsymbol{S_{ij}^* S_{ij}^*}\right)^{\frac{\mathbf{5}}{\mathbf{4}}}}$$

DISTRIBUTION STATEMENT A. Approved for public release. Distribution is unlimited.

(5)

with

$$S_*^{ij} = \frac{1}{2}\left(g_{ij}^2 + g_{ji}^2\right) - \frac{1}{3} g_{kk}^2 \delta_{ij},$$

(6)

$$g_{ij}^2 = g_{ik} g_{kj},$$

(7)

$$g_{ij} = \frac{\partial u_i}{\partial x_j},$$

(8)

and model constant C_w=0.5. For the present results, the grid length-scale, Δ, was chosen as the geometric average of the cell dimensions. The WALE model accounts for the effects of both the strain and rotation rate of the smallest resolved turbulent fluctuations. It recovers the proper y^3 near-wall scaling for the eddy viscosity.

3.3 Non-Dimensionalization

The chord length and maximum thickness of the Rood wing airfoil of the Penn State University (PSU) experiments were c=40cm and t=9.42cm [16, 17, 18]. For the present simulations, the maximum thickness, t, was chosen as reference length scale. With this scaling, the chord length becomes $c = 4.239$. The inlet freestream velocity, v_{in}, was taken as reference velocity. Time was made dimensionless with t/v_{in}.

3.4 Simulation Setup

The simulations were set up according to the PSU experiments [16, 17, 18]. The Rood wing span in the experiment was H=54.5cm. Only half of the wing span, $H/(2t) = 2.914$, was simulated and symmetry conditions were enforced at mid-span. The freestream temperature was 286K and the wall temperature was 311K. The freestream turbulence intensity in the wind tunnel was roughly 1%. For the present simulations, because of the high computational cost associated with resolving turbulent velocity fluctuations in the freestream, the freestream turbulence was set to zero. Unless noted otherwise, the Reynolds number based on maximum thickness was $Re = 7{,}000$ (lowest Reynolds number of the PSU experiments). The reference Mach number was set to $M = 0.1$. This Mach number is small enough to satisfy the incompressible flow assumption without negatively affecting the convergence characteristics of the implicit time-integration scheme. The laminar and turbulent Prandtl numbers were $Pr = 0.72$ and $Pr_T = 0.9$ and the computational timestep was $\Delta t = 0.005$.

DISTRIBUTION STATEMENT A. Approved for public release. Distribution is unlimited.

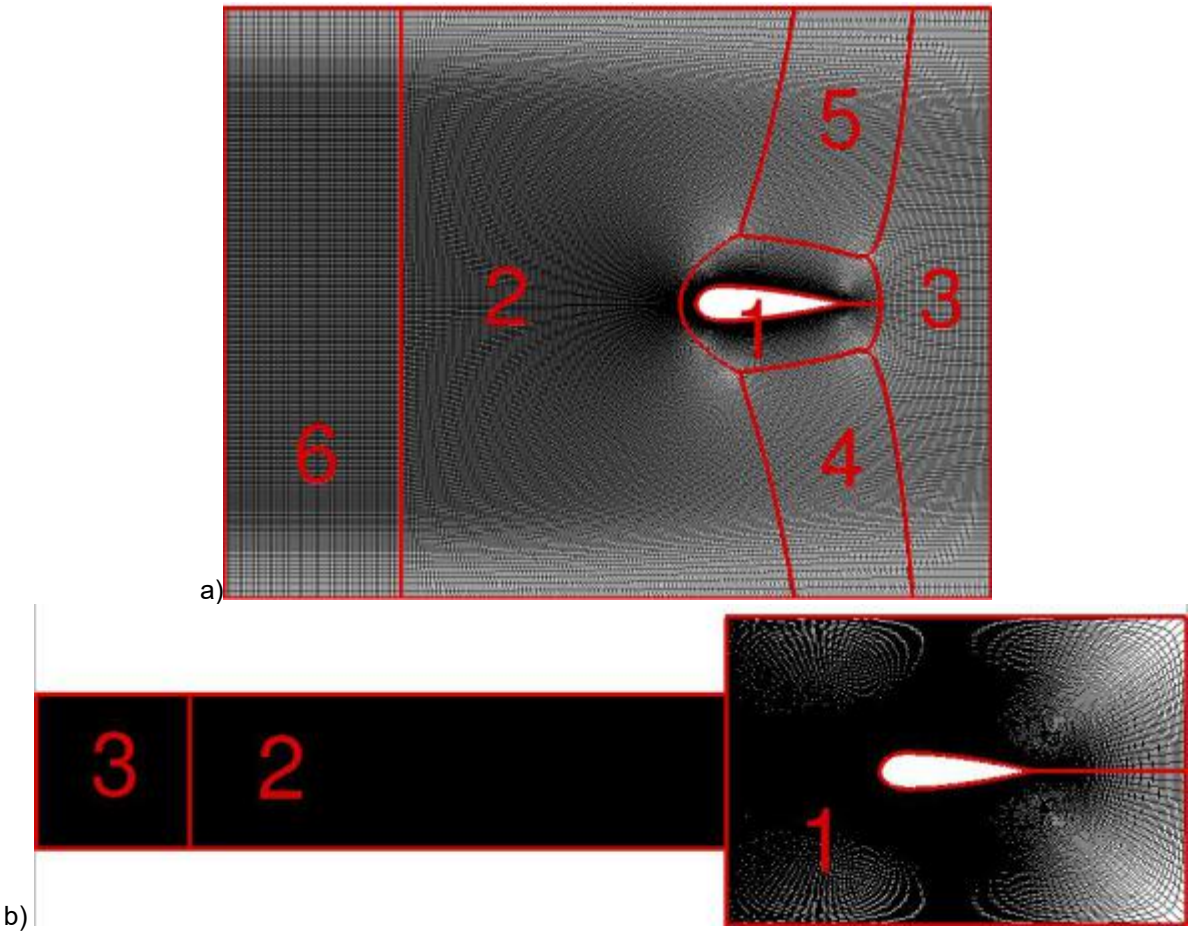


Figure 1: a) Grid 1 and b) grid 2.

3.5 Computational Grids

Various different two-dimensional (2-D) grids were generated with a Poisson grid generator [37]. The two grids shown in Figure 1 provided the basis for the simulations that are discussed in this report. Grid line stretching was employed near the outflow to dissipate wake structures. The width of the PSU wind tunnel test section (pitchwise extent) is 1.12m. Made dimensionless with the profile thickness, this corresponds to a width of 11.89. The pitchwise domain boundaries are at 8.478 for grid 1 and at 4.239 (block 1) and 2.120 (blocks 2 and 3) for grid 2. The locations of the inflow and outflow boundaries are provided in Tab. 1.

DISTRIBUTION STATEMENT A. Approved for public release. Distribution is unlimited.

Table 1: Streamwise positions of inflow and outflow boundaries.

Block	*Grid 1*		*Grid 2*	
	Inflow	*Outflow*	*Inflow*	*Outflow*
1	-0.4616 - 1.273	4.863 – 5.297	-4.239	8.478
2	-8.478	-0.4616 – 2.826	-19.067	-4.239
3	4.863 – 6.217	8.478	-23.304	-19.067
4,5	1.273 – 2.826	4.863 – 6.217		
6	-13.550	-8.478		

The 2-D grids were "extruded" in the spanwise direction over a spanwise distance of 2.914 (Figure 2). Towards this end, a grid line distribution that provides grid line clustering near the lower wall and blends towards an equidistant spacing near mid-span,

$$\boldsymbol{z_0 = 0} \quad \textbf{(9)}$$

$$\boldsymbol{z_1 = \Delta z} \quad \textbf{(10)}$$

$$\boldsymbol{z_k = z_{k-1} + \left[0.1\left(\frac{k-K}{2-K}\right)^c + 1\right](z_{k-1} - z_{k-2})\ for\ k \geq 2} \quad \textbf{(11)}$$

was employed. The wall-normal grid line spacing at the lower wall is $\Delta z = 2 \times 10^{-3}$ for grid 1 and 4×10^{-4} for grid 2. The number of cells per block and the total number of cells for the two blocks are provided in Table 2.

DISTRIBUTION STATEMENT A. Approved for public release. Distribution is unlimited.

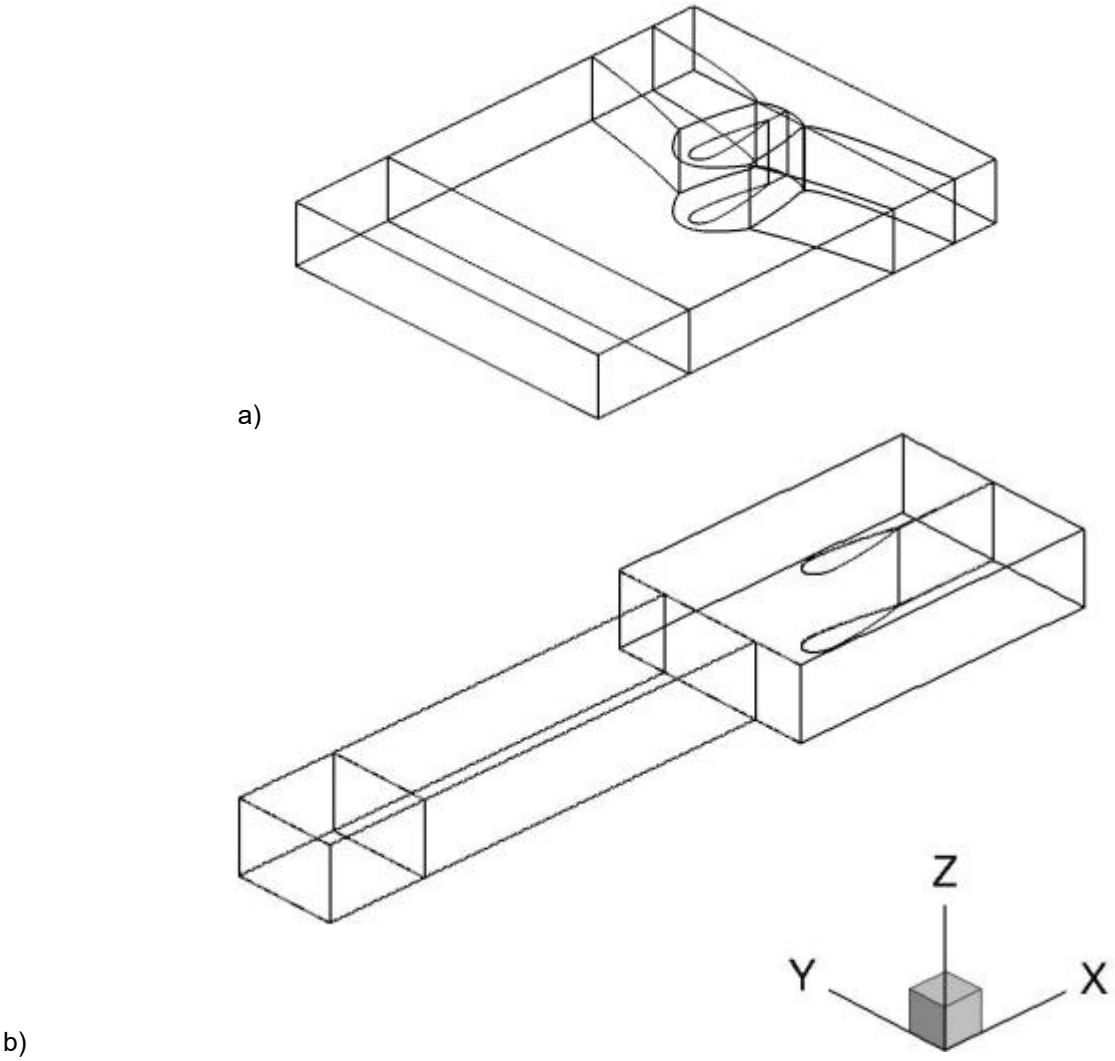


Figure 2: Outlines of 3-D computational domain for a) grid 1 and b) grid 2. Inflow is on the lower left.

Table 2: Number of cells.

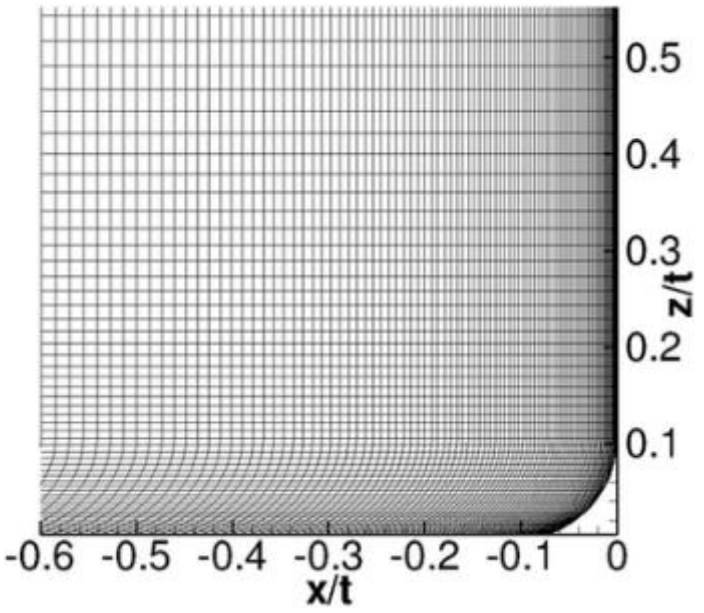
Block	*Grid1*	*Grid2*
1	380x 70x112	410x200x96
2	200x400x112	245x150x96
3	40x260x112	70x150x96
4	60x100x112	
5	60x100x112	
6	100x400x112	
Total	18,928,000	12,408,000

DISTRIBUTION STATEMENT A. Approved for public release. Distribution is unlimited.

In addition to this baseline 3-D grid with straight endwall junction, two grids with circular endwall fillets were generated by modifying the block 1 grid near the endwall (Figure 3). The block grid resolutions were identical to those listed in Tab. 2. The fillet radius was $r = t = 0.1$ for fillet 1 ("F1") and 0.2 for fillet 2 ("F2"). The near-wall grid resolution in wall units for the approach BL is provided in Figure 4. Georgiadis et al. [38] recommend grid resolutions of $10 \leq \Delta x^+ \leq 20$, $\Delta y^+ \leq 1$ (wall-normal, equivalent to Δz^+ for present simulations), $5 \leq \Delta z^+ \leq 10$ for direct numerical simulations (DNS) and $50 \leq \Delta x^+ \leq 150$, $\Delta y^+ \leq 1$, $15 \leq \Delta z^+ \leq 40$ for LES. For comparison, Nicoud and Ducros [36] employed near-wall grid resolutions of $\Delta x^+ = 28$, $\Delta y^+ = 2.1$, and $\Delta z^+ = 8.8$ for their WALE model LES. The respective values for grid 2 upstream of the junction, $\Delta x^+ = 20$, $\Delta y^+ = 8.8$, and $\Delta z^+ = 0.32$, are close to the Nicoud and Ducros values. Contours of the near-wall grid line spacing for grid 2 are provided in Figure 5. Because of the chosen block 1 O-grid topology, the grid resolution improves as the BL approaches the Rood wing leading edge and then rapidly decreases downstream. Since the interest is on the interaction region and not on the downstream region, this grid property is desirable.

DISTRIBUTION STATEMENT A. Approved for public release. Distribution is unlimited.

a)



b)

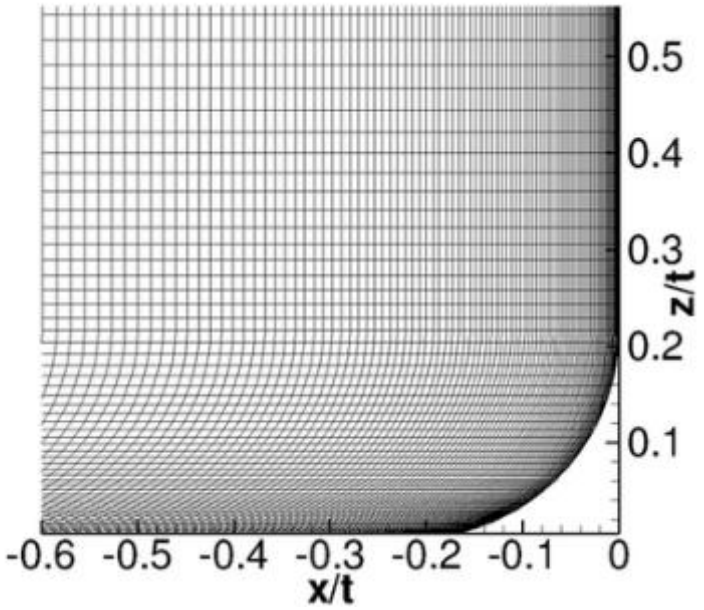


Figure 3: Computational grid in symmetry plane (z = 0) for a) fillet 1 (r = 0.1) and b) fillet 2 (r = 0.2).

DISTRIBUTION STATEMENT A. Approved for public release. Distribution is unlimited.

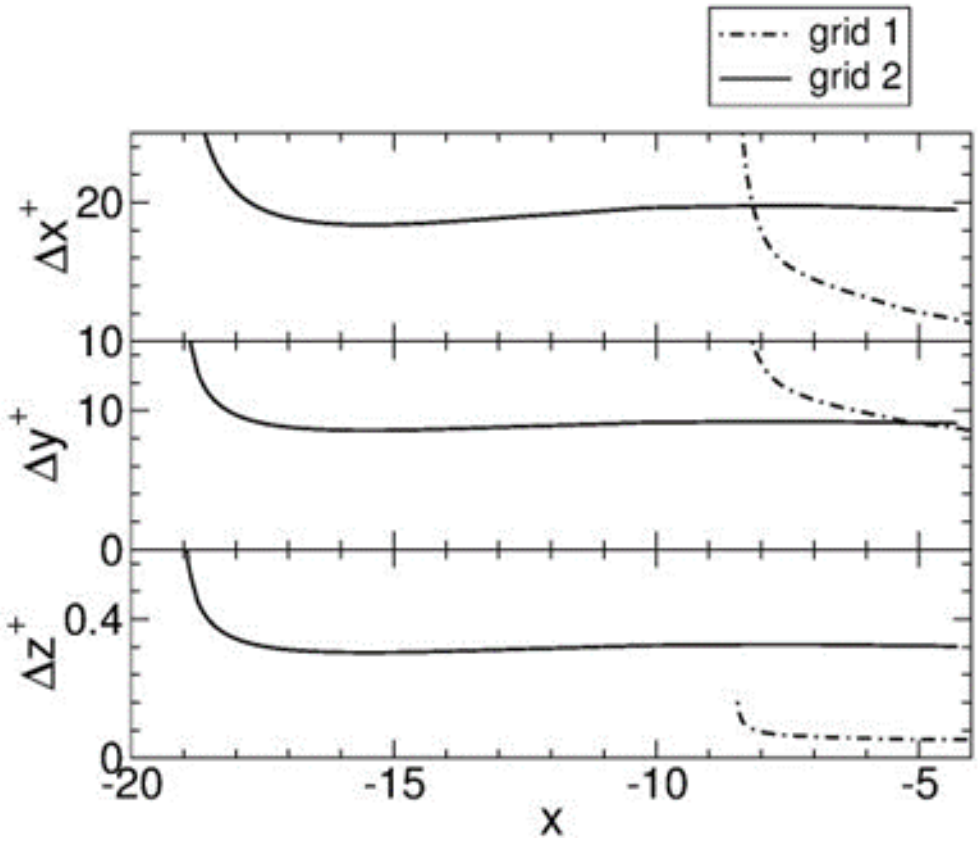


Figure 4: Approach flow boundary layer near-wall resolution in wall units.

DISTRIBUTION STATEMENT A. Approved for public release. Distribution is unlimited.

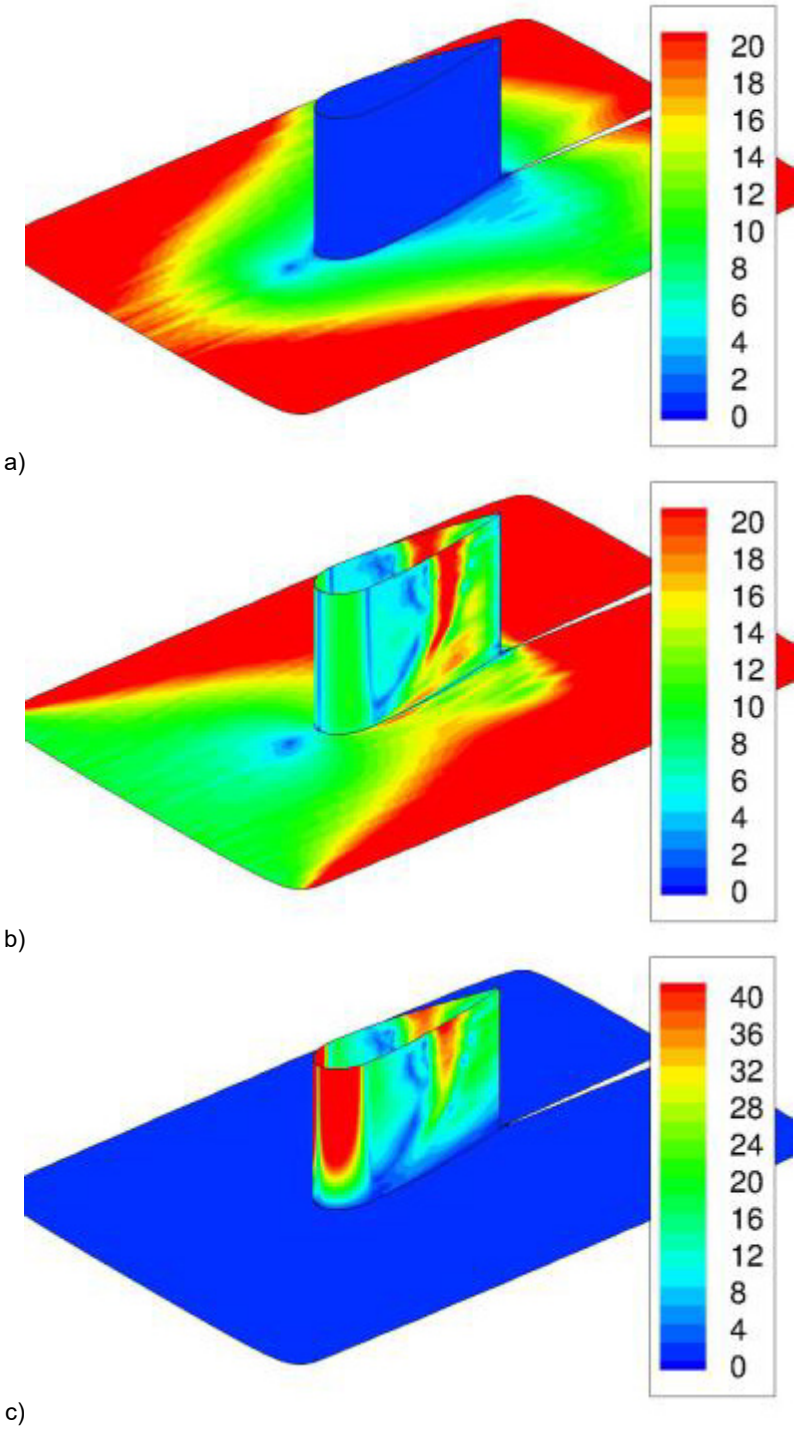


Figure 5: Streamwise (a), crossflow (b), and spanwise (c) near-wall grid resolution in wall units for grid 2.

3.6 Temporal Boundary Layer Simulation

Block 3 was employed for temporal boundary layer simulations that provide turbulent inflow data for block 2. The shifted periodic boundary condition approach by Munters et al. [39] was employed to prevent the spanwise locking of large-scale structures. To maintain a constant BL

DISTRIBUTION STATEMENT A. Approved for public release. Distribution is unlimited.

thickness, after each timestep the primitive variables were averaged in the streamwise and pitchwise direction. The average was subtracted from the instantaneous data to obtain the fluctuations. The fluctuations were then added to a turbulent velocity profile from a precursor Reynolds-averaged Navier-Stokes (RANS) calculation. In the freestream, the conservative variables were forced to the RANS profile.

3.7 Boundary Conditions

All walls were considered as isothermal. Slip wall conditions were employed at the spanwise domain boundary (half-span of Rood wing). The time-dependent outflow data from the temporal simulation (block 3) were "fed" into block 2 at the inflow boundary. For blocks 2 and 3, periodicity conditions were enforced in the pitch-wise direction. A non-reflecting boundary condition [40] was applied at the pitchwise domain boundaries of block 1. The non-reflecting boundary condition was also applied at the outflow boundary (block 1).

3.8 Identification of Boundary Layer Events

The variable-interval time-averaging (VITA) method by Blackwelder and Kaplan [26] was employed to detect coherent BL events. For any variable f, the VITA value is computed from

$$\boldsymbol{VITA(t) = \frac{var(t)}{\overline{f^2_{RMS}}}}$$

(12)

$$\boldsymbol{var(t) = \overline{f^2} - \bar{f}^2}$$

(13)

$$\boldsymbol{\bar{f} = \frac{1}{T_{av}} \int_{t-\frac{T_{av}}{2}}^{t+\frac{T_{av}}{2}} f \, d\tau}$$

(14)

$$\boldsymbol{\overline{f^2} = \frac{1}{T_{av}} \int_{t-\frac{T_{av}}{2}}^{t+\frac{T_{av}}{2}} f^2 d\tau.}$$

(15)

$$\boldsymbol{\overline{f^2}_{RMS} = \lim_{T\to\infty} \frac{1}{T} \int_0^T f^2 d\tau.}$$

(16)

For the original method, both $\bar{f}$ and $\overline{f^2}$ are averaged over a time interval (in wall units) of $T_{av}^+ = 8.6$. An event is detected when $VITA(t) \geq 1$.

DISTRIBUTION STATEMENT A. Approved for public release. Distribution is unlimited.

3.9 Proper Orthogonal Decomposition (POD)

The proper orthogonal decomposition (POD) [41] decomposes a time-dependent velocity field,

$$\boldsymbol{v}(\boldsymbol{x},\boldsymbol{t}) = \sum \boldsymbol{a_i}(\boldsymbol{t})\, \boldsymbol{q_i}(\boldsymbol{t}) \quad \textbf{(17)}$$

into a sum of products of time-coefficients, $a_i(t)$, and modes, $q_i(x)$. The magnitude of the associated eigenvalues, λ_i, is identical to two times the kinetic energy of the respective modes. The POD modes form an orthogonal basis and are here sorted according to their energy content. The present POD results were obtained with the "snapshot" method by Sirovich [42].

DISTRIBUTION STATEMENT A. Approved for public release. Distribution is unlimited.

4 FLOW FIELD DESCRIPTION AND COMPARISON OF EXPERIMENT AND SIMULATION

Two-dimensional (2-D) simulations were carried out as a precursor for the three-dimensional (3-D) simulations. Instantaneous flow fields from the 2-D simulations were extended in the spanwise direction to obtain initial conditions for the 3-D simulations. In addition, before commencing the 3-D simulations, the temporal BL simulations were initialized and advanced in time until the near-wall turbulence was fully developed.

4.1 Experiments at PSU

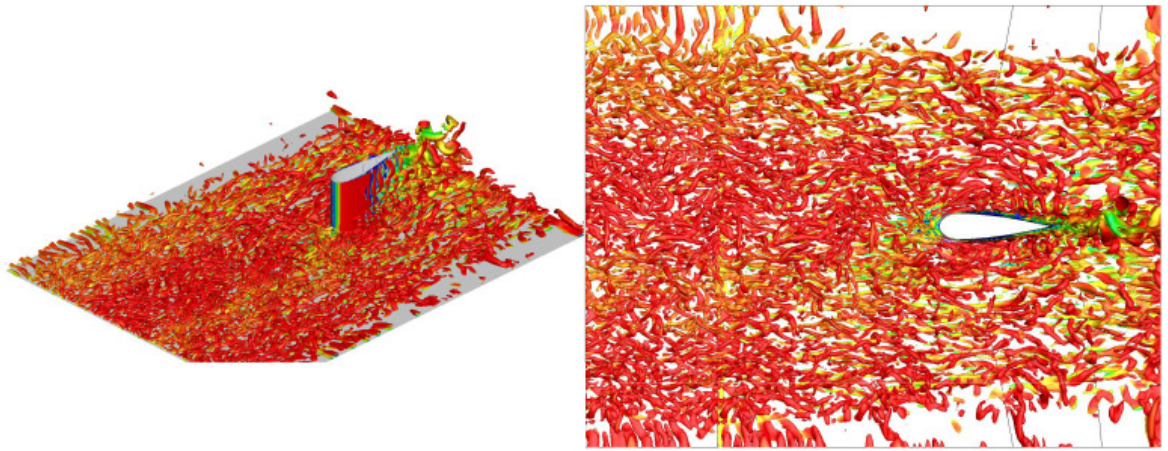
Rood wing junction flow experiments for a wide Reynolds number range, 7,000 to 80,000, based on approach flow velocity and maximum wing thickness were carried out by Lynch and co-workers at Penn State University (PSU) [16, 17, 18]. The flow was fully optically accessible and measurements of the interaction region were taken with a high-speed stereo particle image velocimetry (PIV) system that samples at kHz rates. In addition, BL data (mean and fluctuating velocities, Reynolds stresses) were taken upstream of the junction with a laser Doppler velocimetry (LDV) system. Conditional sampling of the PIV data in the symmetry plane upstream of the Rood wing clearly revealed the bimodal behavior. The lowest Reynolds number of the experiments ($Re = 7{,}000$ based on thickness and $Re = 29{,}670$ based on chord) was chosen for the present LES.

4.2 Approach Flow

Instantaneous iso-surfaces of the Q-criterion by Hunt [43] flooded by the streamwise velocity ($0 < u < 1$) are shown in Figure 6. The visualizations reveal that the data from the temporal BL simulations is fed seamlessly into block 2 (inflow boundary of spatial simulations). For both grids, “streaky” near-wall structure and occasional hairpin vortices are observed for the turbulent approach BL. The Rood wing is embedded in the turbulent BL. Away from the endwall, attached laminar BLs originate from the Rood wing leading edge and then separate at the maximum thickness location. A Kelvin-Helmholtz instability of the separated BLs leads to the shedding of spanwise coherent structures and turbulent breakdown. For grid 1, the grid resolution near the pitchwise domain boundaries is low and few unsteady flow structures are resolved. Similarly, for grid 2, block 1, few structures are observed near the pitchwise and outflow boundaries where the grid resolution is poor.

DISTRIBUTION STATEMENT A. Approved for public release. Distribution is unlimited.

a)



b)

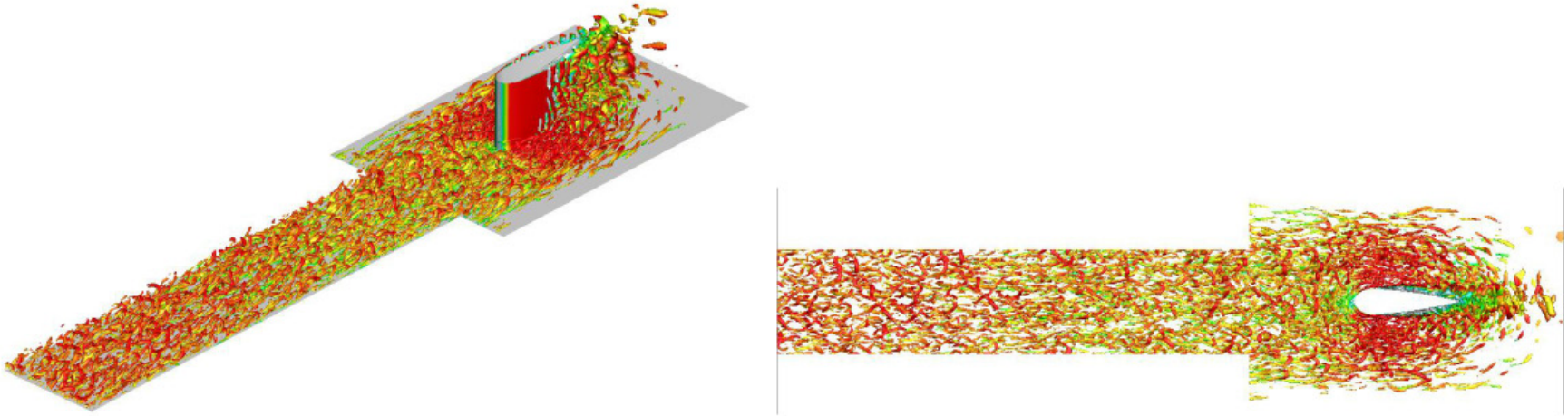
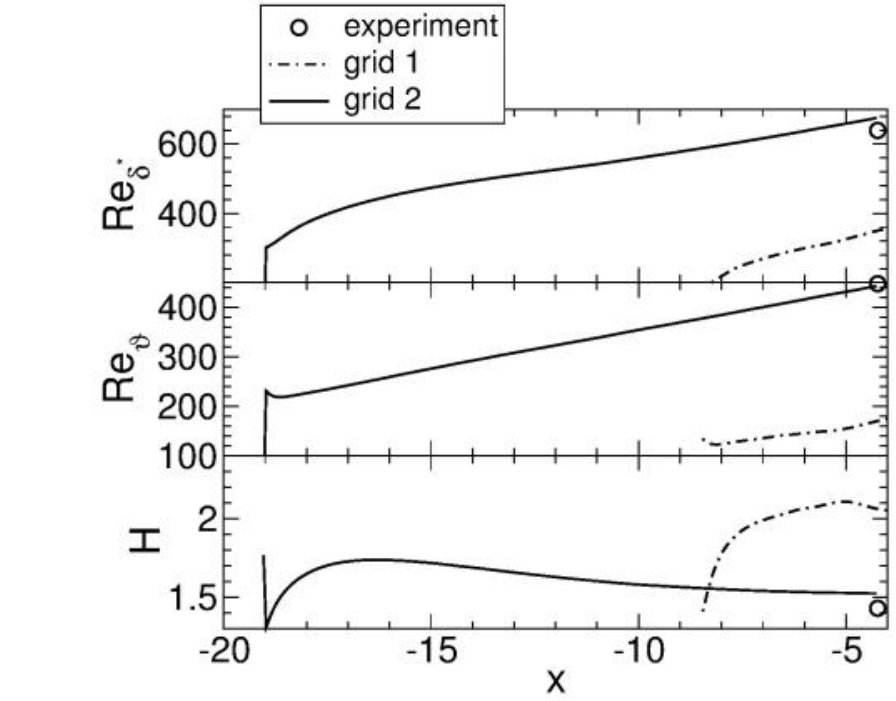
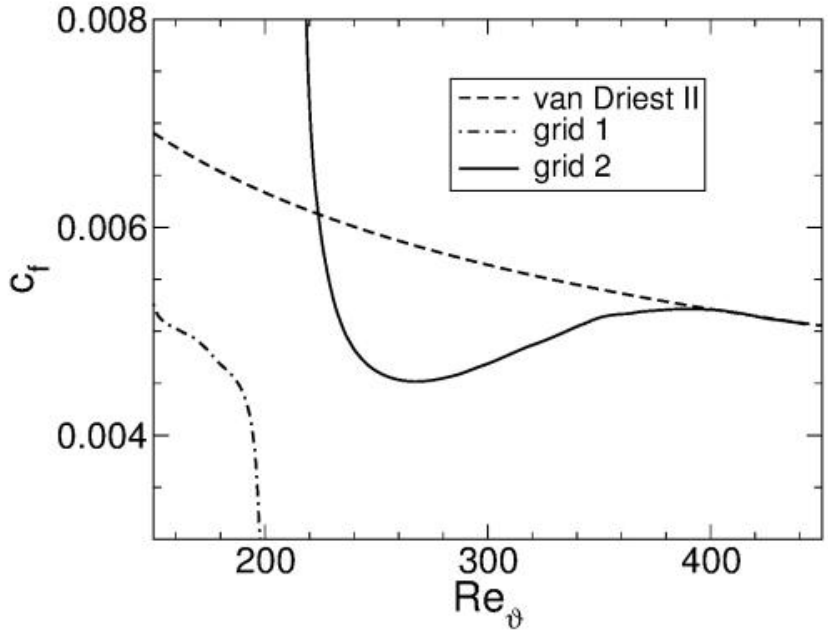


Figure 6: Instantaneous iso-surfaces of Q flooded by streamwise velocity for a) grid 1 (Q=0.1) and b) grid 2 (Q=0.5).

DISTRIBUTION STATEMENT A. Approved for public release. Distribution is unlimited.



a)



b)

Figure 7: Approach boundary layer a) displacement and momentum thickness Reynolds number and shape factor, and b) skin-friction coefficient.

Laser Doppler velocimetry (LDV) measurements at PSU one chord length upstream of the Rood wing provided displacement and momentum thickness-based Reynolds numbers of $Re_{\delta^*} = 639$ and $Re_\vartheta = 448$. The corresponding shape factor is $H = Re_{\delta^*}/Re_\vartheta = 1.43$. These values must be matched in the simulations to allow for a direct comparison with the PSU particle image velocimetry (PIV) measurements. The displacement and momentum thickness Reynolds number

DISTRIBUTION STATEMENT A. Approved for public release. Distribution is unlimited.

as well as the shape factor obtained from block 2 of the simulations are provided in Figure 7a. The symbols represent the experimental data. Time-averages were computed over a time interval of 30 (grid 1) and 100 (grid 2). For both simulations, the displacement and momentum thickness are growing in the streamwise direction and the shape factor is asymptotically approaching a value of H = 2.1 for grid 1 and 1.5 for grid 2. The former is far outside the typical range for turbulent BLs, $1.3 < H < 1.4$. For the integration of the displacement and momentum thickness, the BL edge was taken as the wall-normal location where the pitchwise vorticity dropped below 0.01% of the wall-vorticity. For the grid 2 simulation, the displacement and momentum thickness one chord-length upstream of the Rood wing approximately match the measured data (symbols) and the skin-friction coefficient upstream of the junction is in good agreement with van Driest II [44] (Figure 7b).

In Figure 8a velocity profiles in wall units are compared with the relationships for the laminar sublayer, $u^+ = z^+$, and the log-layer, $u^+ = 5 + ln\, z^+/0.41$. For grid 1 the log-layer is not developed which suggests that the BL is not fully turbulent. For grid 2, a distinct log-layer is visible. Although the grid 1 simulation (and other simulations that are not shown here) provided useful information for setting up the finally successful grid 2 simulation, it agrees poorly with the experiment. This can be attributed to an insufficient downstream extent of block 2. As a result, the spatial turbulent BL does not reach an equilibrium state upstream of the junction. It was thus decided to discontinue the grid 1 simulation. The following analyses and discussions are exclusively for the grid 2 simulation. A direct comparison with the PSU LDV data for grid 2 reveals excellent agreement of the velocity profile upstream of the junction (Figure 8b).

DISTRIBUTION STATEMENT A. Approved for public release. Distribution is unlimited.

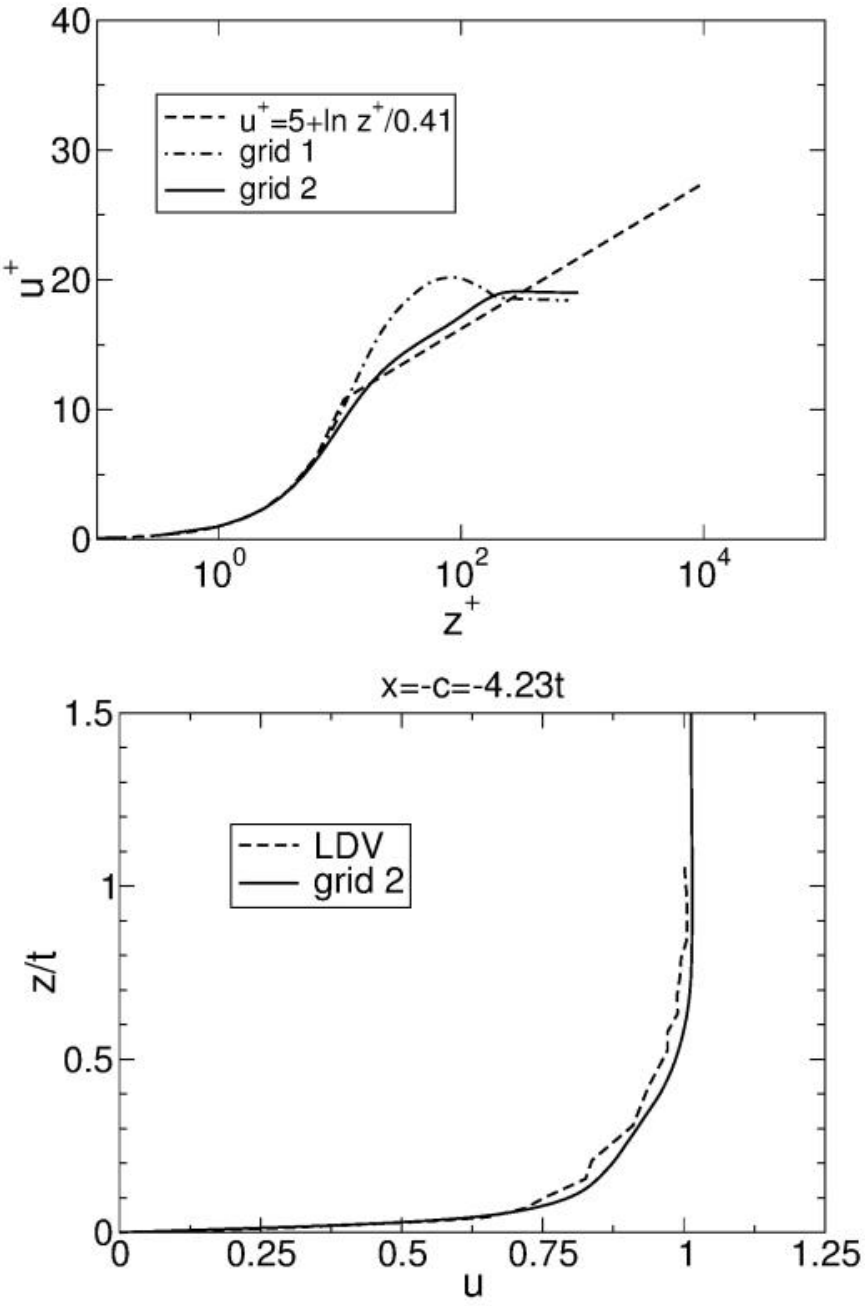


Figure 8: a) Approach boundary layer velocity profiles in wall units (x = 5 for grid 1 and x = 4.24 for grid 2). b) Velocity profiles one chord length upstream of Rood wing.

4.3 Mean Flow Comparison

The straight Rood wing flow field (no fillet) was averaged over a time interval of 125. Iso-contours of the streamwise, u, and spanwise, w, velocity components in the symmetry plane upstream of the junction obtained from both simulation (floods) and PSU PIV measurements (lines) [16, 17, 18] are compared in Figures 9a and b. The agreement of the two data sets is good

DISTRIBUTION STATEMENT A. Approved for public release. Distribution is unlimited.

and overall better than in Gross and Robison [25] because of the longer time averaging interval. Statistical quantities were computed over a time interval of 75. The turbulent kinetic energy and $\overline{u'w'}$-component of the Reynolds stress tensor in the symmetry plane are compared in Figures 9c & d. Both quantities are in adequate agreement with the PSU PIV measurements [16, 17, 18]. Velocity profiles in the center of the reverse flow region, 0.1 profile thicknesses upstream of the leading edge are shown in Figure 10a. The profile shape and maximum reverse flow velocity obtained from the simulation are in good agreement with the PSU measurements. Figure 10b provides spanwise velocity profiles for the center of the downwash region at the leading edge. Compared to the experiment, in the simulation the intensity of the downwash is slightly under-predicted.

Iso-contours of the streamfunction computed from the time-averaged flow field (Figure 11) reveal that the reverse flow region is elongated in the streamwise direction which hints at a back and forth motion of the horseshoe vortex (HV). The core of the time-averaged HV is situated at $(x, z) = (0.12, 0.042)$. A smaller secondary vortex with opposite sense of rotation is located at $(x, z) = (0.014, 0.019)$. Figure 12 provides a top-down view of the forward part of the interaction region. The wall is flooded by the magnitude of the skin-friction coefficient. Skin-friction lines for the time-averaged flow reveal a stagnation point at $x = 0.60$ and a node at $x = 0.028$. The node is situated where the dividing streamline between the HV and the smaller reverse flow vortex hits the wall (Figure 11). The mean-flow skin-friction is close to zero in the vicinity of both singular points and quite large in the shoulder regions (Figure 12a). The visualization of the instantaneous skin-friction (Figure 12b) indicates unsteady flow structures in the approach flow BL and the junction region itself.

By maintaining a constant wall temperature, the effect of the unsteady flow on the wall heat transfer can be investigated. This technique was borrowed from the PSU experiment where distributed heating and an infrared camera are employed for the same purpose. The heat transfer coefficient is

$$\boldsymbol{h} = \frac{\boldsymbol{q}}{\boldsymbol{\Delta T}}, \tag{18}$$

where $\Delta T = {}_{w} - {}_{1}$ is the difference between the wall and freestream temperature and

$$\mathbf{q} = -\mathbf{k}\frac{\partial \mathbf{T}}{\partial \mathbf{z}}, \tag{19}$$

is the heat flux with thermal conductivity,

$$\boldsymbol{k} = \frac{\boldsymbol{c_p}}{\boldsymbol{Pr}}\boldsymbol{\mu}, \tag{20}$$

and wall distance z. The Stanton number which is defined as

$$\boldsymbol{St} = \frac{\boldsymbol{h}}{\boldsymbol{\rho_\infty v_\infty c_p}}, \tag{21}$$

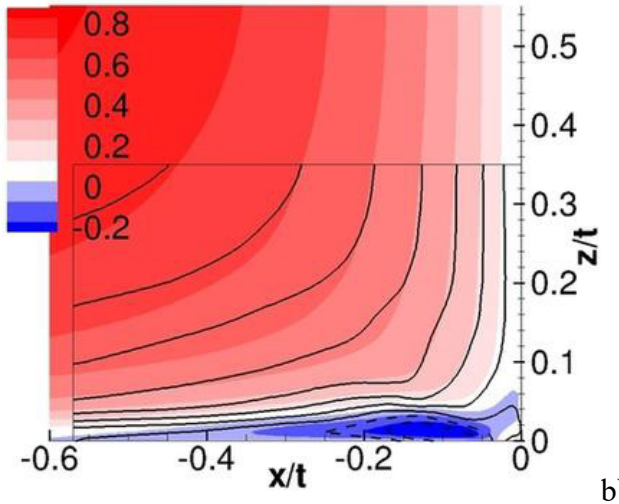
DISTRIBUTION STATEMENT A. Approved for public release. Distribution is unlimited.

can be computed from the dimensionless variables via,

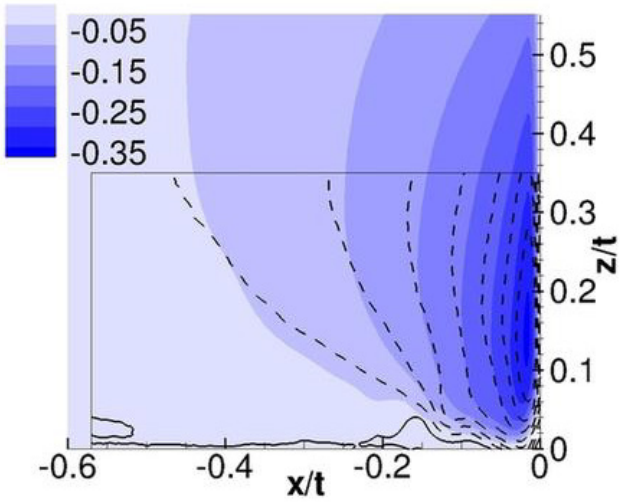
$$St = \frac{-\mu \frac{\partial T}{\partial z}}{RePr(1-T_w)}.$$

(22)

Iso-contours of the Stanton number are provided in Figure 13. The heat flux computed from the time-mean attains its maximum in the stagnation point region (13a). The distribution is close to symmetric and follows the leading edge curvature which suggests that it is directly related to the HV. This is in contrast to the instantaneous visualization (Figure 13b), which reveals unsteady flow structures in the approach flow and several organized structures that wrap around the leading edge of the Rood wing.

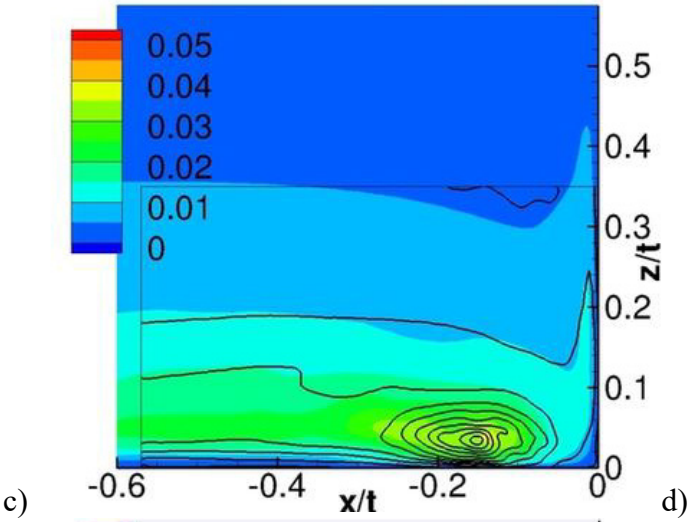


a) b)b)

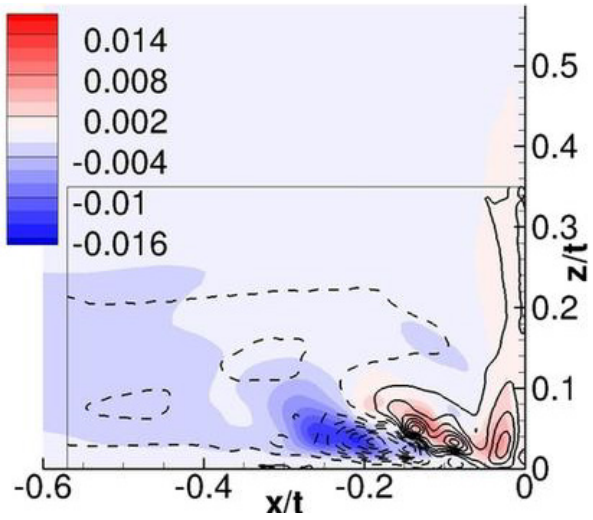


b)

DISTRIBUTION STATEMENT A. Approved for public release. Distribution is unlimited.



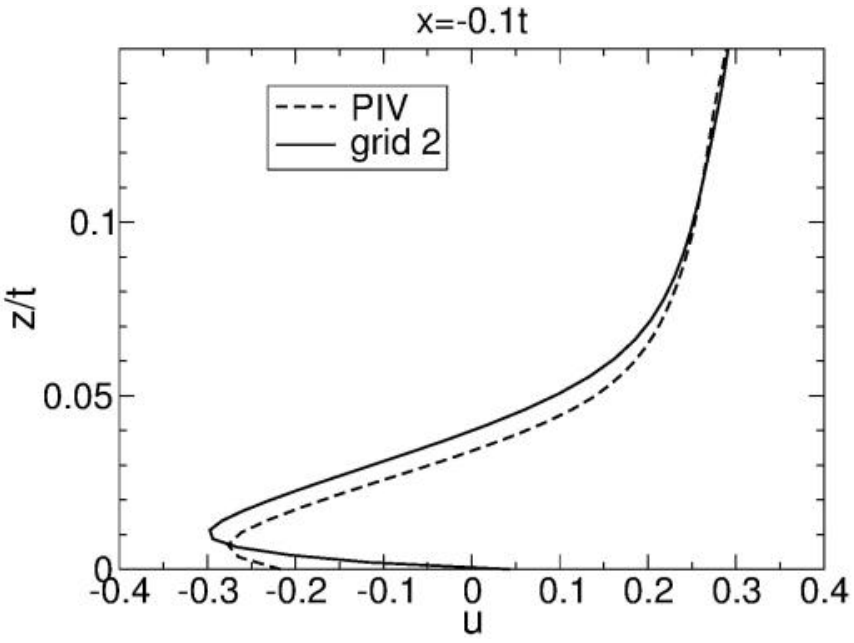
c) d)



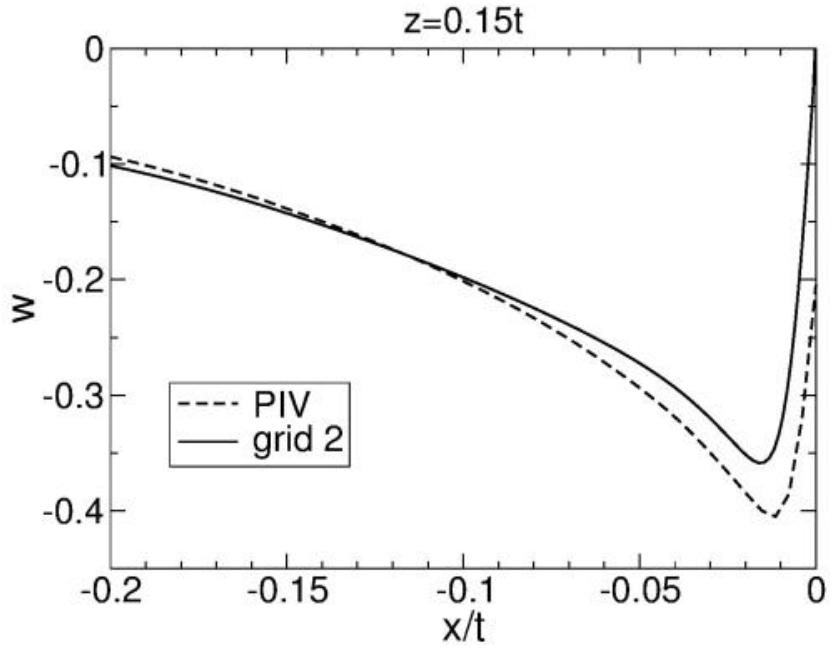
d)

Figure 9: Floods (simulation) and contours (PIV measurements [16, 17, 18]) of a) streamwise and b) spanwise velocity as well as c) turbulent kinetic energy and d) $\overline{u'w'}$ Reynolds stress in symmetry plane

DISTRIBUTION STATEMENT A. Approved for public release. Distribution is unlimited.



a)



b)

Figure 10: Velocity profiles in interaction region. a) x=0.1 and b) z=0.15.

DISTRIBUTION STATEMENT A. Approved for public release. Distribution is unlimited.

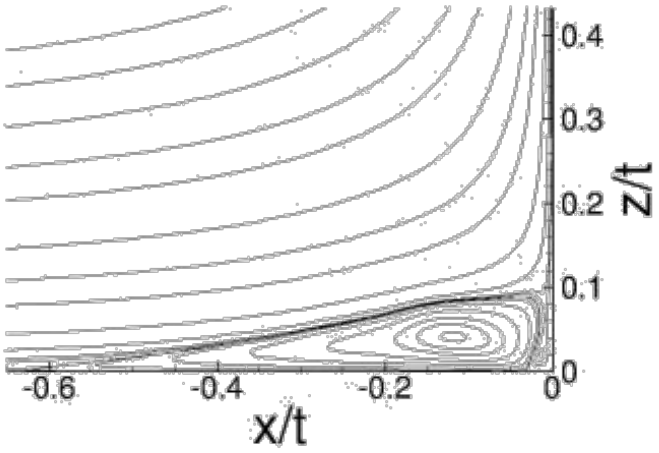
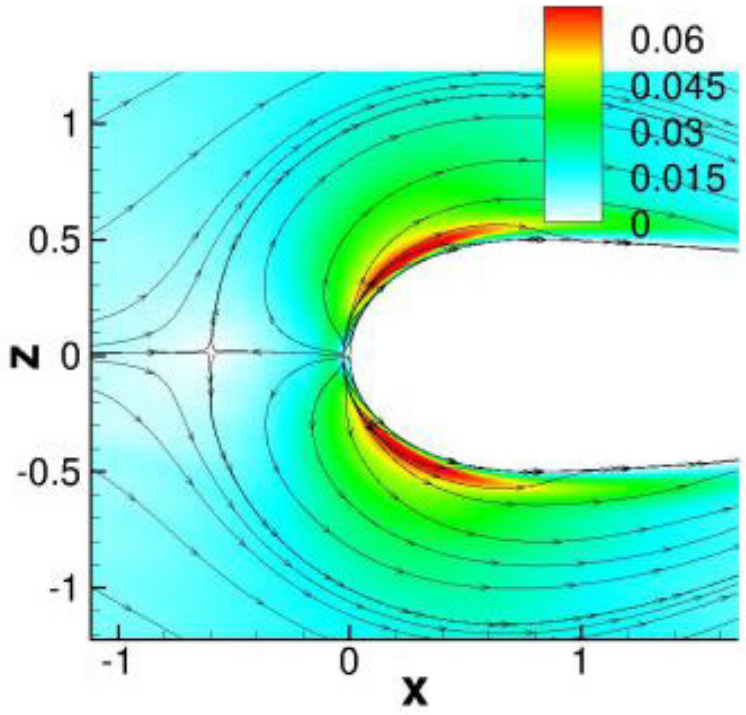
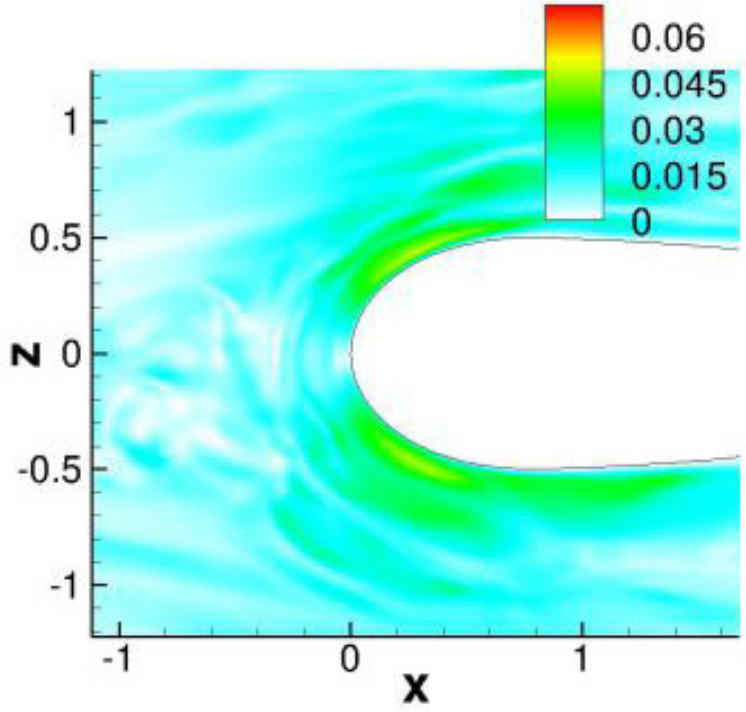


Figure 11: Streamlines in symmetry plane.

DISTRIBUTION STATEMENT A. Approved for public release. Distribution is unlimited.



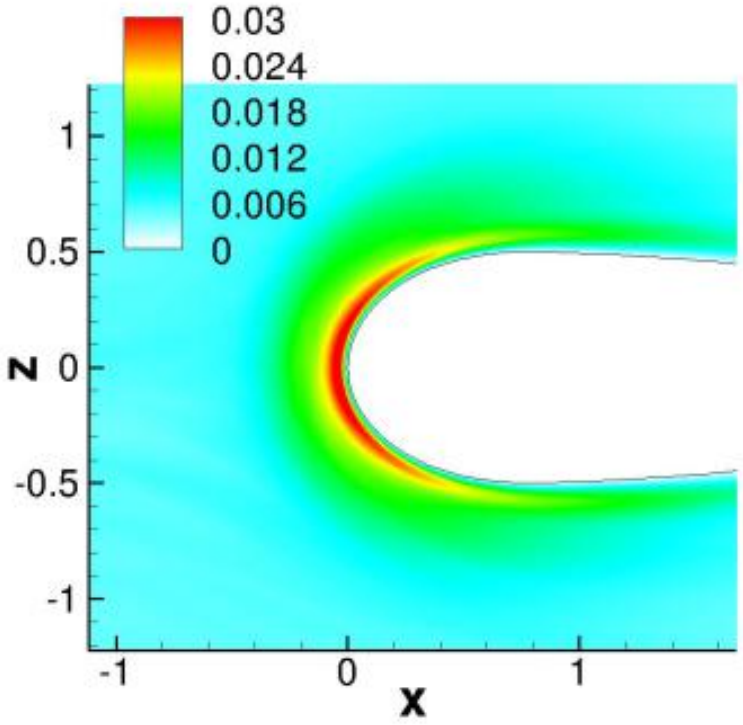
a)



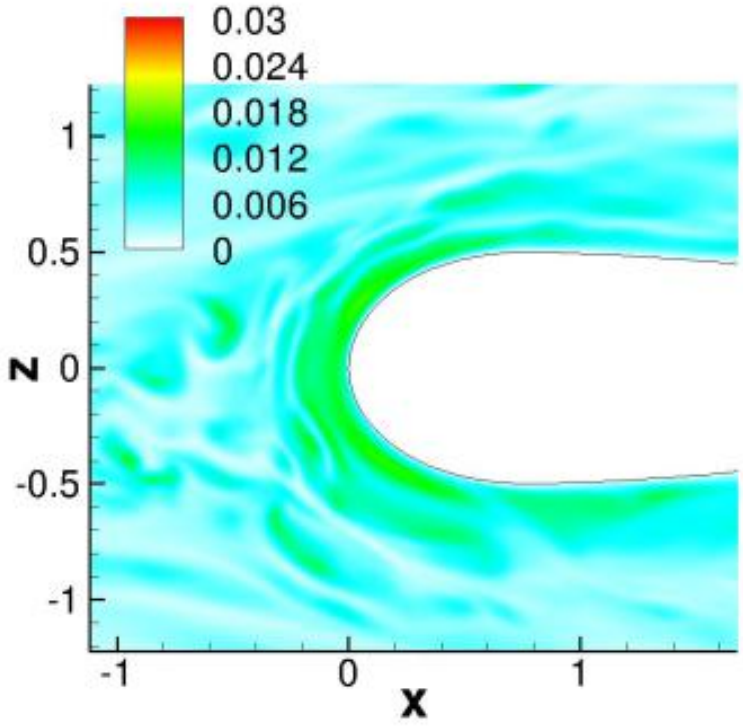
b)

Figure 12: Skin-friction coefficient magnitude iso-contours and skin-friction lines for a) time-average and b) instantaneous flow.

DISTRIBUTION STATEMENT A. Approved for public release. Distribution is unlimited.



a)



b)

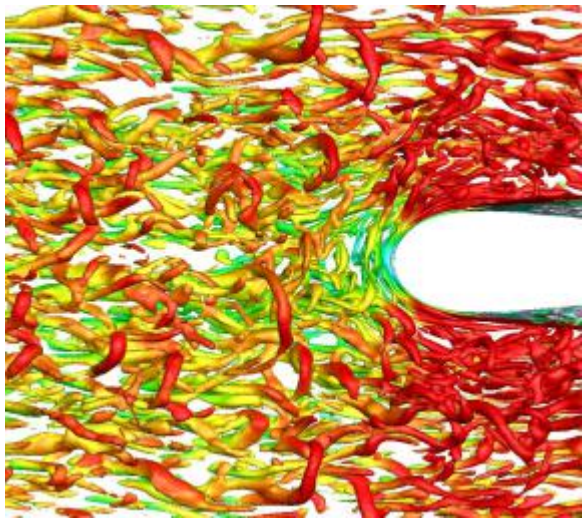
Figure 13: Stanton number computed from a) time-averaged and b) instantaneous flow field.

DISTRIBUTION STATEMENT A. Approved for public release. Distribution is unlimited.

4.4 Analysis of Unsteady Flow

An instantaneous visualization of the unsteady flow field reveals multiple hairpin vortices upstream of the junction (Figure 14a). Hairpin vortices are common to turbulent BLs. The visualization of the time-averaged flow field exhibits two counter-rotating vortical flow structures (Figure 14b). The outer structure appears to have two co-rotating cores which is a consequence of the bimodal behavior. Because of the short duration of the time-averaging interval, the structures are not perfectly symmetric. The inner structure has the opposite sense of rotation and corresponds to the smaller secondary vortex in Figure 11.

a)



b)

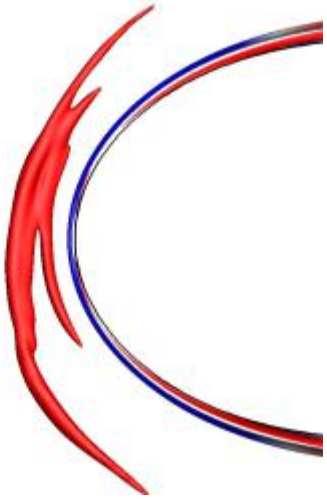


Figure 14: Iso-surfaces of a) Q=0.5 flooded by streamwise velocity (instantaneous flow) and b) Q=6 flooded by pitchwise vorticity, ω_y (time-averaged flow).

Velocity data were recorded at several different locations in the symmetry plane. In Figure 15 the kinetic energy of the velocity fluctuations, $k = 1/2(u'^2 + v'^2 + w'^2)$ is plotted versus time. For a location far upstream of the interaction (x=4) the kinetic energy contained in the fluctuations is less than 0.1. Location x=0.6 is close to the saddle point and locations x=0.4 and x=0.2 are in the reverse flow region. The data for x=0.6 and x=0.4 appear correlated. For example, both time

DISTRIBUTION STATEMENT A. Approved for public release. Distribution is unlimited.

series show peaks near t=90. The data for x=0.2 displays the largest spikes and appears uncorrelated to the other time series. For the time instances when the x=0.2 data show peaks, the HV is relatively coherent and far forward of the junction (Figure 16). At time instances when the x=0.2 fluctuations are low, the HV is located closer to the Rood wing (Figure 17). In between, time instances can be identified when the HV coherence is very low, which implies that the flow is in the zero-flow state (Figure 18).

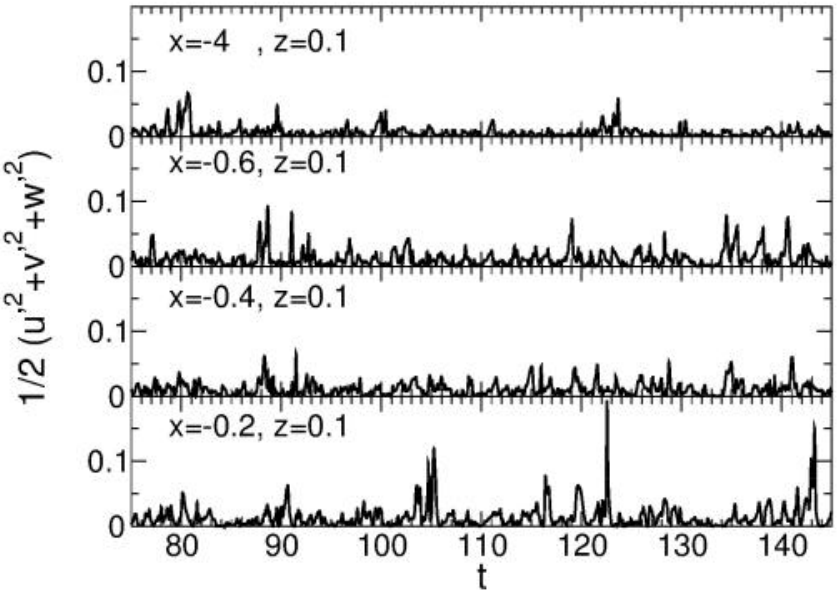


Figure 15: Instantaneous turbulence kinetic energy.

DISTRIBUTION STATEMENT A. Approved for public release. Distribution is unlimited.

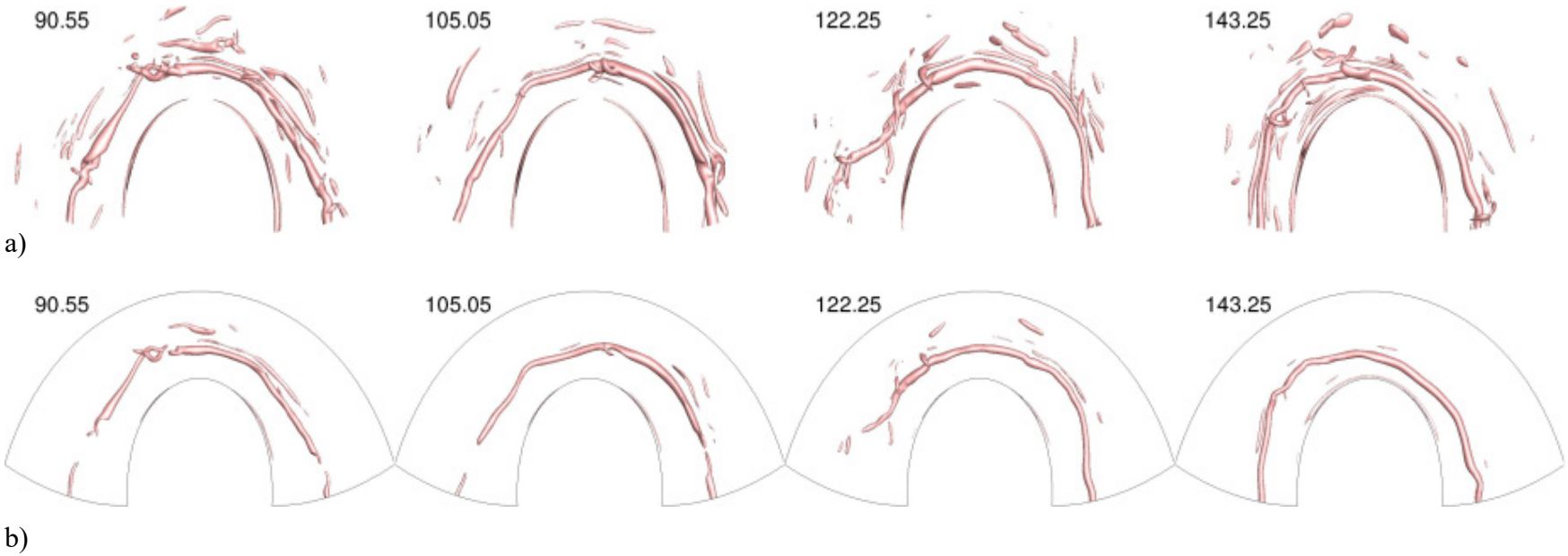


Figure 16: Instantaneous iso-surfaces of a) Q=1 (top) and b) 100 (bottom).

DISTRIBUTION STATEMENT A. Approved for public release. Distribution is unlimited.

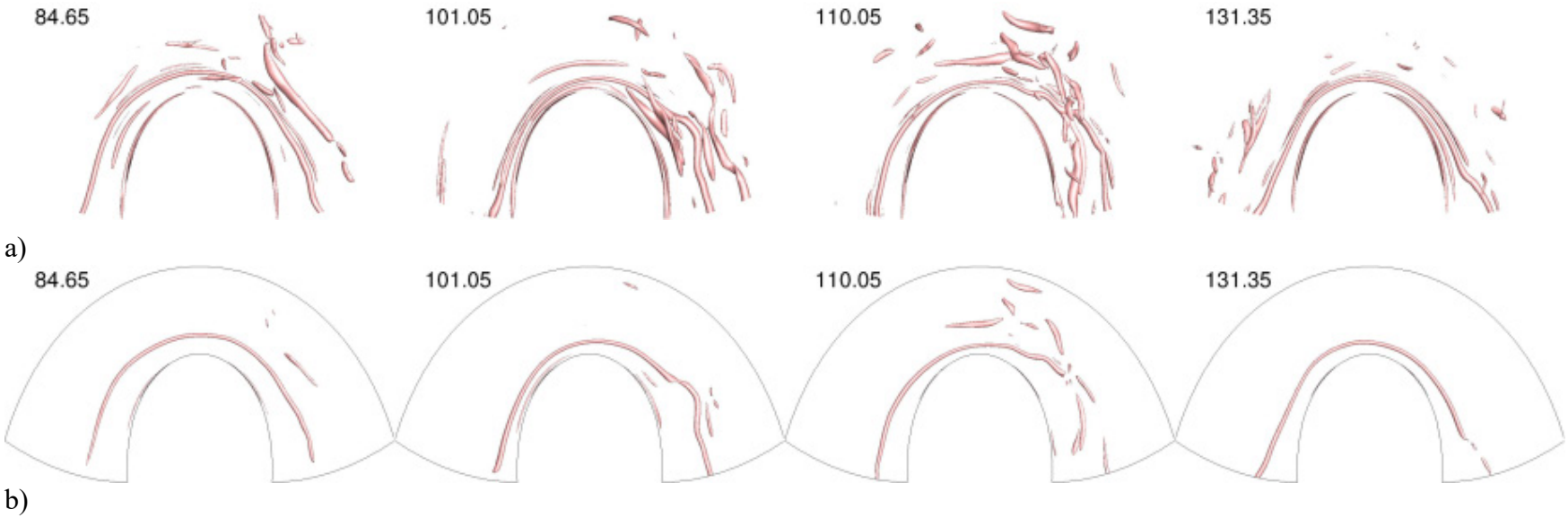


Figure 17: Instantaneous iso-surfaces of a) Q=1 (top) and b) 100 (bottom).

DISTRIBUTION STATEMENT A. Approved for public release. Distribution is unlimited.

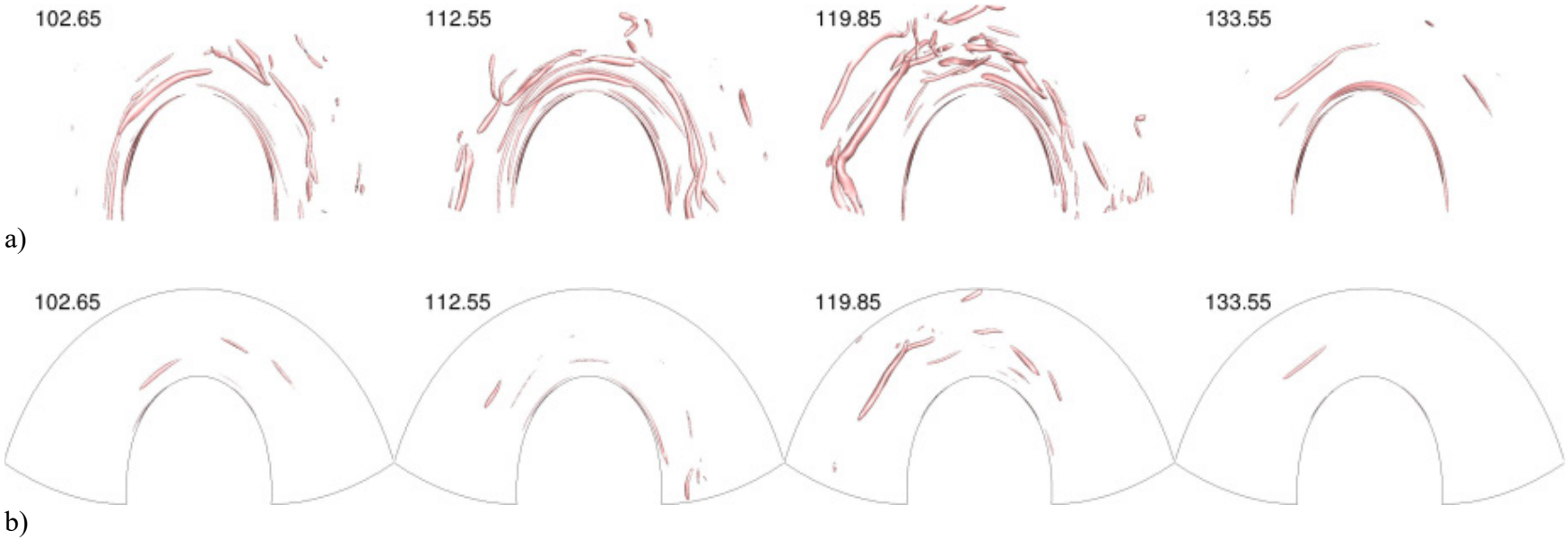


Figure 18: Instantaneous iso-surfaces of a) Q=1 (top) and b) 100 (bottom).

DISTRIBUTION STATEMENT A. Approved for public release. Distribution is unlimited.

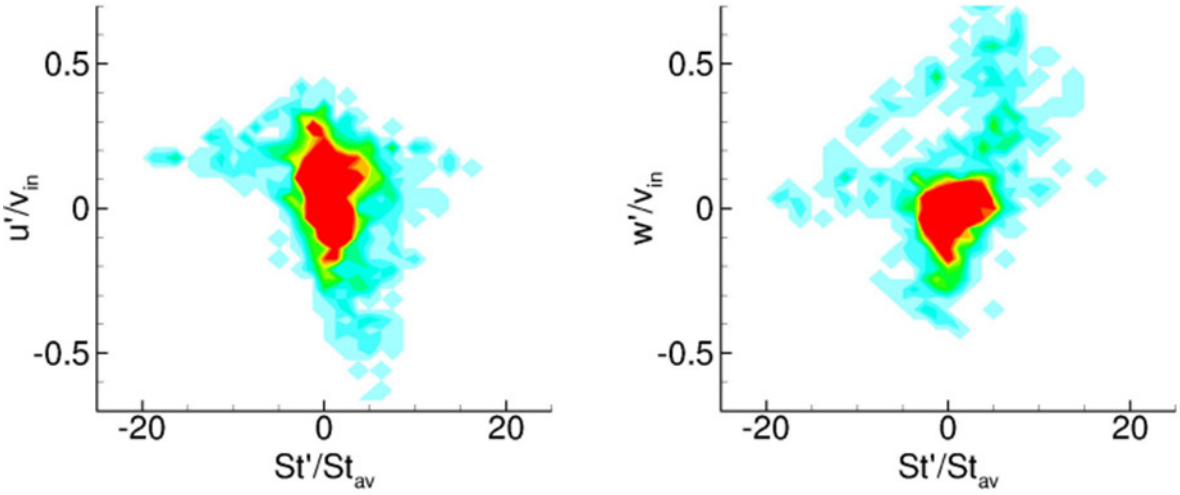


Figure 19: Histogram of velocity fluctuations at (x,y,z) = (0.1,0,0.025) and Stanton number fluctuations at (x,y,z) = (0.1,0,0).

The PSU experiments revealed that the heat flux fluctuations were related to the spanwise but not the streamwise velocity fluctuations. Histograms of the velocity fluctuations, u' and w', at $(x, y, z) = (0.1, 0, 0.025)$ and the heat flux fluctuations, St', at $(x, y, z) = (0.1, 0, 0)$ in the symmetry plane were generated from the LES data (Figure 19). In agreement with the experiment, the w-velocity fluctuations appear to be more strongly correlated with the Stanton number fluctuations than the u-velocity fluctuations.

To more quantitatively describe the behavior of the HV in the symmetry plane, a computer program was developed that finds the maximum of the Q-criterion, Q_{max}, in the symmetry plane and identifies it with the location of the core, x_c, z_c, of the HV if the pitchwise vorticity, ω_y, is positive. Starting from the center of the core, the streamwise and wall-normal extent of the HV were then estimated based on the points were Q dropped below $0.1Q_{max}$. The HV circulation was computed as $\Gamma = \int \omega_y dA$ where A was approximated as the quadratic area spanned by the streamwise and wall-normal extent. Figure 20 reveals that the HV is repeatedly moving back and forth and experiencing strong fluctuations of both Q_{max} and Γ. For time-instances when the circulation is large, the HV is typically located closer to the leading edge of the Rood wing. The frequency of the circulation fluctuations is roughly 0.13. Made dimensionless with the BL thickness upstream of separation, $\delta = 0.88$, a frequency of 0.11 is obtained which falls roughly in the range reported by Gand et al. [21] ($0.05 < f\delta/v_{in} < 0.1$). Figure 21 provides instantaneous flow visualizations for time instances when the circulation attains maxima and minima. For the former, the HV is located close to $x = 0.1$ while for the latter the HV is noticeably absent. A strong HV implies that the flow is in the back-flow state while a weak or entirely missing HV implies that the flow is in the zero-flow state. A time-sequence that shows the development towards a strong HV at $t = 122.95$ and then back toward a weak HV at t=125.45 is provided in Figure 22.

DISTRIBUTION STATEMENT A. Approved for public release. Distribution is unlimited.

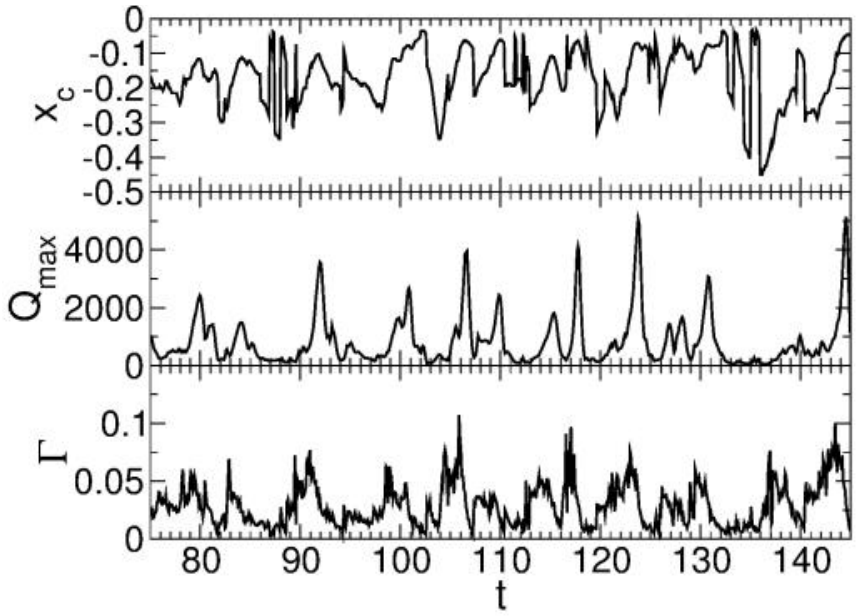


Figure 20: Vortex core location, maximum Q-criterion, and circulation of horseshoe vortex.

DISTRIBUTION STATEMENT A. Approved for public release. Distribution is unlimited.

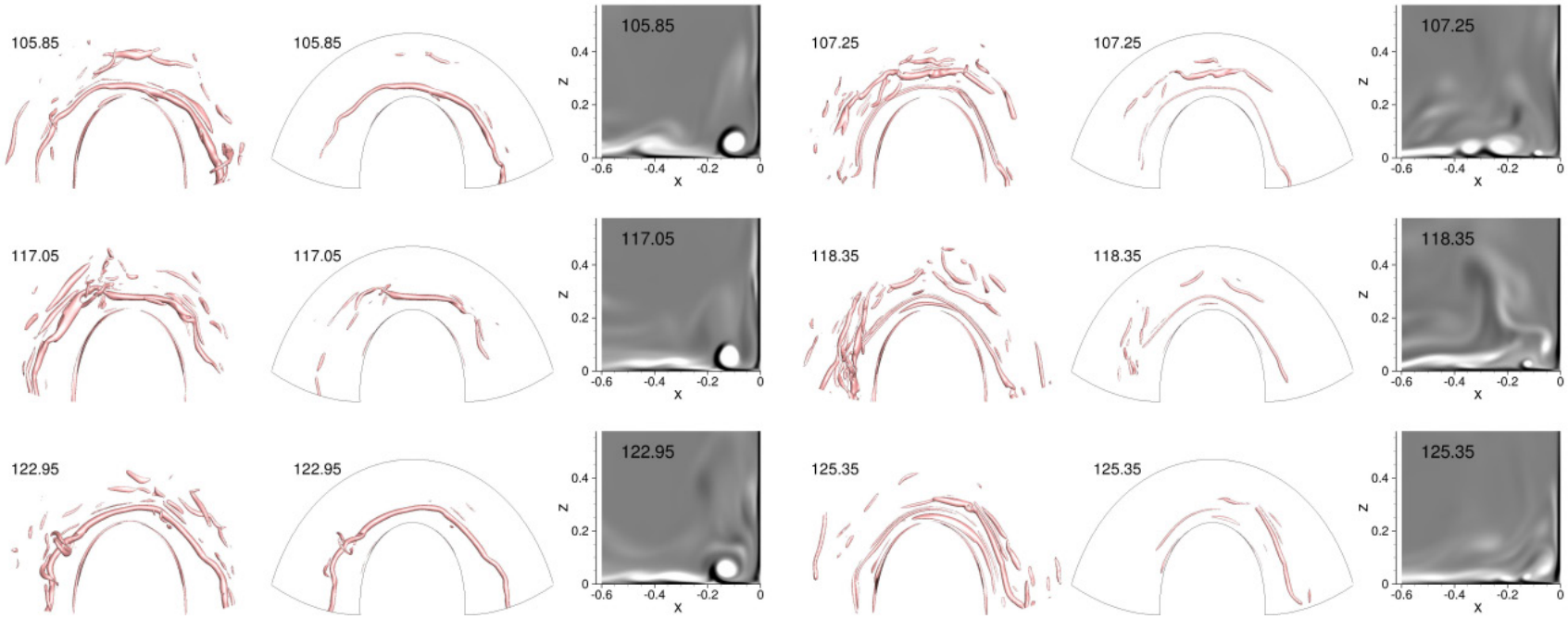


Figure 21: Instantaneous iso-surfaces of Q=1, Q=100, and iso-contours of pitchwise vorticity, ω_y, in symmetry plane.

DISTRIBUTION STATEMENT A. Approved for public release. Distribution is unlimited.

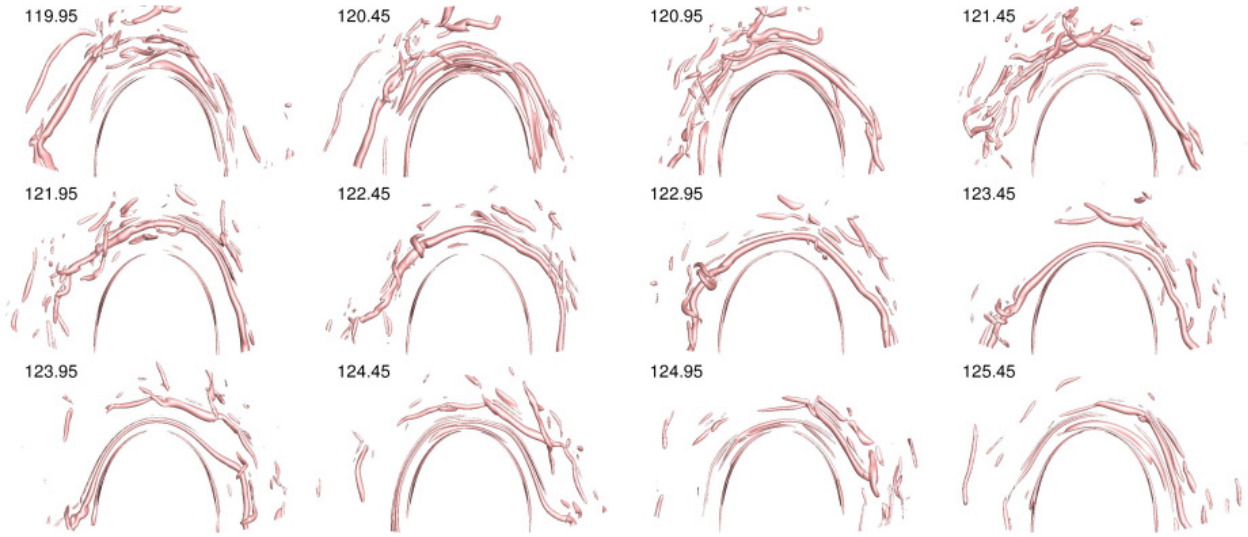
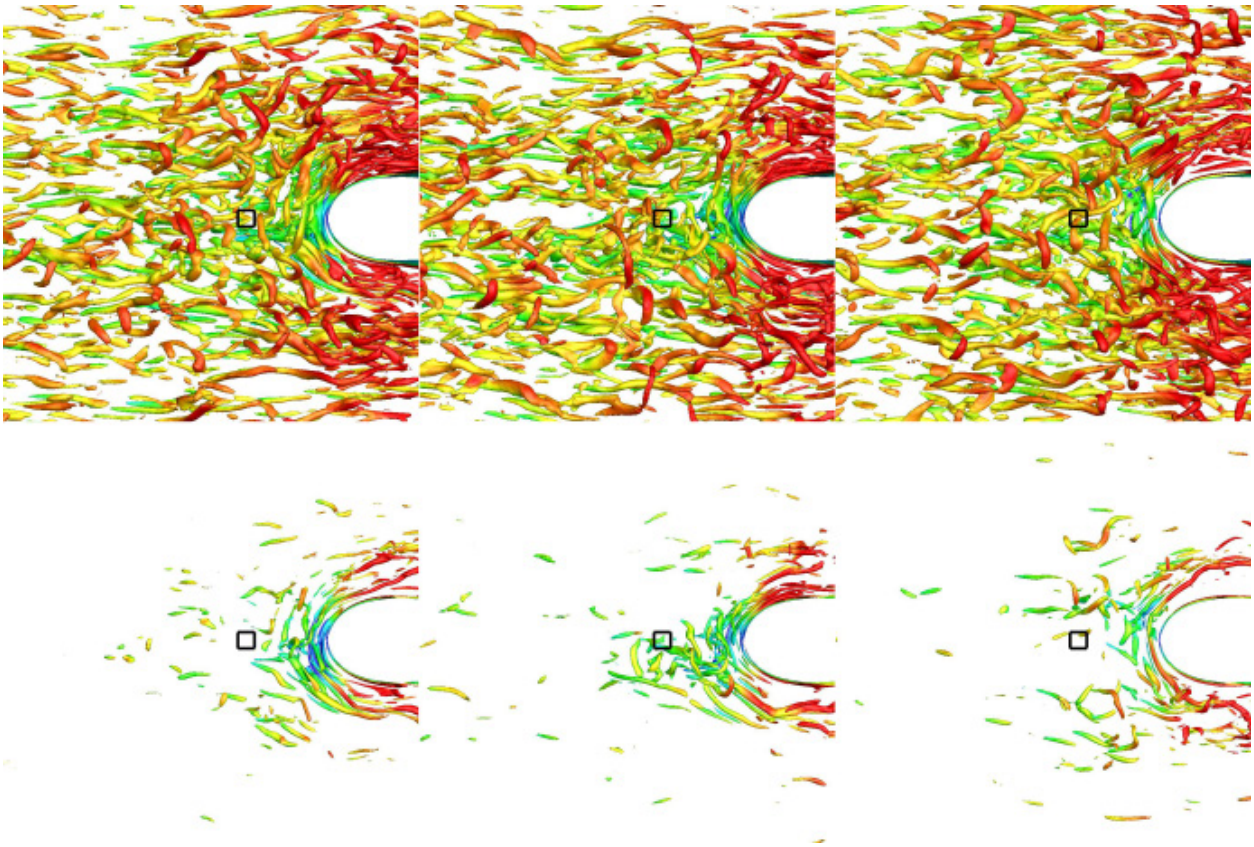


Figure 22: Instantaneous iso-surfaces of Q=1.

The flow visualizations indicate that lumps of highly elevated turbulence are hitting the interaction region at random locations and time-instances. For example, at $t = 119.95$, a region of elevated turbulence is impacting the left of the leading edge region. This raises the question if upstream BL events (bursts and ejections) are responsible for the intermittent loss of coherence of the HV. Visualizations of the upstream boundary layer in Figure 23 again show that for $t = 119.7$ a packet of highly turbulent flow is impacting the junction region. At other time instances (e.g., $t = 116.0$ and 123.0) the approach flow BL turbulence is noticeably reduced.

DISTRIBUTION STATEMENT A. Approved for public release. Distribution is unlimited.



t=116.0 t=119.7 t=123.0

Figure 23: Iso-surfaces of Q=1 (top) and 10 (bottom) flooded by streamwise velocity. Box indicates area over which VITA data for x=1 in Figure 26 were averaged.

The VITA method was employed to detect upstream BL events. In Figure 24 the VITA value was computed from the streamwise skin-friction coefficient, $c_{f,x}$, and the integrals Eqs. 14 and 15 were computed over the time interval $T^+ = 8.6$ as suggested in the literature [26]. For the computation of the dimensionless time based on freestream velocity and maximum thickness,

$$\boldsymbol{T = \frac{1}{Re}\frac{v_w}{v_\tau^2}T^+},$$

(23)

the friction velocity, u_r, was averaged over an area of $-2.6494 < x < -2$ and $-2 < y < 2$ upstream of the Rood wing (Figure 23). The averaging time constitutes 12% of the total simulation time. The VITA-distributions looked "smeared out" in the streamwise direction and do not allow for an accurate identification of BL events (Figure 24). To make the VITA method more sensitive to short duration events, T^+ was lowered to one. Contours of the VITA method computed from the wall pressure coefficient, streamwise skin-friction coefficient, and Stanton number are provided in Figure 25. For all three quantities, the VITA method with $T^+ = 1$ identifies the turbulent event that strikes the junction flow region at $t = 119.7$.

DISTRIBUTION STATEMENT A. Approved for public release. Distribution is unlimited.

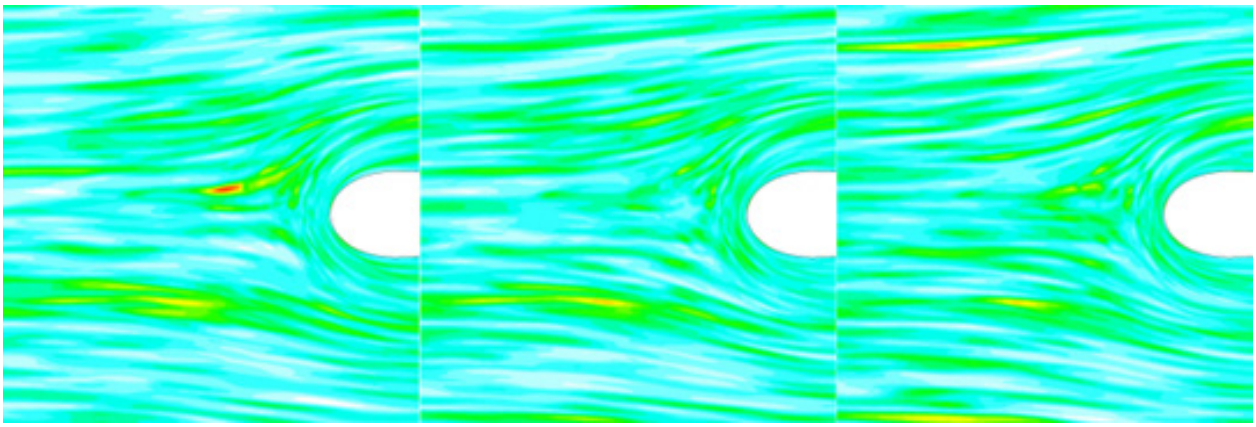


Figure 24: Iso-contours of 0< VITA < 6 (with T^+=8.6) computed from $c_{f,x}$.

DISTRIBUTION STATEMENT A. Approved for public release. Distribution is unlimited.

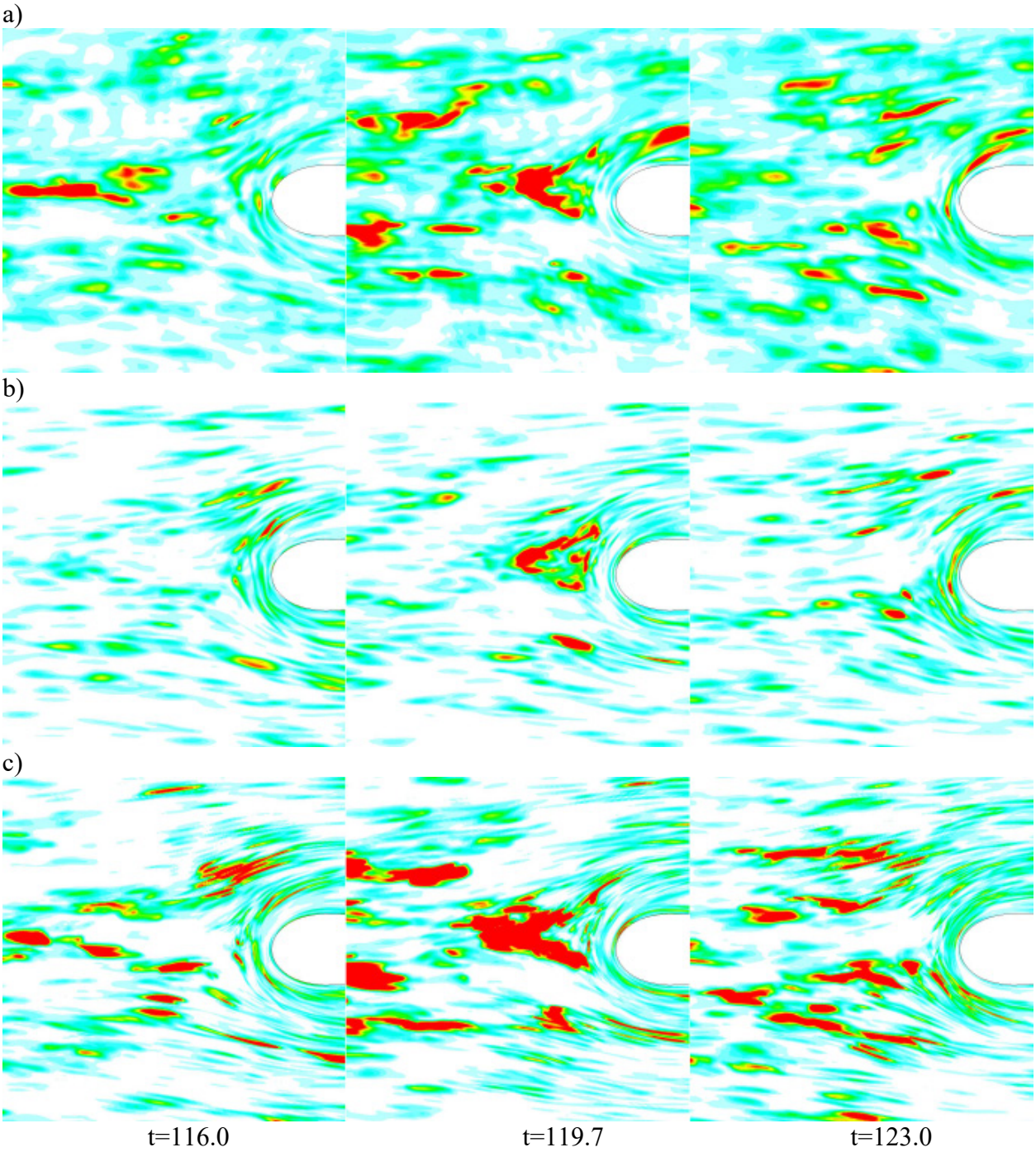


Figure 25: Iso-contours of 0 ≤ VITA ≤ 6 (with T^+=1) computed from a) c_p, b) $c_{f,x}$, and c) St.

DISTRIBUTION STATEMENT A. Approved for public release. Distribution is unlimited.

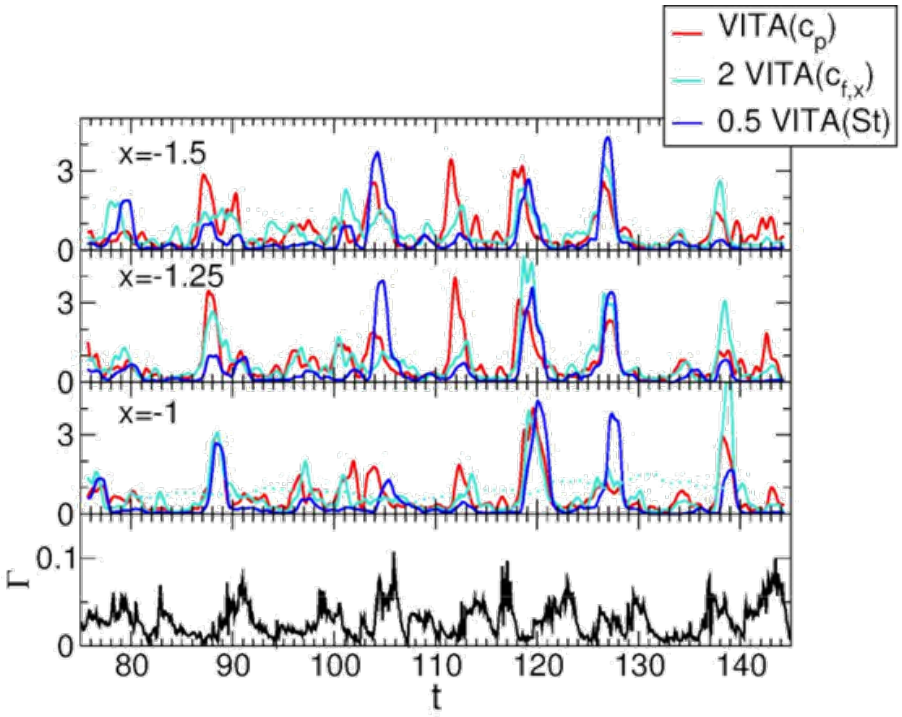


Figure 26: Averages of VITA data (T^+=1, dotted line is for T^+=8.6) for three upstream locations and HV circulation.

In Figure 26 spatial averages (for $x \pm 0.1$ and $y \pm 0.1$) of the VITA method for 3 upstream locations (x as indicated and y = 0) are compared with the HV circulation. The magnitude of the VITA results for the skin-friction were doubled and the results for the Stanton number were halved to approximately normalize the amplitudes. Also included is the VITA result for $T^+ = 8.6$ which shows little variation in time. The majority but not all of the events identified by the VITA method are followed by maxima of the circulation which suggests that the vorticity contained in the turbulent flow structures (e.g., hairpin vortices) is absorbed into the HV as suggested by Sabatino and Smith [15]. The snapshots series in Figure 22 reveals how a highly turbulent packet impacts the junction area slightly off-center around $t = 120$ and then passes the airfoil to the left. In the process, first the right hand side and then the entire HV becomes more coherent. At $t = 122.95$ the HV circulation reaches a maximum. The HV then migrates towards the leading edge and loses coherence. As a result, the circulation drops (Figure 20). Unfortunately, these observations do not conclusively answer the question if the switch between the zero-flow and back-flow mode is triggered by upstream BL events. The switch could have occurred despite the impact of the turbulent packet.

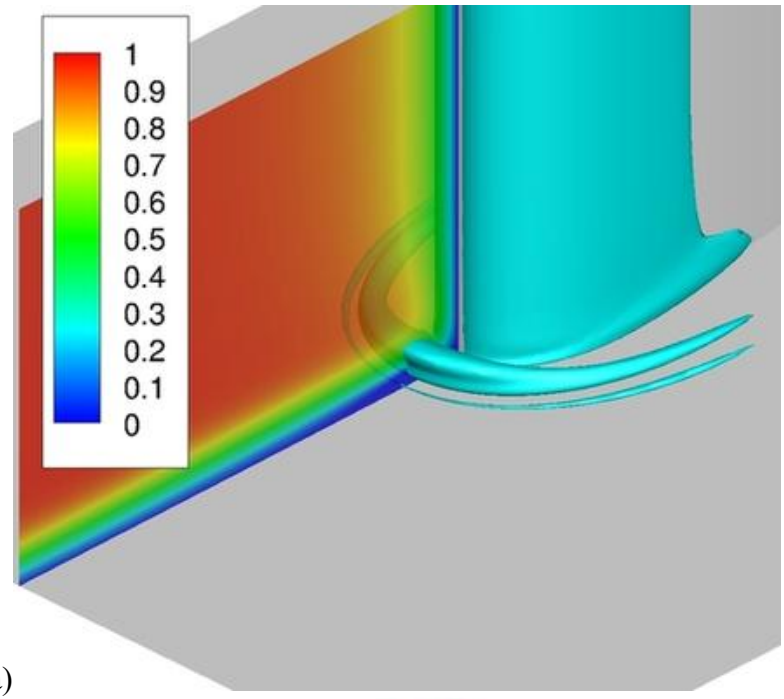
4.5 Simulation of Laminar Junction Flow

Since prior research (Devenport and Simpson [3], Praisner and Smith [13], and Agui and Andreopoulos [12]) suggests that the bimodal behavior is related to the incoming turbulent BL structures, a simulation with laminar BL was performed to see if the bimodal behavior persists if the upstream flow is steady. For this simulation, the reference Reynolds number was lowered to 1,000 and a Blasius BL profile was prescribed at the block 1 inflow (x=4.239). The dimensionless momentum thickness of the profile was matched to the momentum thickness of

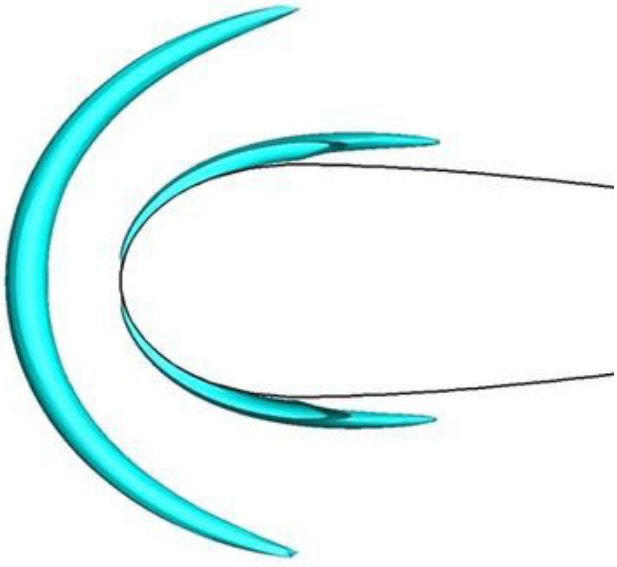
DISTRIBUTION STATEMENT A. Approved for public release. Distribution is unlimited.

the turbulent profile at the same location ($\vartheta/t = 0.0805$). The block 1 grid resolution was lowered by a factor of two in all three dimensions to save computational time. Blocks 2 and 3 were not employed for the laminar simulation.

Flow visualizations were obtained to confirm that the incoming BL remained steady and to investigate the dynamics of the HV. Figure 27a illustrates the HV location relative to the laminar BL at the end of the simulation. The endwall BL separates ahead of the junction and the core of the HV is located in the outer part of the separated BL. The HV wraps around the leading edge as seen in Figure 27b.



a)



b)

Figure 27: Laminar junction ow: a) Iso-surfaces of Q=0.5 and u-velocity contours in symmetry plane. b) Iso-surfaces of Q=2.

DISTRIBUTION STATEMENT A. Approved for public release. Distribution is unlimited.

A smaller secondary vortex with opposite sense of rotation can be distinguished closer to the junction. The legs of the secondary vortex develop into two corner separation vortices downstream of the leading edge.

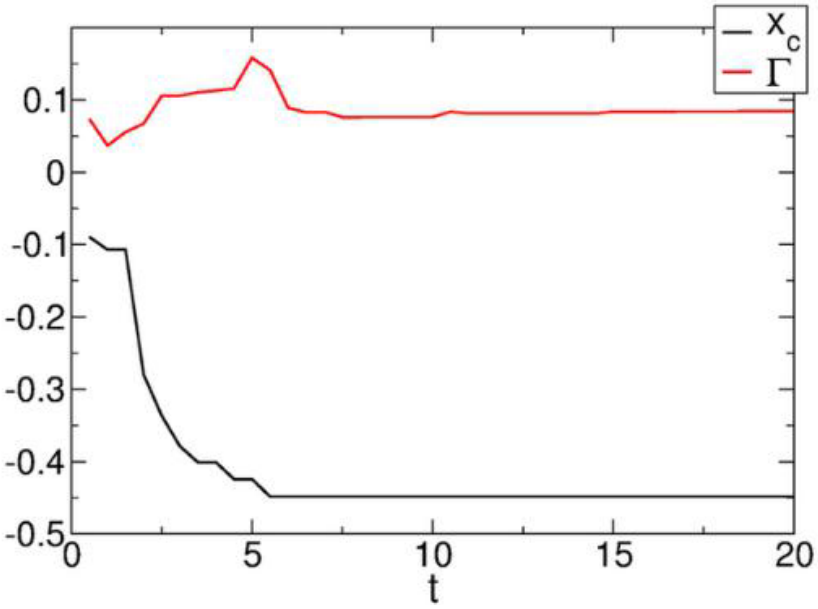


Figure 28: Laminar junction flow: Streamwise core position and circulation of HV in symmetry plane.

The circulation and streamwise position of the HV core in the symmetry plane are shown in Figure 28. Initially, the HV is unsteady and moves far ahead of the leading edge. Around t=5, the HV comes to a rest at $x_c \approx 0.45$ and the circulation converges to a value of $\Gamma \approx 0.082$. Although these findings provide additional support for the statement that the bimodal behavior is absent for laminar interactions, they do not allow for conclusions regarding the dependence of the bimodal behavior of turbulent junction flows on upstream turbulent BL events.

DISTRIBUTION STATEMENT A. Approved for public release. Distribution is unlimited.

5 ACTIVE FLOW CONTROL

5.1 Generation of Boundary Layer Events - Active Flow Control

Unsteady jets were issued into the turbulent BL upstream of the interaction region to seed deterministic turbulent BL events. All forced cases were started from the same instantaneous uncontrolled flow field. The jets were generated by wall-normal blowing through circular holes with diameter $D = 0.4$. Figure 29 shows outlines of the circular holes. The assumption was made that the jets would bring the turbulent BL out of equilibrium and that the BL would slowly recover equilibrium in the downstream direction. For investigating the effect of the disturbances on the junction flow physics, it is desirable that the disturbances still have an appreciable amplitude when they they reach the HV. Therefore, the decision was made to place the jets not too far upstream of the leading edge. Several different cases were considered. For cases a-e, one jet was situated in the symmetry plane ($y = 0$); for case f, three jets were aligned in the transverse direction ($y = -0.4, 0, and\ 0.4$); for case g, three jets were aligned in the streamwise direction ($x = -3.05, -2.65, and\ -2.25$). The jets were pulsed with a reduced duty cycle of $\tau = 4\%$. The jet pitch angle was 90 deg (wall-normal injection). The streamwise location, period, and blowing ratio for the different cases are listed in Tab. 3. The momentum coefficient

$$c_\mu = \frac{\frac{1}{T}\int_T \int_A \rho u^2 dA dt}{\frac{1}{2}\rho v_{in} A_{ref}} \tag{24}$$

based on a reference area of $A_{ref} = ct$ is provided in Tab 3.

A systematic parameter study was carried out for case b to determine the most appropriate VITA settings for detecting BL events immediately upstream of the interaction. Three different endwall areas (for averaging the VITA value; see Figure 30 and Tab. 4) and three different time averaging intervals, T_{av}, were considered. All VITA values were computed from the fluctuations of the streamwise skin-friction coefficient, $c'_{f,x}$.

DISTRIBUTION STATEMENT A. Approved for public release. Distribution is unlimited.

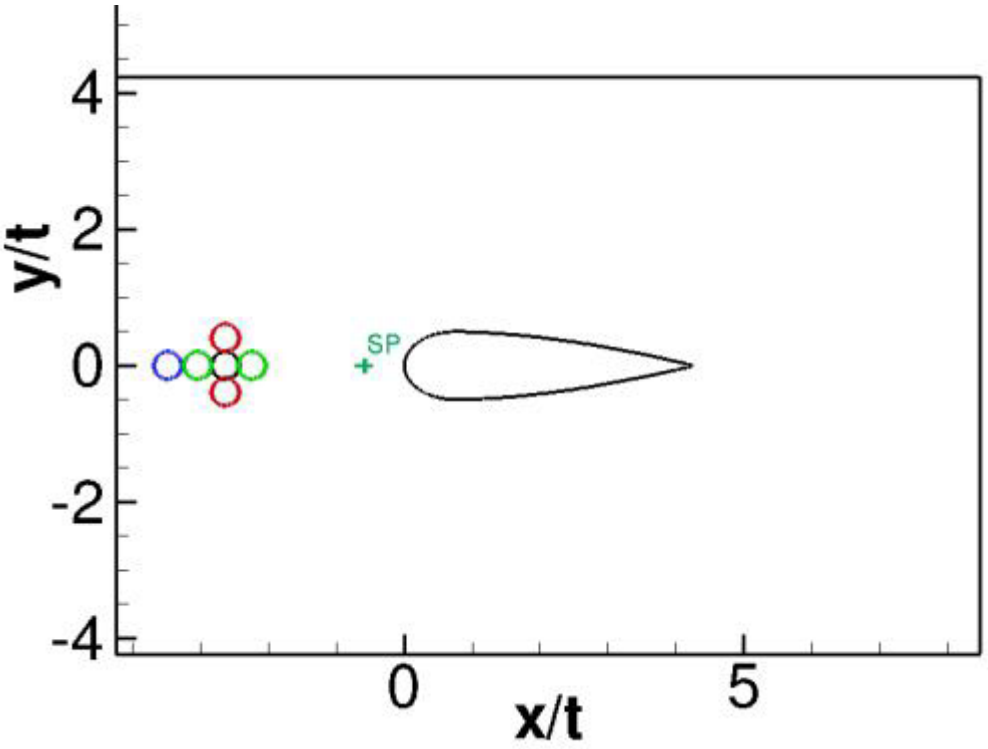


Figure 29: Jet locations. Cases a, b, c, e: Black circle; Case d: Blue circle; Case f: Black and red circles; Case g: Black and green circles. Green "+" symbol indicates saddle point of skin-friction lines.

The VITA responses for the different settings are compared in Figure 31. Because the forcing for case b has a period of 7.5, the VITA response should inherit this period. Immediately downstream of the jet location (box 1), the VITA value follows the forcing signal closely, especially for the shortest time averaging interval. For higher values of T_{av}, the peaks associated with the forcing become "smeared out". The further away the box (Figure 30) is placed from the jet location, the less closely the VITA value follows the forcing signal. For box 3, the peaks at t=262.5 and 285 are missing and the peak at 277.5 is split in half.

Table 3: Forcing parameters.

Case	*x-location*	*Period, T*	*Blowing ratio, B*	c_μ
a	-2.65	5	1	0.0007375
b	-2.65	7.5	1	0.0007375
c	-2.65	7.5	2	0.0095000
d	-3.5	7.5	1	0.0007375
e	-2.65	10	1	0.0007375
f	-2.65	7.5	1	0.007150
g	-2.65	7.5	1	0.007150

DISTRIBUTION STATEMENT A. Approved for public release. Distribution is unlimited.

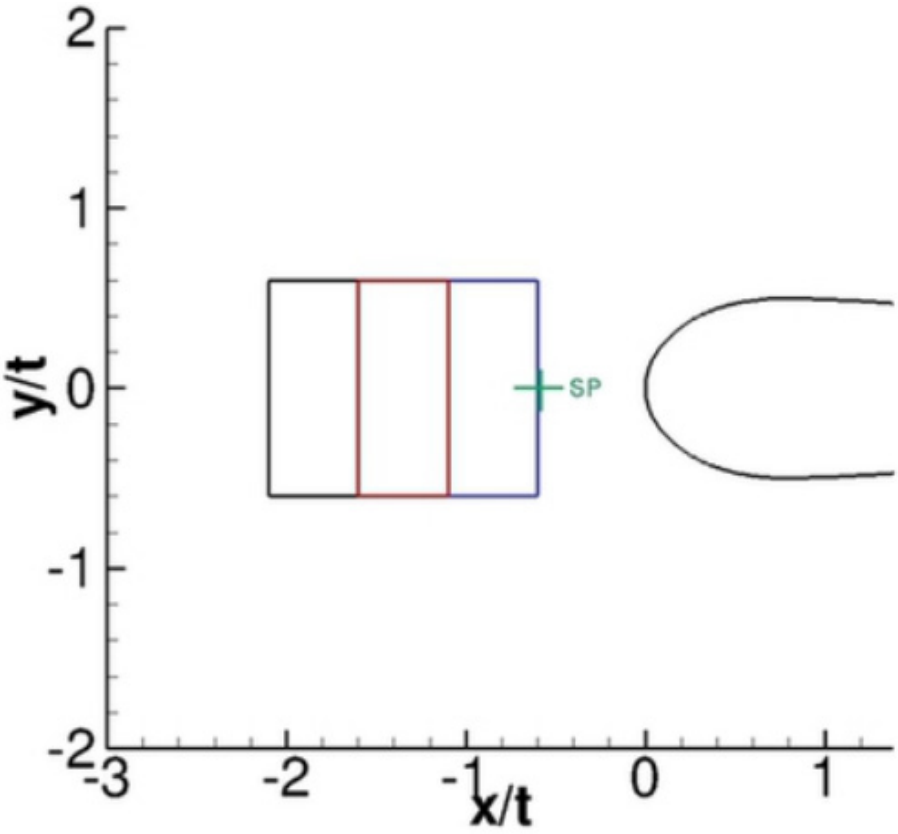


Figure 30: Endwall areas for averaging of VITA value. Saddle point illustrated by green “+" symbol.

DISTRIBUTION STATEMENT A. Approved for public release. Distribution is unlimited.

Table 4: Endwall areas for averaging of VITA value.

Reference	*Outline*	*Coordinates*			
Box 1	Black	2.1	< x <	1.6	0.6 < y < 0.6
Box 2	Red	1.6	< x <	1.1	0.6 < y < 0.6
Box 3	Blue	1.1	< x <	0.6	0.6 < y < 0.6

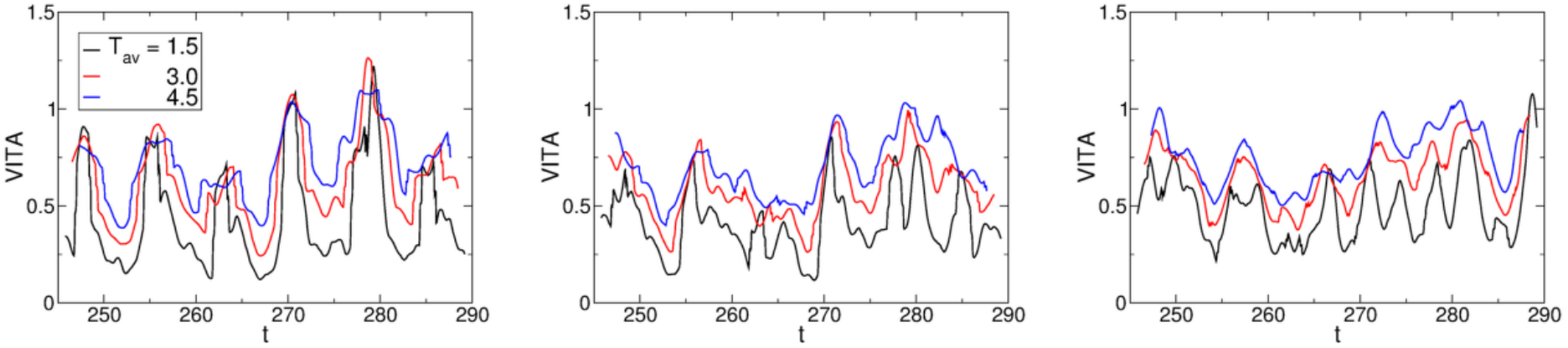


Figure 31: Case b: Dependence of VITA value on endwall area (Figure 30) and time averaging interval, T_{av}.

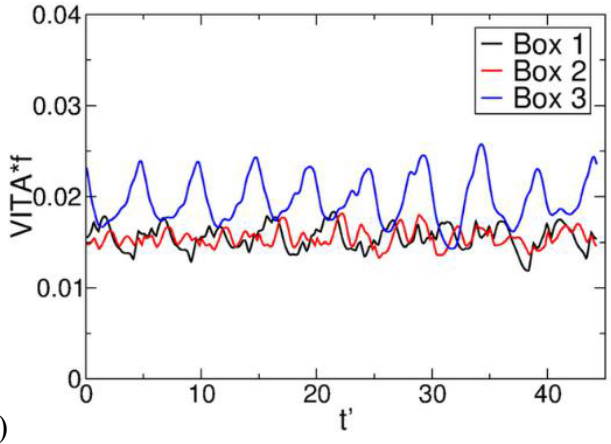
DISTRIBUTION STATEMENT A. Approved for public release. Distribution is unlimited.

For cases a, b, e, and f (forcing periods of $T = 5, 7.5, 10, and\ 7.5$, respectively), the cyclic cross-correlation of the VITA value for $T_{av} = 1.5$ with the forcing signal (normalized to one),

$$(\boldsymbol{VITA} * \boldsymbol{f})(\boldsymbol{t'}) = \int \boldsymbol{VITA}(\boldsymbol{t})\boldsymbol{f}(\boldsymbol{t'} + \boldsymbol{t})\boldsymbol{dt}, \quad \textbf{(25)}$$

was computed to quantify how well the BL events were correlated with the actuation. The cross-correlation program was tested for $VITA(t) = sin(2\pi t)$ and $f(t) = sin(2\pi t)$. For this test case, the analytical cross-correlation of $cos(2\pi t)/2$ was recovered. A large spread of the cross-correlation together with a periodicity of the cross-correlation that matches the forcing period are indicators that two signals are well correlated.

For a forcing period of five, weak cross-correlations are obtained for boxes 1 and 2 (Figure 32a). Interestingly, the cross-correlation for box 3 is slightly larger and displays a more defined periodic behavior. A better VITA response is obtained for T=7.5 (Figure 32b). For this forcing period, the strongest cross-correlation is obtained for box 1. For boxes 2 and 3, the cross-correlation becomes progressively weaker which may be attributed to the slow recovery of boundary layer equilibrium in the streamwise direction. For a forcing period of T=10 (Figure 32c), the cross-correlations between the VITA value and the forcing signal are overall slightly weaker than for T=7.5 (Figure 32b). The strongest cross-correlations are obtained for case f (three jets; T=7.5). However, even for this case the cross-correlations are quickly getting weaker in the streamwise direction (Figure 32d). The shift between the maxima for boxes 1 and 3 is about $\Delta t' \approx 2$. Since the centers of the boxes are at x=-1.85, -1.35, and -0.85, this suggests that the disturbances are convected with a streamwise velocity of $1/2 \approx 0.5$.



a)

DISTRIBUTION STATEMENT A. Approved for public release. Distribution is unlimited.

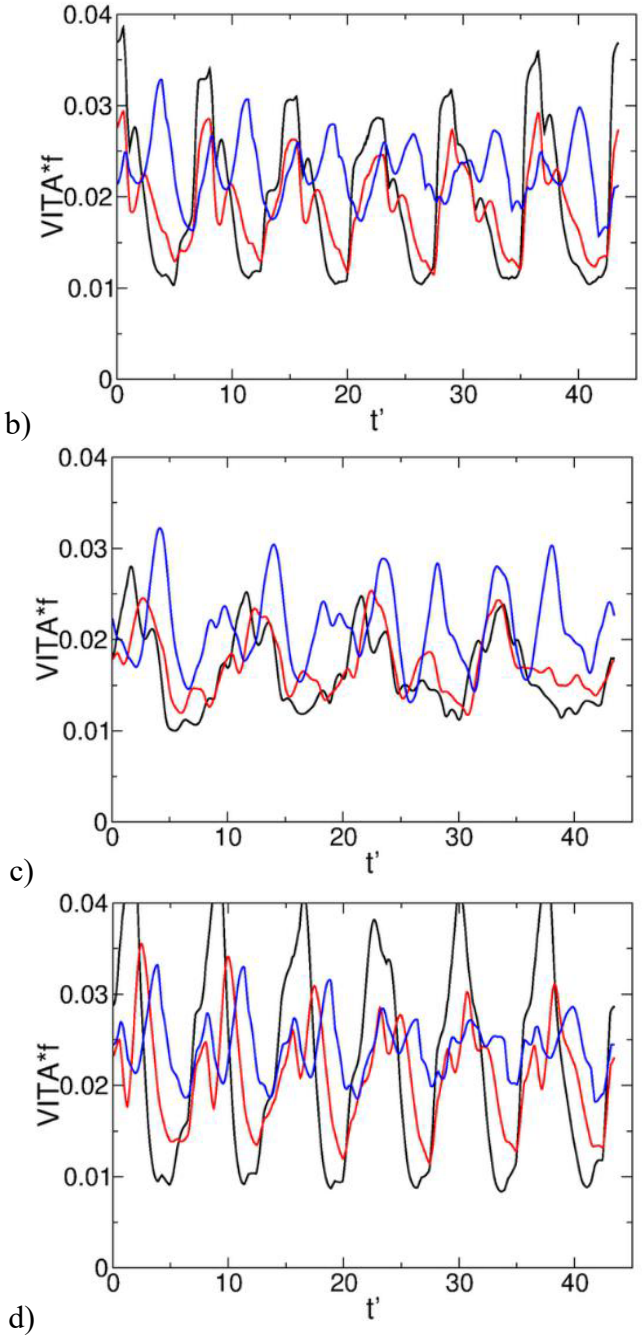


Figure 32: Cross-correlation of VITA value with normalized forcing signal for a) case a, b) case b, c) case e and d) case f.Horseshoe Vortex Behavior Cross-Correlations

Instantaneous visualizations of the Q-criterion by Hunt et al. [43] were generated to track the downstream development of the disturbances for cases a and f (Figures 33 and 34). Similar flow visualizations were also generated for the other cases but are not shown here for the sake of brevity. A Q-level of two was employed to visualize disturbances embedded in the turbulent BL and a Q-level of eight was used to highlight the disturbances related to the forced BL events. The $t = 245$ images in Figure 33 show the "plume" resulting from a single jet ejection. For $246 \leq$

DISTRIBUTION STATEMENT A. Approved for public release. Distribution is unlimited.

$t \leq 247$ this disturbance travels downstream and develops into a hairpin vortex. The hairpin "breaks up" for $t = 248$ and leaves behind a region of elevated turbulence which strikes the leading edge at $t = 249$.

Visualizations for case f (three transverse jets) are provided in Figure 34. The row of jets generates three hairpin vortices that are clearly visible for $t = 248.5$. The lower two vortices approach each other for $t = 249.5$ and for $t = 250.5$, both the upper hairpin and the pair of the lower two hairpins disintegrate and leave behind two areas of increased turbulence that strike the leading edge region at $t = 251.5$. From these images and the time stamps, it was concluded that the disturbances impact the junction region about four time units after they were generated. Since the jets were located at a distance of 2.65 upstream of the leading edge, this implies a convection velocity of $2.65/4 \approx 0.6$ which is close to the value estimated from the VITA results (Figure 32d). Visualizations for case g (three streamwise jets) are provided in Figure 35. Like case f, all three jets produce hairpin vortices that can be easily seen at $t = 248.5$. Because the jets are aligned in the streamwise direction, as the flow approaches the leading edge and slows down, the hairpins appear to interact with one another as seen for $t = 250.5$ and $t = 251.5$. The structures resulting from the forcing are no longer visible for $t = 252.5$.

To quantify the effect of the BL events on the bimodal behavior of the HV, the cross-correlation of the VITA value and the HV circulation in the symmetry plane,

$$(\boldsymbol{VITA} * \boldsymbol{\Gamma})(\boldsymbol{t'}) = \int \boldsymbol{VITA}(\boldsymbol{t})\boldsymbol{\Gamma}(\boldsymbol{t'} + \boldsymbol{t})\boldsymbol{dt}, \tag{26}$$

was computed. For all cases, the VITA value was obtained for boxes 1 and 3 and $T_{av} = 1.5$. The uncontrolled flow is discussed first, since it provides a reference for the forced cases (Figure 36). Both the VITA values and the circulation show a distinct low-frequency oscillation. The associated dominant frequencies are f=0.12 (based on VITA for box 1), 0.12 (box 3), 0.13 (based on circulation), 0.12 (based on cross-correlation for box 1), and 0.12 (based on cross-correlation for box 3).

DISTRIBUTION STATEMENT A. Approved for public release. Distribution is unlimited.

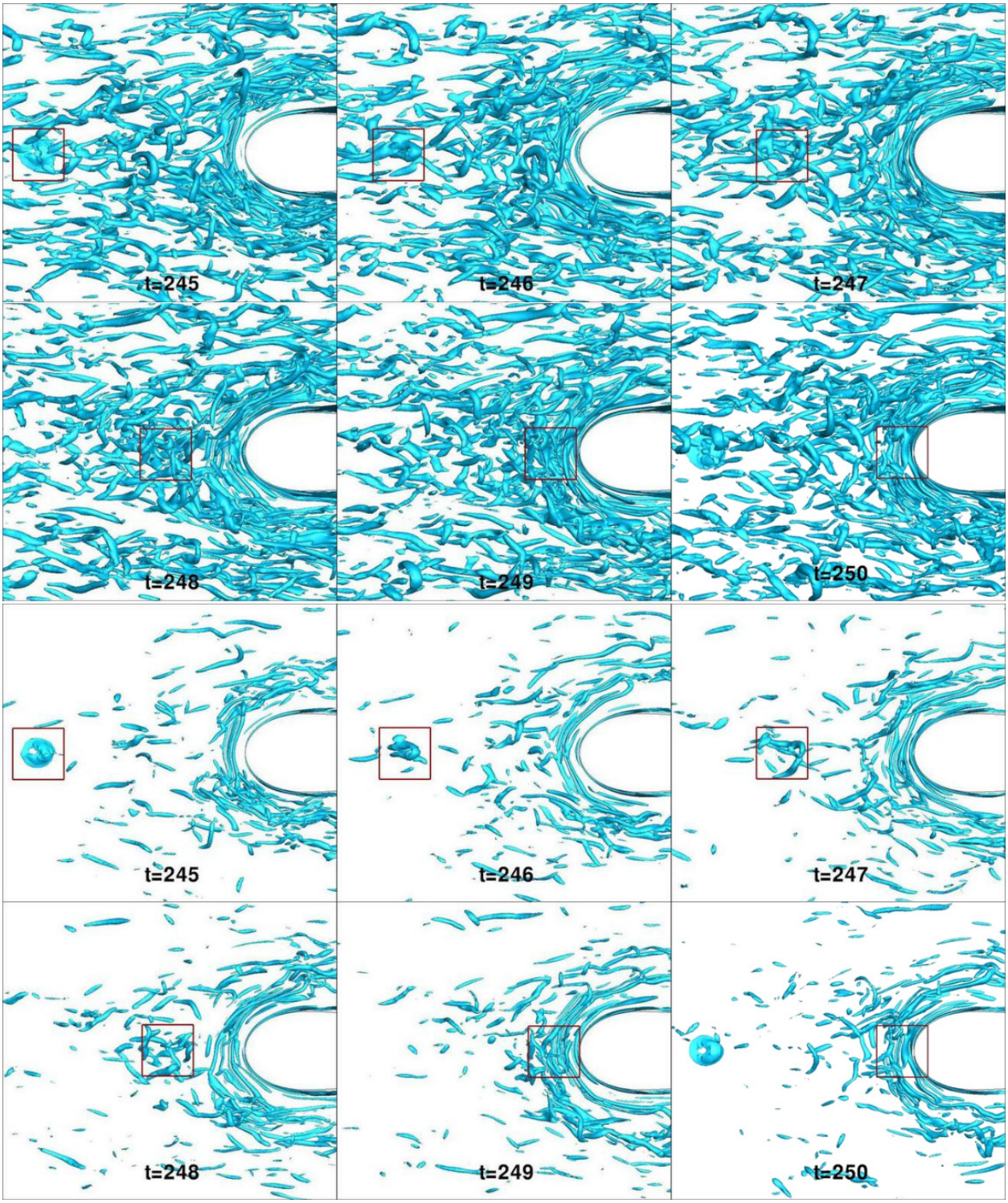


Figure 33: Case a: Iso-surfaces of Q=2 (top two rows) and Q=8 (bottom two rows). BL event is highlighted by red box.

DISTRIBUTION STATEMENT A. Approved for public release. Distribution is unlimited.

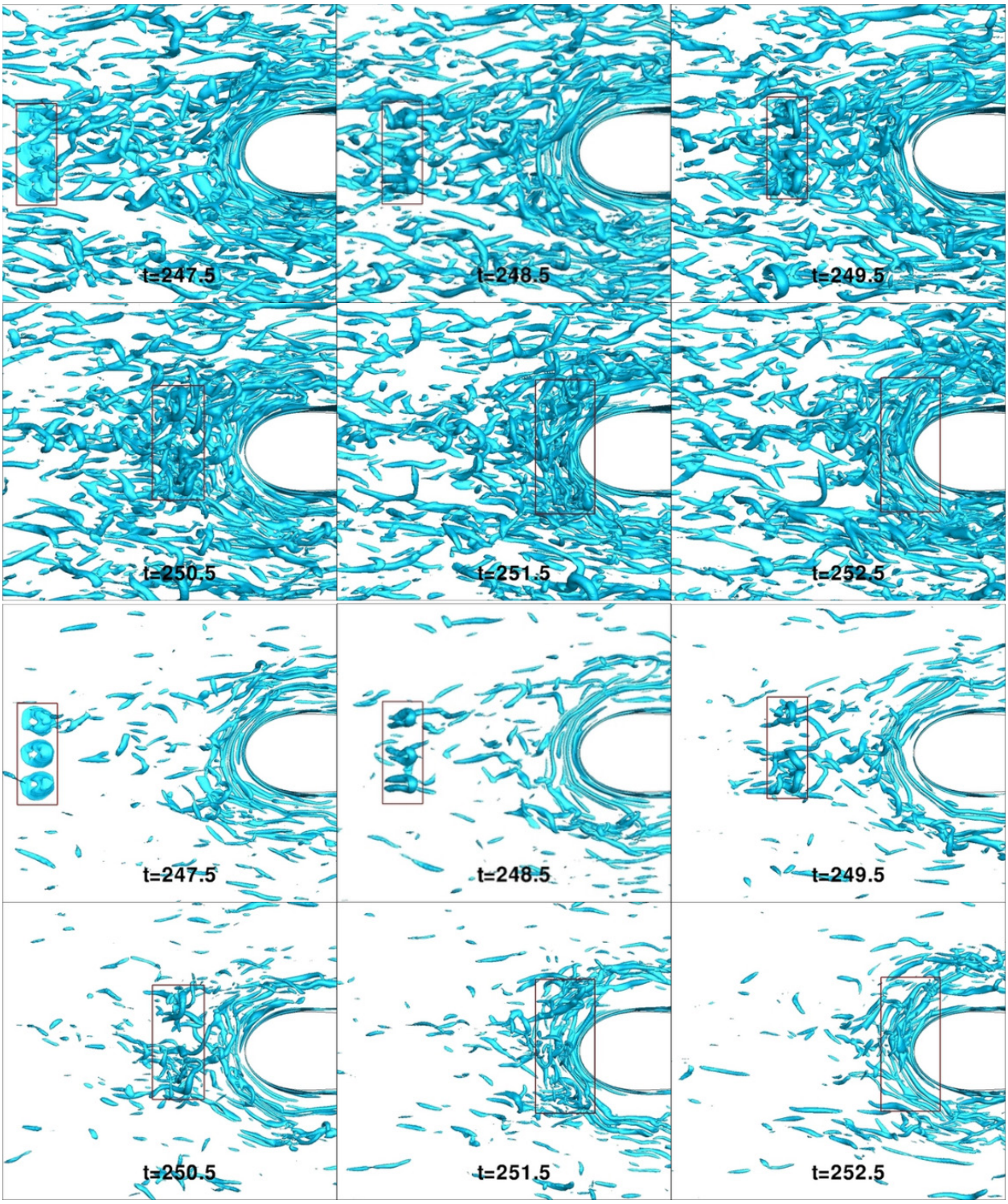


Figure 34: Case f: Iso-surfaces of Q=2 (top two rows) and Q=8 (bottom two rows). BL event is highlighted by red box.

DISTRIBUTION STATEMENT A. Approved for public release. Distribution is unlimited.

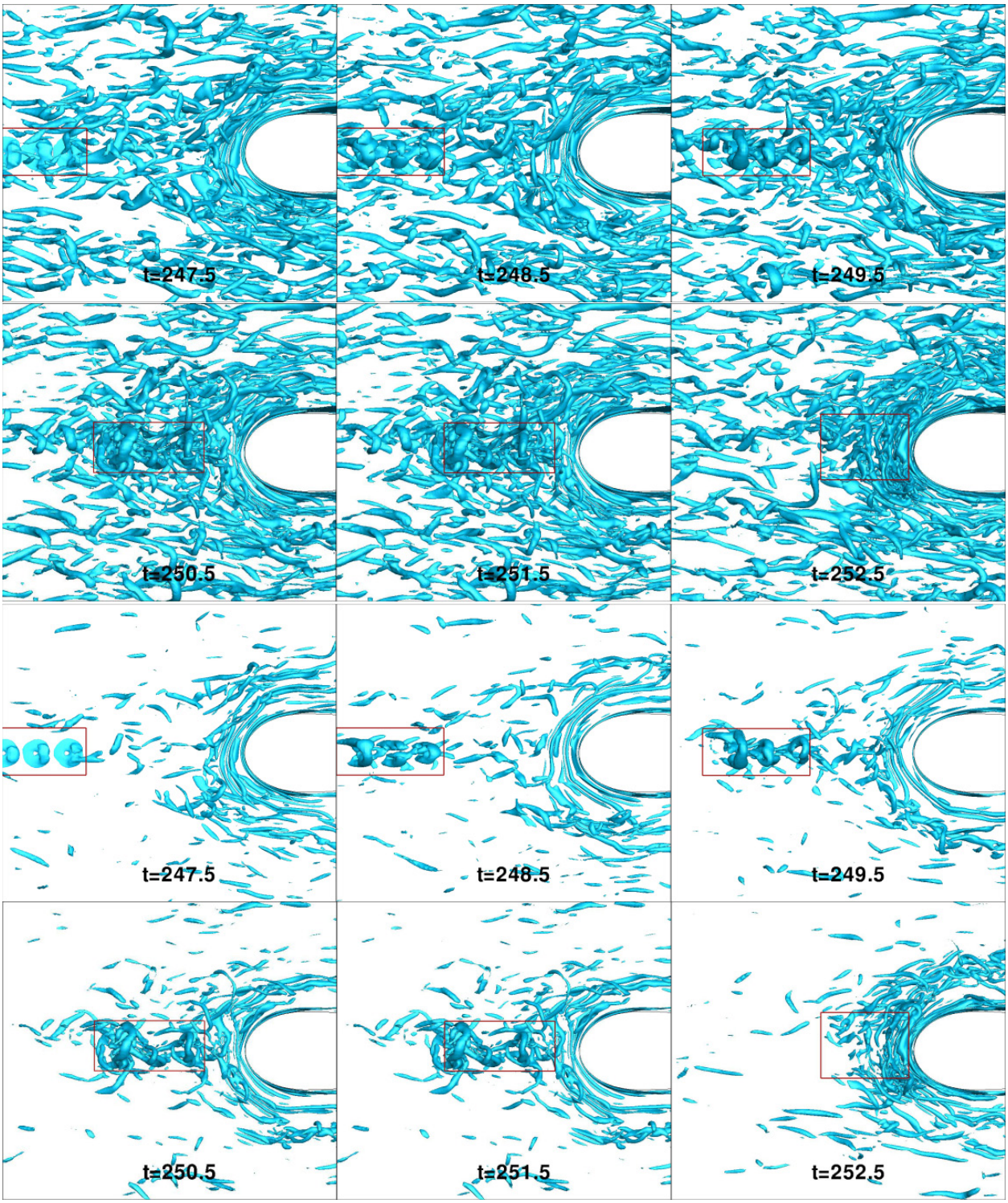


Figure 35: Case g: Iso-surfaces of Q=2 (top two rows) and Q=8 (bottom two rows). BL event is highlighted by red box.

DISTRIBUTION STATEMENT A. Approved for public release. Distribution is unlimited.

In the literature, the frequency associated with the bimodal behavior is often normalized with the boundary layer thickness, δ, and the freestream velocity, v_{in}. For the present simulation, the BL thickness in the symmetry plane one chord length upstream of the leading edge is $\delta = 0.83$. The dimensionless frequencies based on the BL thickness are f=0.10 (based on VITA for box 1), 0.10 (box 3), 0.11 (based on circulation), 0.10 (based on cross-correlation for box 1), and 0.10 (based on cross-correlation for box 3). These frequencies are close to those reported by Gross and Robison [25] and Gand et al. [21]. The spectra suggest that the circulation is more strongly correlated with the VITA value for box 1 (which is farther upstream of the interaction) than the VITA value for box 3.

Figure 37 provides the results for case a (x=2.65, T=5, B=2). The VITA value has a period of roughly 10, suggesting that every other forcing cycle leads to a BL event. Some of the resulting BL events are stronger (e.g., higher VITA values for t=270 and 285) and some are weaker (e.g., lower VITA value for t=260). Visual inspection reveals no close resemblance between the circulation and the VITA value. Based on the spread and periodicity of the cross-correlation it must be concluded that the BL events and the behavior of the HV are not well correlated for box 1. The spread and periodicity for box 3 are slightly better. Results for case b (x=2.65, T=7.5, B=2) are provided in Figure 38. For this case, the VITA values appear to follow the forcing signal better but the cross-correlations remain weak although the cross-correlation for box 1 has a period of 7.5. For case c, the blowing ratio was increased to B=4 and the period remained unchanged at T=7. The VITA value for box 1 has the same period as the actuation (Figure 39). Compared to the previous case with B = 2, the cross-correlation for box 1 displays a similar periodicity. However, the amplitudes are higher and the peaks are more defined. When the jet is moved upstream to x=3.5, the VITA value is not showing a clear dependence on the forcing (case d, T=7.5, B=2, Figure 40). This was expected since compared to case b the turbulent boundary layer has more time to recover its equilibrium. The disturbances travel a longer distance before they reach the junction and as a result, the BL events are weaker and have less effect on the junction flow than for case b. For case e, the forcing period was increased to T=10 (and x=2.65, B=2). This period is visible in the VITA time history for box 1 (Figure 41). The cross-correlation for box 1 has a period of roughly 11 which suggests a weak correlation between the BL events and the HV response (Figure 41). The cross-correlation for box 3 has a period of roughly five. Results for case f (three transverse jets, x=2.65, T=7.5, B=2) are shown in Figure 42. Compared to case b, the VITA values for boxes 1 & 2 have a stronger dependence on the forcing signal and several of the VITA peaks are followed by maxima of the circulation. This case has the strongest periodicity and largest spread of the cross-correlation for box 1, which indicates that the HV behavior is more strongly correlated with the actuation than for the other cases.

Finally, results for case g (three streamwise jets, x_{av}=2.65, T=7.5, B=2) are provided in Figure 43. For this case, box 1 was not considered because it overlapped with one of the holes. Instead, box 2 was considered. Both the results from boxes 2 and 3 reveal a strong periodic behavior with box 3 showing a slightly better correlation than box 2. Box 3 for case g has the highest correlation of the cases analyzed however the box 1 correlation for case f displays the largest oscillations in the time shift.

DISTRIBUTION STATEMENT A. Approved for public release. Distribution is unlimited.

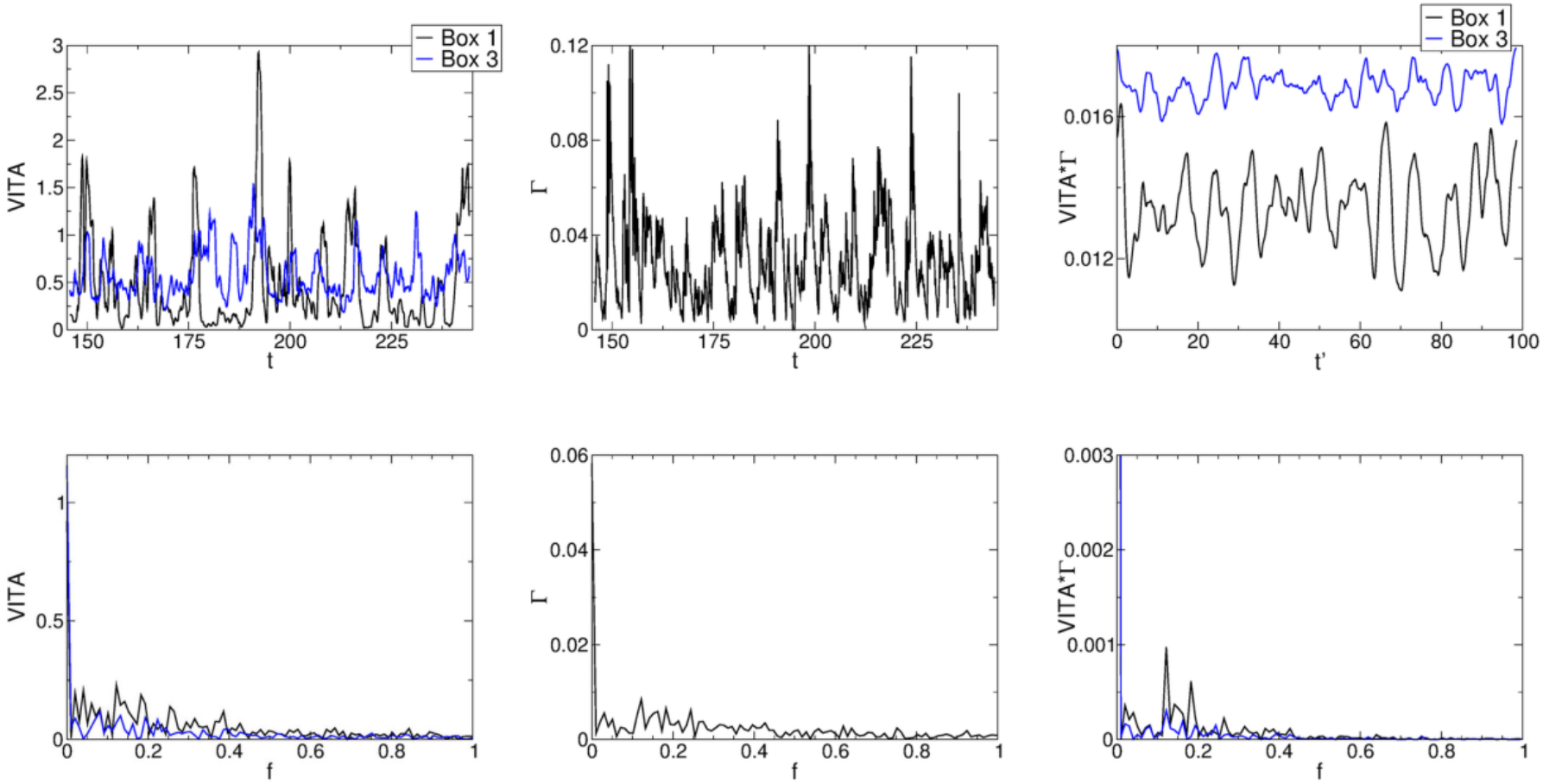


Figure 36: Uncontrolled flow: VITA (left), circulation (middle), and cross-correlation of VITA and circulation (right). Signals (top) and spectra (bottom).

DISTRIBUTION STATEMENT A. Approved for public release. Distribution is unlimited.

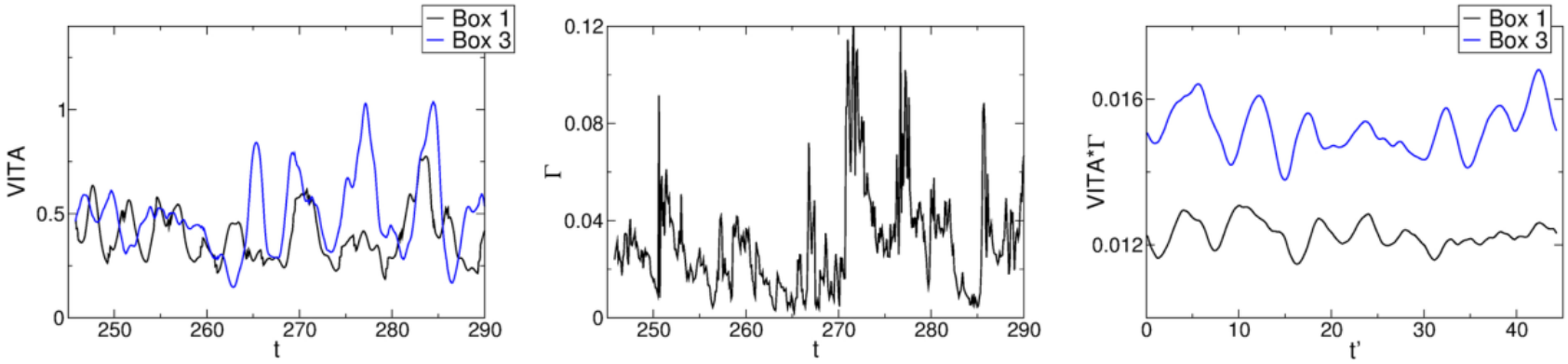


Figure 37: Case a: VITA (left), circulation (middle), and cross-correlation of VITA and circulation (right).

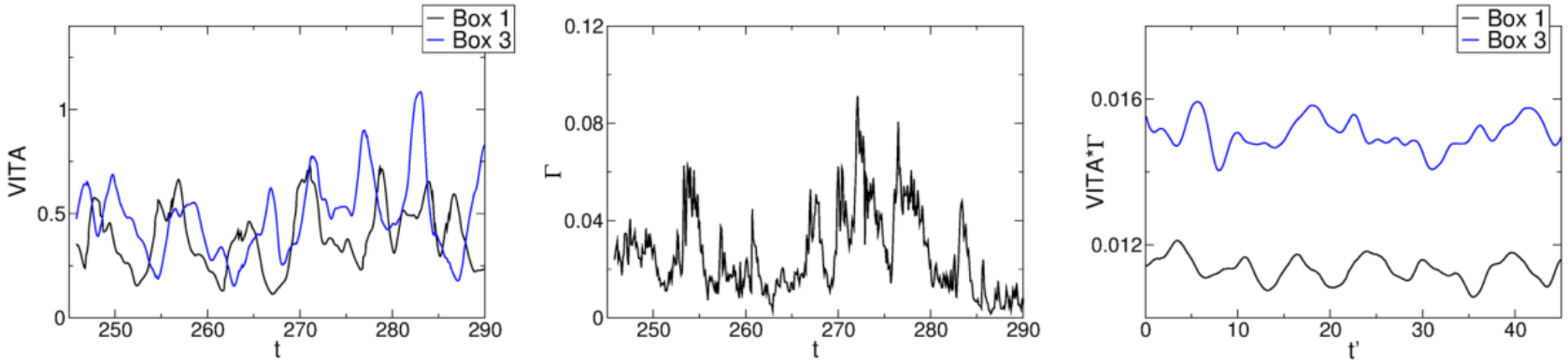


Figure 38: Case b: VITA (left), circulation (middle), and cross-correlation of VITA and circulation (right).

DISTRIBUTION STATEMENT A. Approved for public release. Distribution is unlimited.

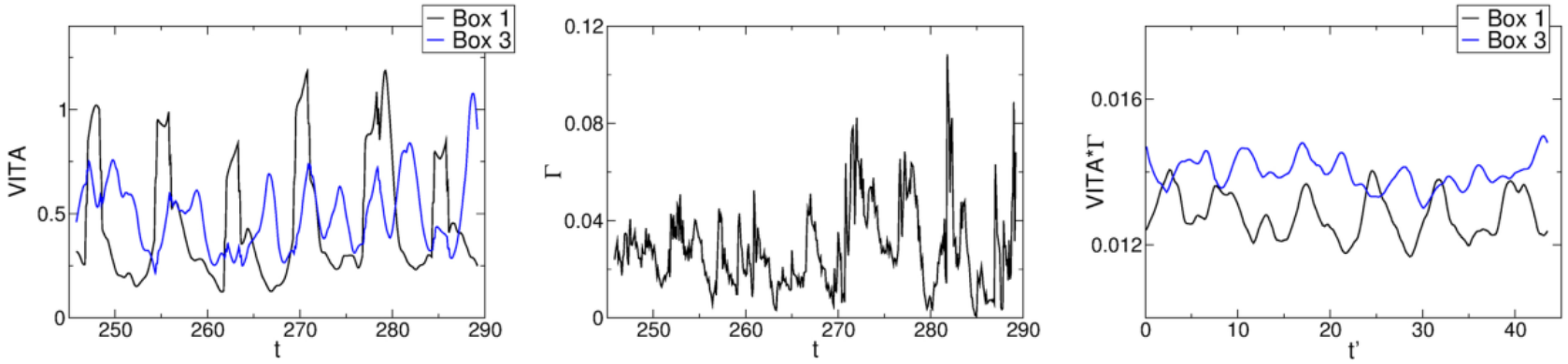


Figure 39: Case c: VITA (left), circulation (middle), and cross-correlation of VITA and circulation (right).

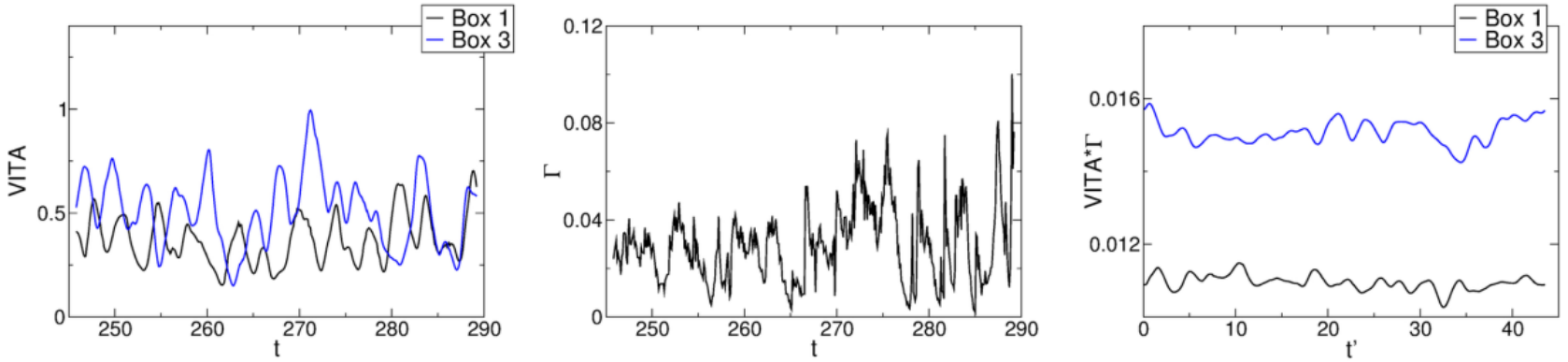


Figure 40: Case d: VITA (left), circulation (middle), and cross-correlation of VITA and circulation (right).

DISTRIBUTION STATEMENT A. Approved for public release. Distribution is unlimited.

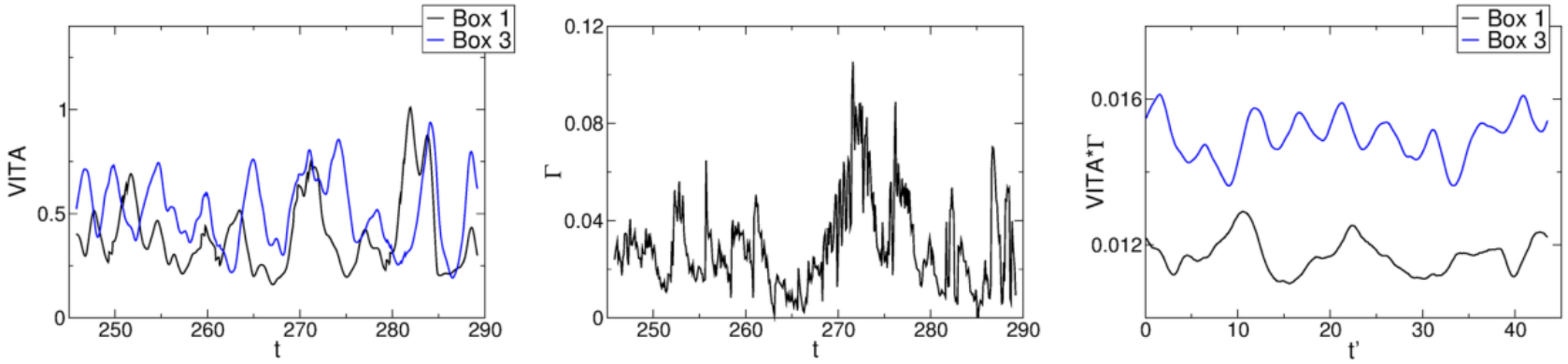


Figure 41: Case e: VITA (left), circulation (middle), and cross-correlation of VITA and circulation (right).

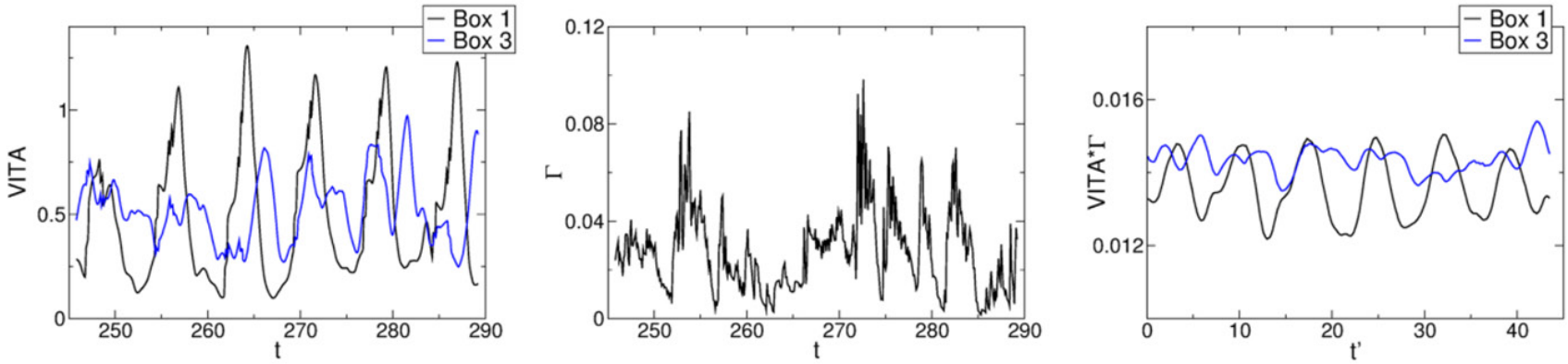


Figure 42: Case f: VITA (left), circulation (middle), and cross-correlation of VITA and circulation (right).

DISTRIBUTION STATEMENT A. Approved for public release. Distribution is unlimited.

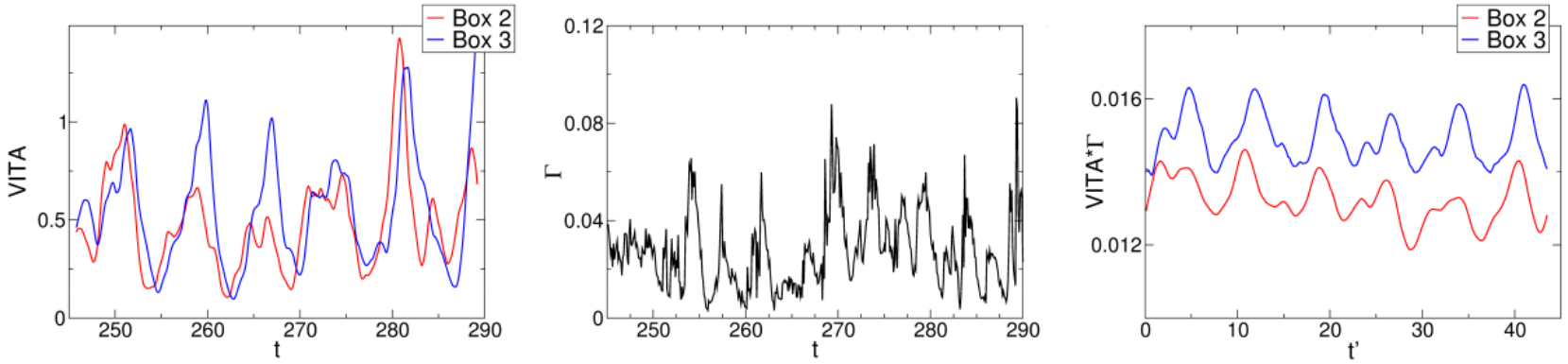


Figure 43: Case g: VITA (left), circulation (middle), and cross-correlation of VITA and circulation (right).

DISTRIBUTION STATEMENT A. Approved for public release. Distribution is unlimited.

5.2 Proper Orthogonal Decomposition

The uncontrolled flow as a well as cases b and f were analyzed with the POD to investigate the dynamics of the coherent structures introduced by the forcing as well as the HV response. Two different areas were considered: The first area (red outline in Figure 44) is downstream of the forcing location and upstream of the junction and was chosen for investigating the upstream turbulent boundary layer. The second area (blue outline in Figure 44) was designed to capture the junction flow dynamics.

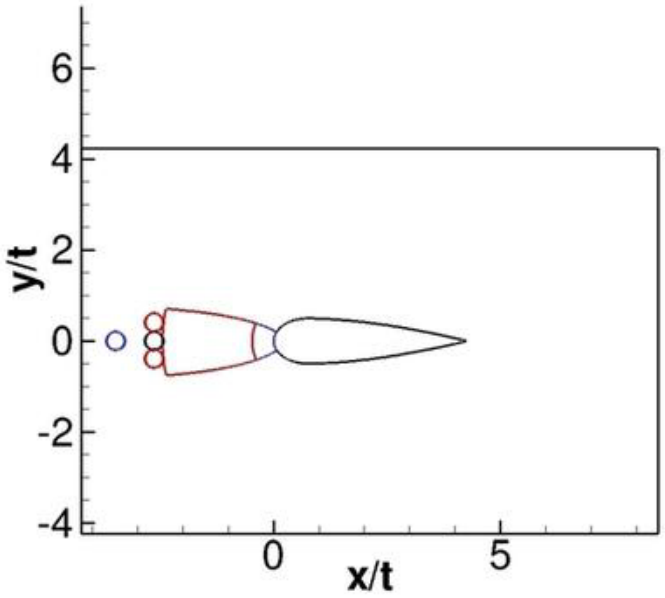


Figure 44: Areas analyzed with POD and jet locations

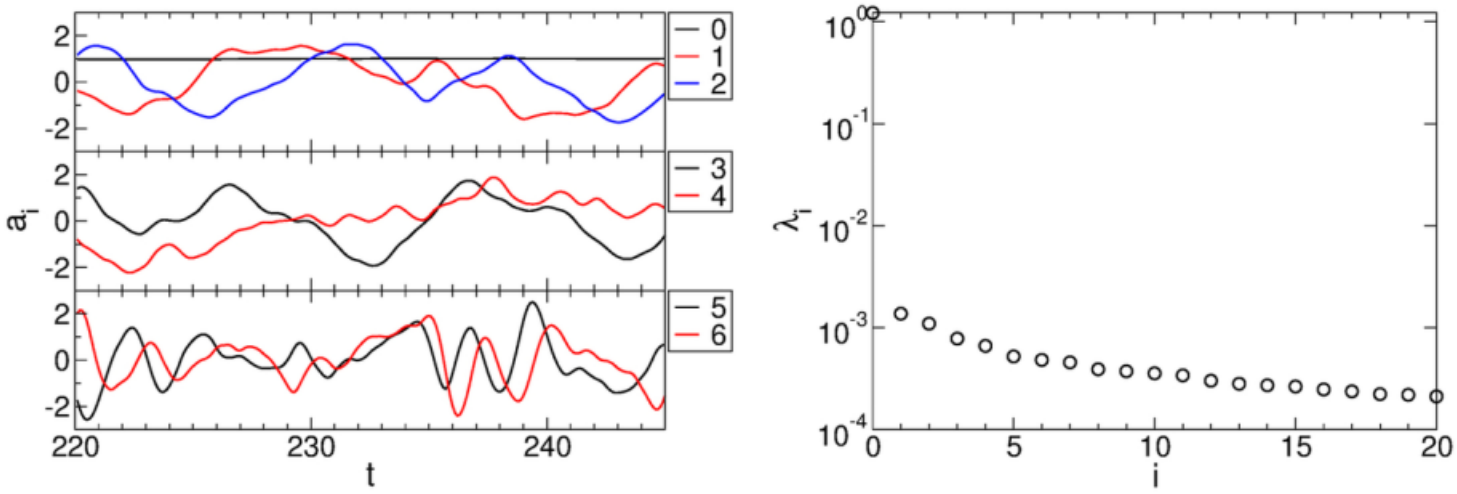
Time-coefficients, eigenvalues and POD modes for the uncontrolled flow are shown in Figures 45 and 46. Modes 1 - 3 for the upstream boundary layer capture elongated low-frequency structures that are likely related to low-speed streaks in the turbulent boundary layer. According to Adrian et al. [14], such structures are related to quasi-periodic eruptions of near-wall fluid. Concerning the junction region, modes 1 and 2 have similar eigenvalue magnitudes and thus likely form a pair. The period is about 10 and the associated frequency made dimensionless with the boundary layer thickness is $f = 0.83/10 = 0.08$ which suggests that modes 1 and 2 are related to the bimodal behavior.

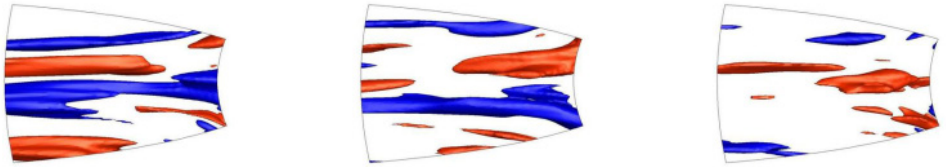
Time-coefficients, eigenvalues, and associated POD modes for case b are provided in Figure 47 and 48. For the upstream area (red box in Figure 44), the mode 2 and 3 time-coefficients have a period of roughly 7.5 but the associated eigenvalues have different magnitudes and the mode shapes are not directly related to each other. Modes 1 and 2 appear to originate from the jet location which is an indication that they may be related to the forcing. Based on the mode shapes, it can be conjectured that the forcing introduces streamwise streaks. The time-coefficients for the leading edge region (blue box in Figure 44) exhibit a more or less random signal that is not directly tied to the forcing. In agreement with the weak correlation (Figure 38), this suggests a weak response of the junction flow to the forcing.

DISTRIBUTION STATEMENT A. Approved for public release. Distribution is unlimited.

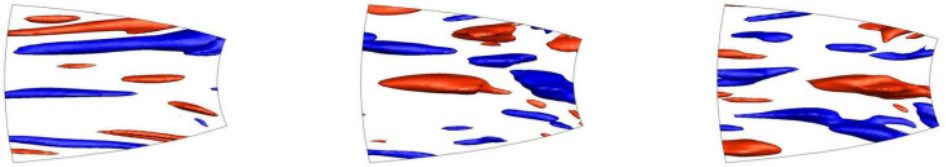
The results from the POD analysis for case f are presented in Figure 49 and 50. Modes 3 and 4 (for the upstream area) have a period of about 7.5. The associated eigenvalues have roughly the same magnitude and the time-coefficients appear correlated. The mode shape for mode 3 suggests that all three jets generate streamwise streaks which agrees with the earlier observation of three hairpins downstream of the jet location (Figure 34). Modes 1 and 2 have a larger period of roughly 10 and likely capture naturally occurring boundary layer structures. Regarding the junction region (blue box in Figure 44), none of the time-coefficients have a period close to the period of the actuation (T =7.5). One may speculate that either the junction flow does not respond to the forcing or that the computed time-sequence is too short to allow for definitive conclusions to be drawn.

DISTRIBUTION STATEMENT A. Approved for public release. Distribution is unlimited.





mode 1 mode 2 mode 3



mode 4 mode 5 mode 6

Figure 45: Uncontrolled flow: POD time-coefficients, eigenvalues, and modes 1-6 (iso-surfaces of $w = \pm 0.01$) for red area in Figure 44.

DISTRIBUTION STATEMENT A. Approved for public release. Distribution is unlimited.

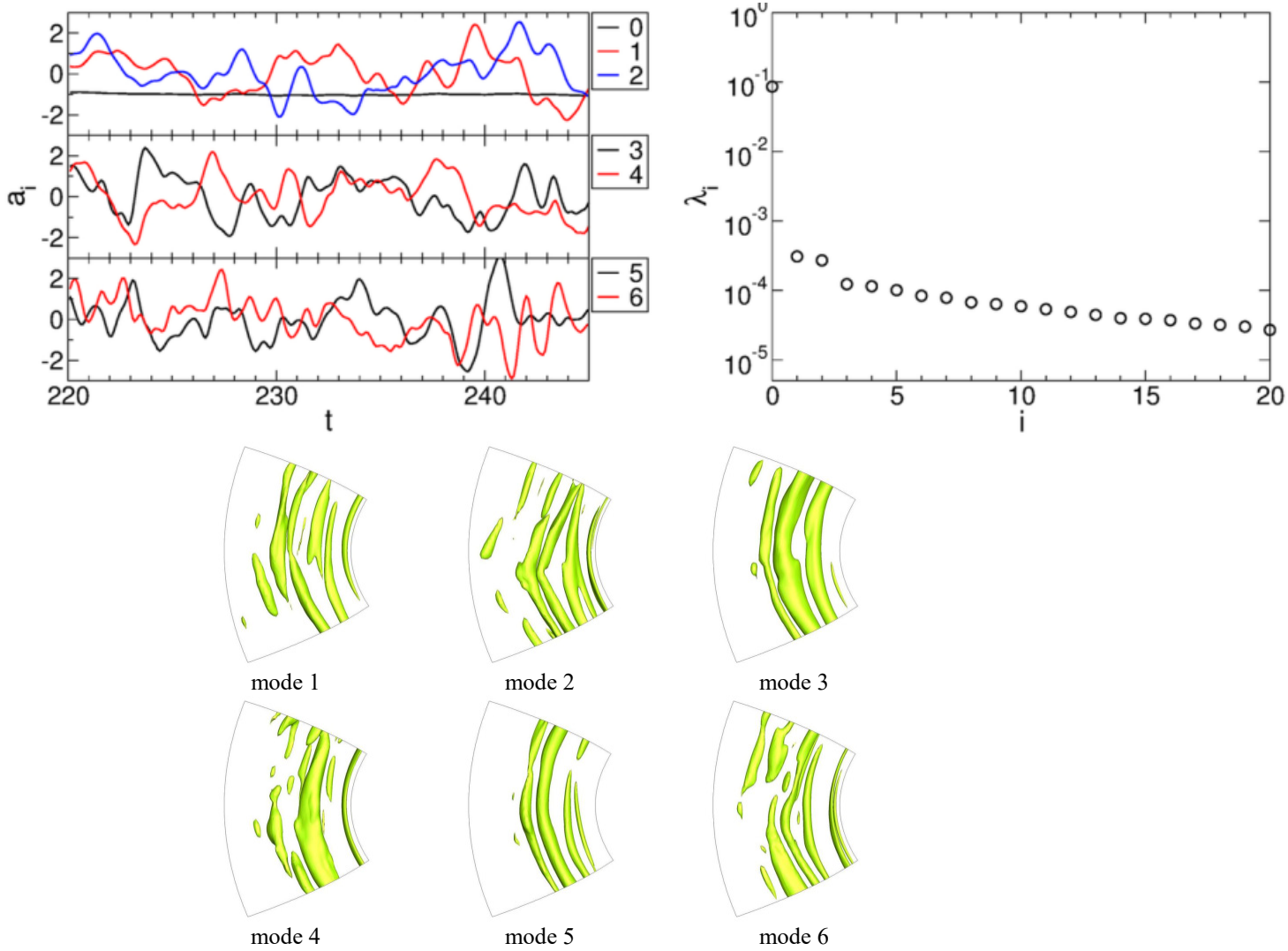
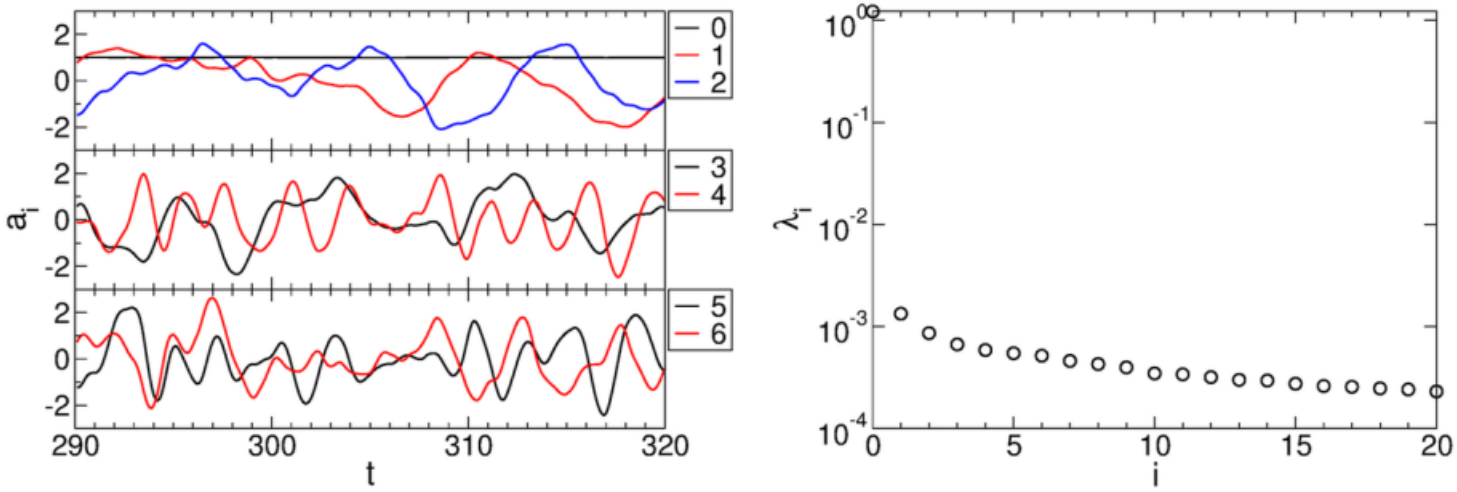
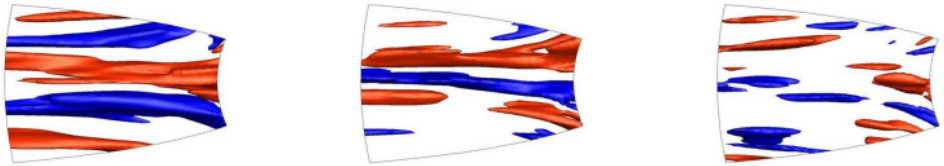


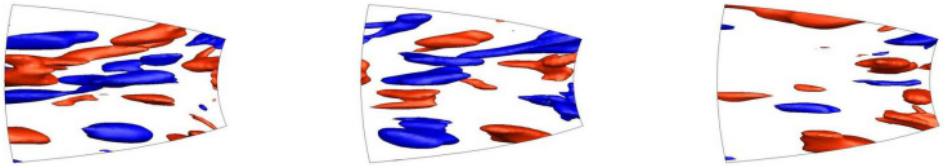
Figure 46: Uncontrolled flow: POD time-coefficients, eigenvalues, and modes 1-6 (iso-surfaces of Q=1) for blue area in Figure 44.

DISTRIBUTION STATEMENT A. Approved for public release. Distribution is unlimited.





mode 1 mode 2 mode 3



mode 4 mode 5 mode 6

Figure 47: Case b: POD time-coefficients, eigenvalues, and modes 1-6 (iso-surfaces of $w = \pm 0.01$) for red area in Figure 44.

DISTRIBUTION STATEMENT A. Approved for public release. Distribution is unlimited.

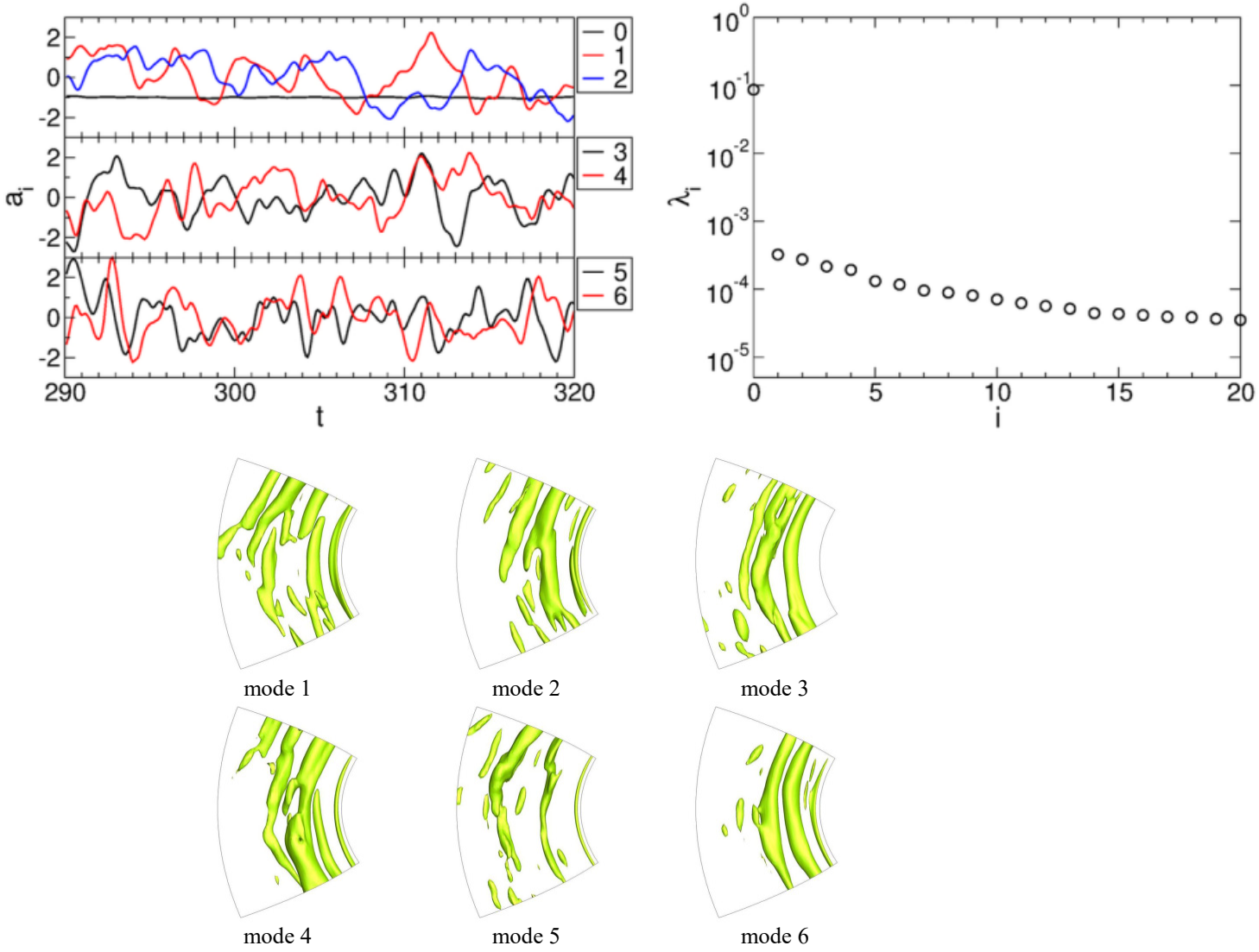
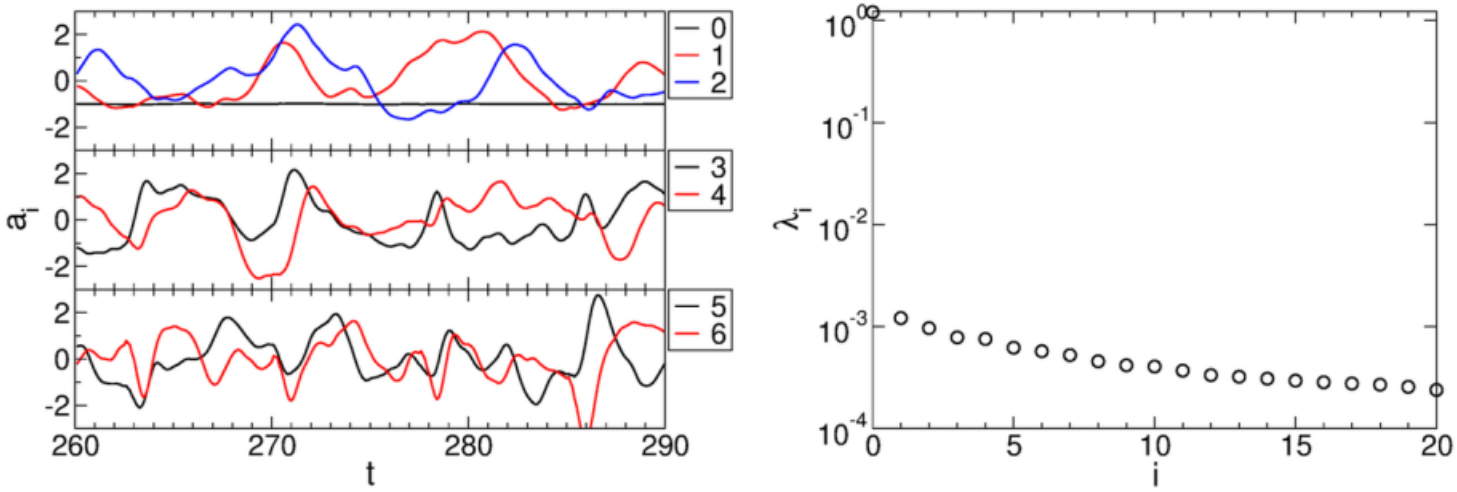
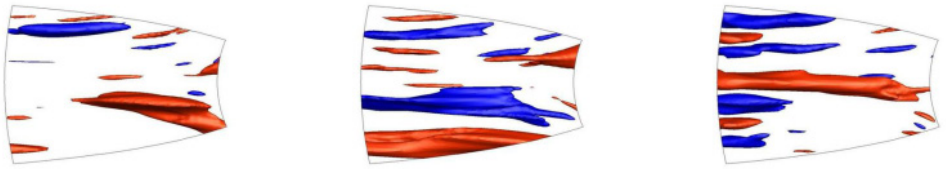


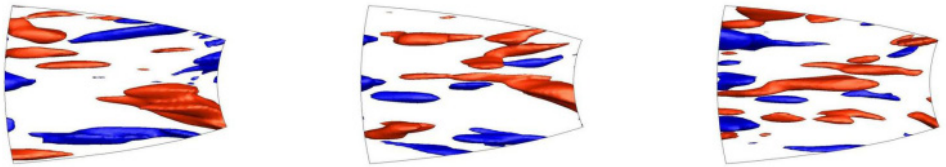
Figure 48: Case b: POD time-coefficients, eigenvalues, and modes 1-6 (iso-surfaces of Q=1) for blue area in Figure 44.

DISTRIBUTION STATEMENT A. Approved for public release. Distribution is unlimited.





mode 1 mode 2 mode 3



mode 4 mode 5 mode 6

Figure 49: Case f: POD time-coefficients, eigenvalues, and modes 1-6 (iso-surfaces of $w = \pm 0.01$) for red area in Figure 44.

DISTRIBUTION STATEMENT A. Approved for public release. Distribution is unlimited.

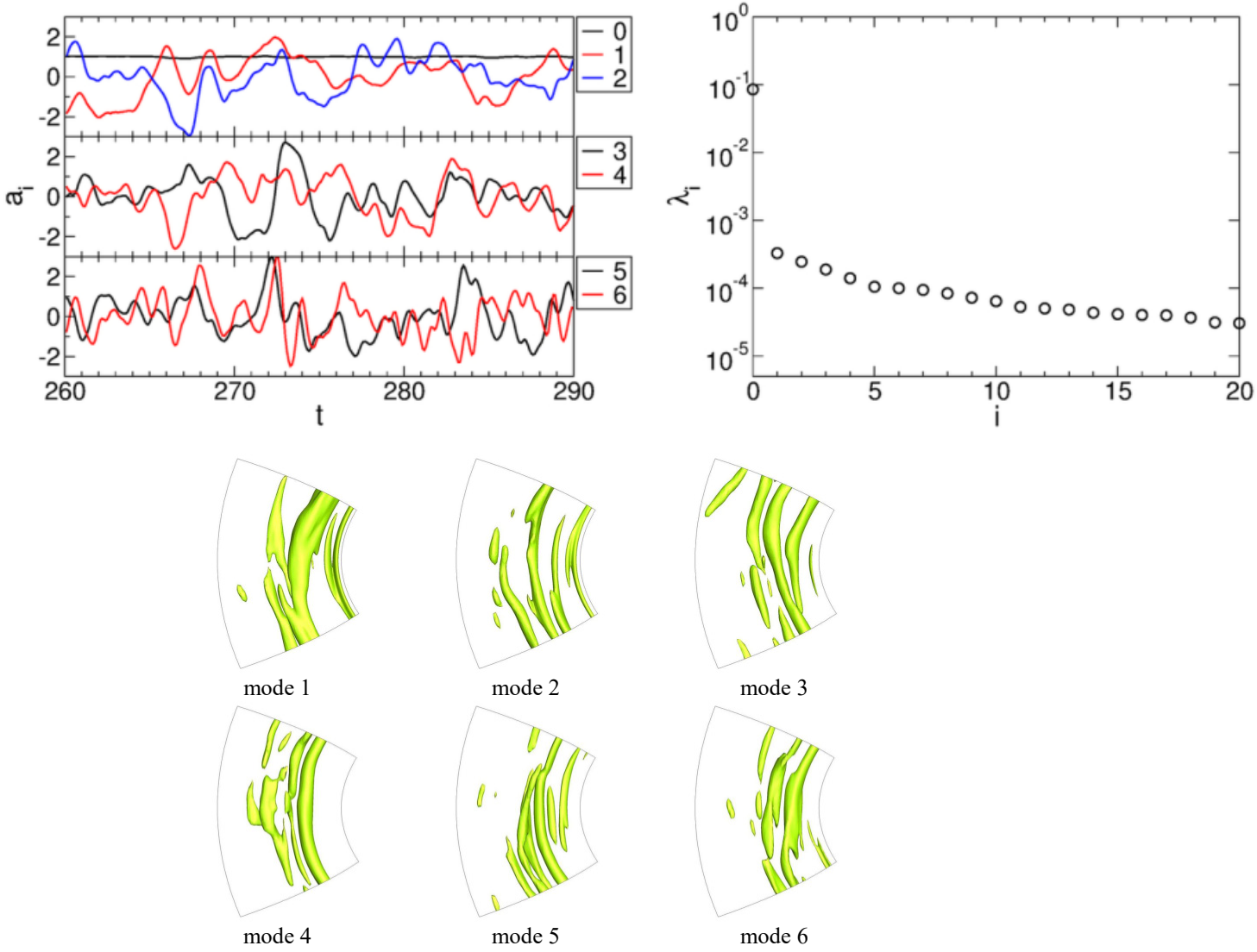


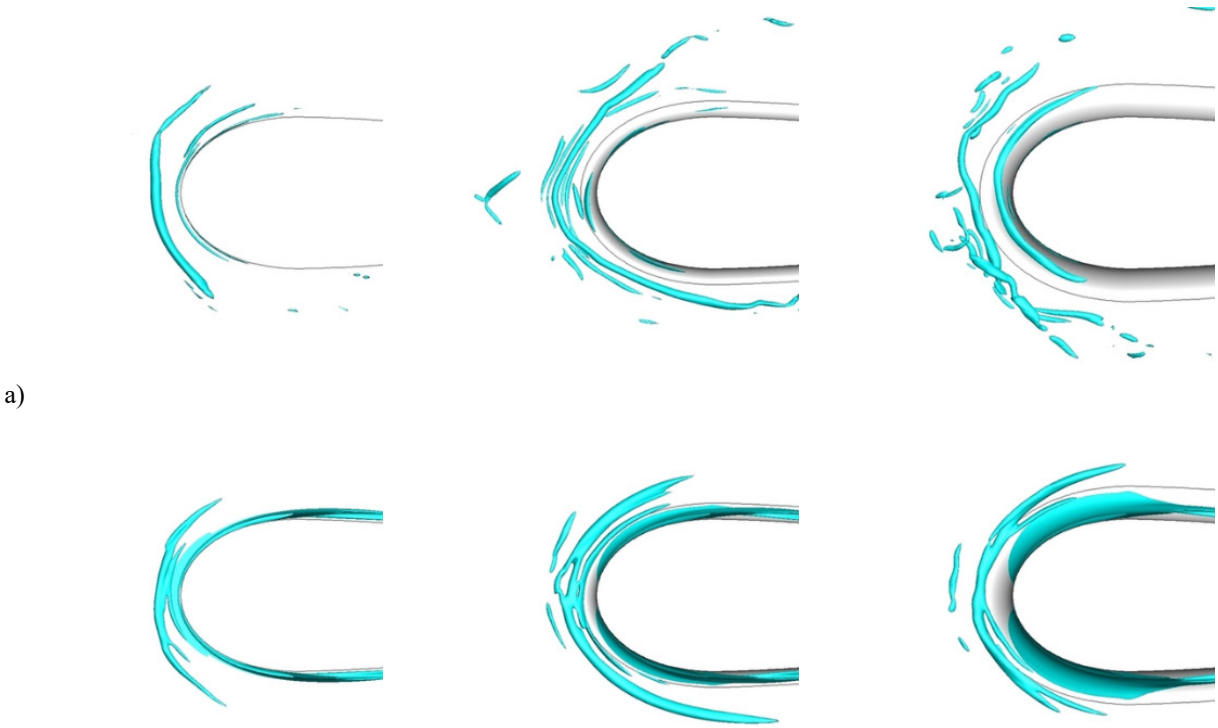
Figure 50: Case f: POD time-coefficients, eigenvalues, and modes 1-6 (iso-surfaces of Q=1) for blue area in Figure 44.

DISTRIBUTION STATEMENT A. Approved for public release. Distribution is unlimited.

6 PASSIVE FLOW CONTROL

6.1 Effect of Fillet on Mean Flow

As shown by Devenport et al. [28] fillets can have an effect on the bimodal behavior. To investigate if this is also the case for the chosen Rood wing configuration, simulations with a 0.1t (case F1) and 0.2t radius (case F2) circular fillet were carried out for a Reynolds number based on maximum thickness of 7,000. The approach flow BL thickness and setup of the simulations with fillet were the same as for the simulation without fillet (case NF). By comparing the results from the simulation without fillet (case NF) with the simulations with fillet (cases F1 and F2), the effect of the fillet on the mean flow and the bimodal behavior can be determined. Iso-surfaces of the Q-criterion computed from the instantaneous and time-averaged flow fields are provided in Figure 51. The time-averages were computed over time intervals of 245 (NF), 44.4 (F1), and 50 (F2). The time-averages indicate that the HV becomes stronger and moves further away from the leading edge as the fillet radius is increased. A stronger HV in the mean implies that the instantaneous HV is stronger and/or that the HV is moving less. The instantaneous flow visualizations hint at similarly intense HVs which suggests that the HV is moving less for the cases with fillet.



a)

b)

Figure 50: Iso-surfaces of Q=100 for cases NF (left), F1 (center) and F2 (right) obtained from a) instantaneous flow fields and b) time-averages.

DISTRIBUTION STATEMENT A. Approved for public release. Distribution is unlimited.

Iso-contours of the time-averaged streamwise velocity in the symmetry plane in Figure 52 show a recirculation region near the bottom wall. As the fillet radius is increased, the reverse flow intensifies and the recirculation region becomes thicker and more stretched out in the upstream and downstream direction. Iso-contours of the streamfunction in Figure 53 clearly outline the separated region. The core of the time-averaged HV is situated at $(x, z) = (0.12, 0.042)$ for case NF, $(0.15, 0.042)$ for case F1, and $(0.21, 0.049)$ for case F2. This suggests that the HV core moves upstream and away from the wall as the fillet radius is increased. Also, the streamlines surrounding the HV core become rounder which implies that the HV is moving less. For the un-filleted Rood wing, a smaller secondary vortex with opposite sense of rotation is located at $(x, z) = (0.014, 0.019)$. The secondary vortex is missing for cases F1 and F2.

Top-down views of the endwall flooded by the magnitude of the skin-friction coefficient in Figure 54 suggest that the HV gets weaker and/or moves farther away from the endwall as the fillet radius is increased. The skin-friction lines display a saddle point upstream of the leading edge which constitutes the most upstream extent of the endwall BL separation associated with the HV vortex.

For case NF, the stagnation point is located at x=0.6. For case F1 and F2 the time-averages are of lower quality and the stagnation points are roughly located at x=0.8 and x=0.7 which is consistent with the earlier observation that the HV moves upstream as the fillet radius is increased. Figure 55 shows the wall pressure coefficient in the symmetry plane for all three cases. For all cases, the pressure coefficient increases to a value near one at the leading edge which is the expected stagnation point value. Slight dips in the c_p-curves appear to be related to the time-mean core locations of the HV. Iso-contours of the wall pressure coefficient in Figure 56 reveal a small increase of the low-pressure regions near the maximum thickness of the airfoil which suggests that the fillet reduces the corner separation.

DISTRIBUTION STATEMENT A. Approved for public release. Distribution is unlimited.

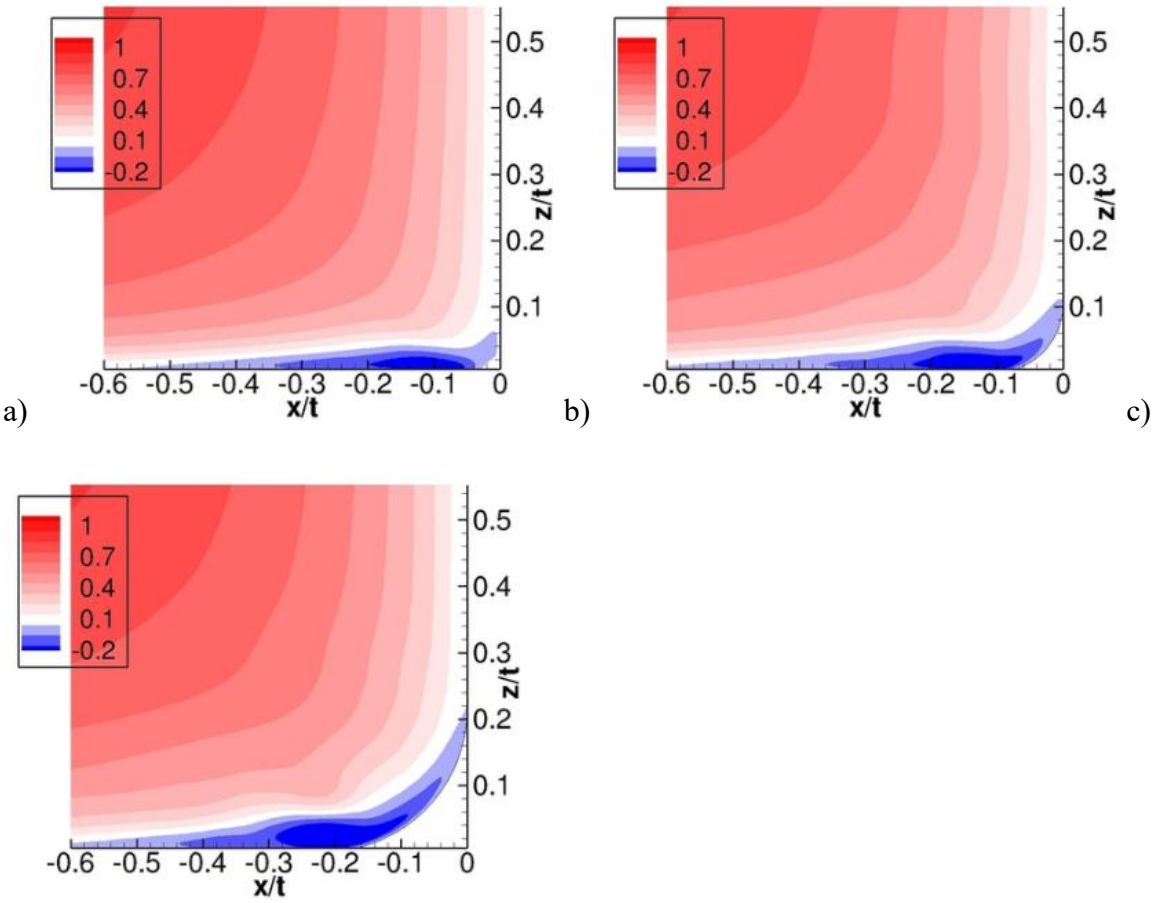


Figure 51: Iso-contours of streamwise velocity in symmetry plane for cases a) NF, b) F1, and c) F2.

DISTRIBUTION STATEMENT A. Approved for public release. Distribution is unlimited.

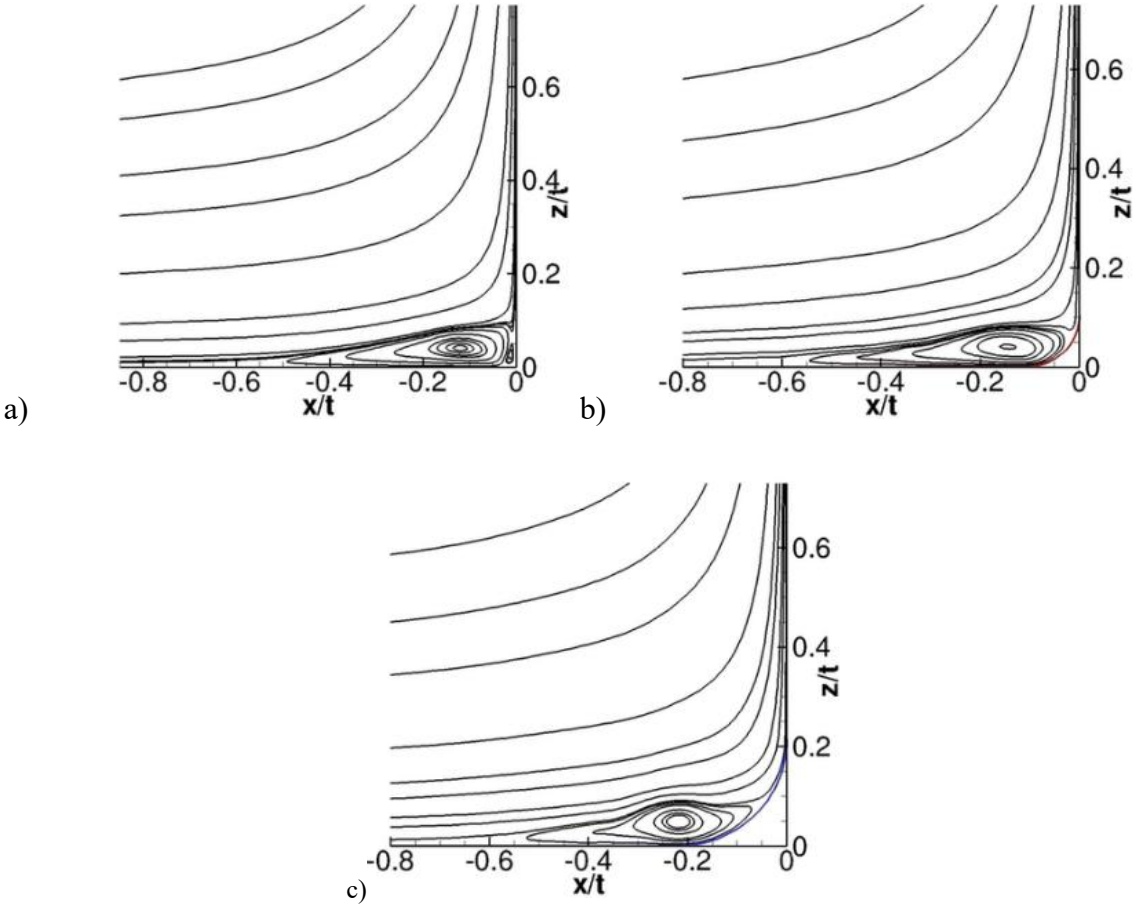


Figure 52: Streamlines in symmetry plane for cases a) NF, b) F1, and c) F2a)

DISTRIBUTION STATEMENT A. Approved for public release. Distribution is unlimited.

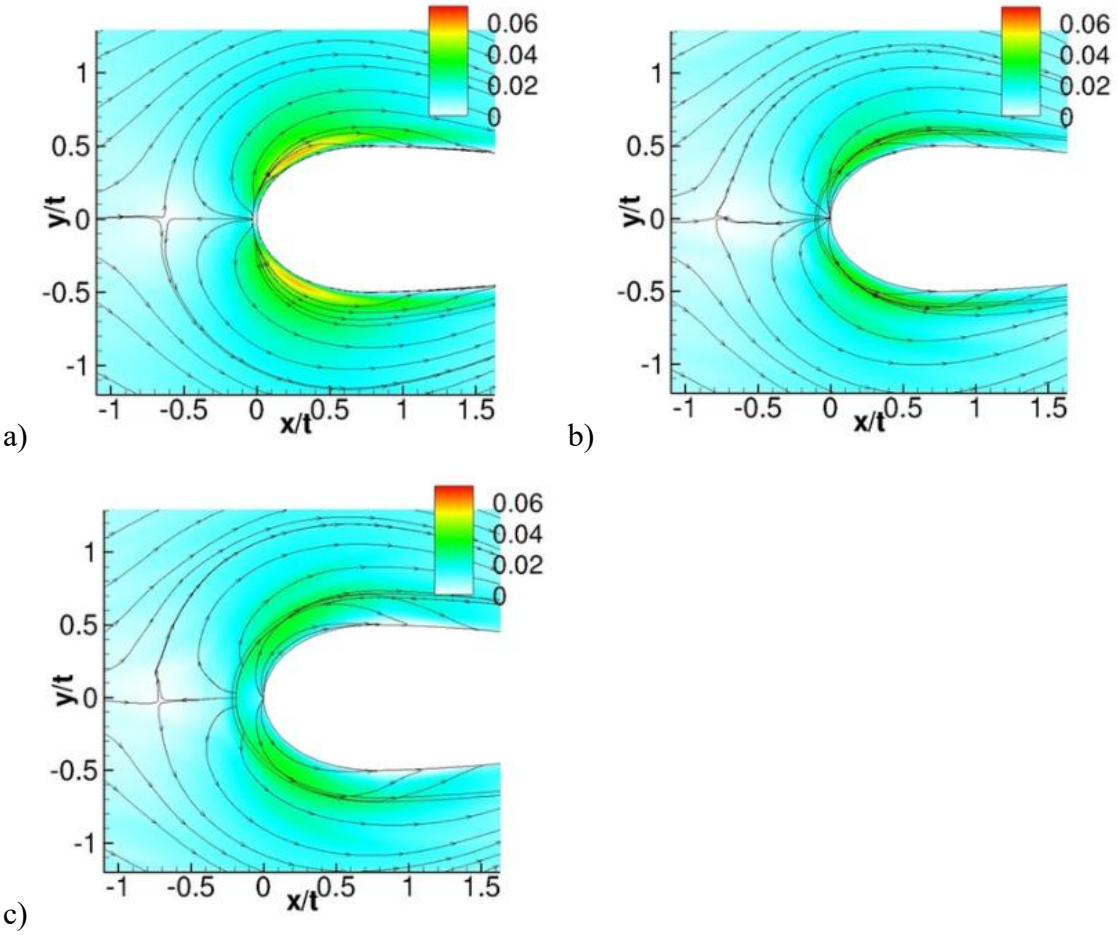


Figure 53: Iso-contours of skin-friction coefficient magnitude and skin-friction lines obtained from time-averages for cases a) NF, b) F1, and c) F2

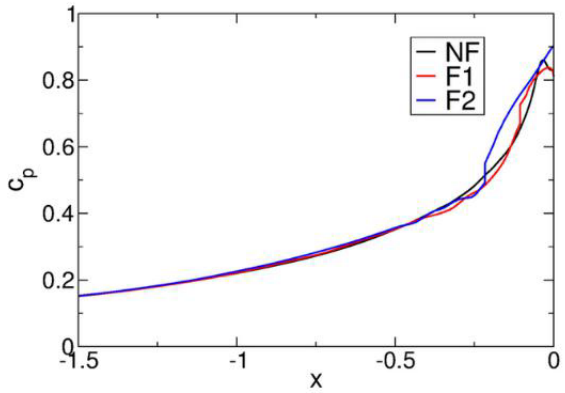


Figure 54: Wall pressure coefficient in symmetry plane.

DISTRIBUTION STATEMENT A. Approved for public release. Distribution is unlimited.

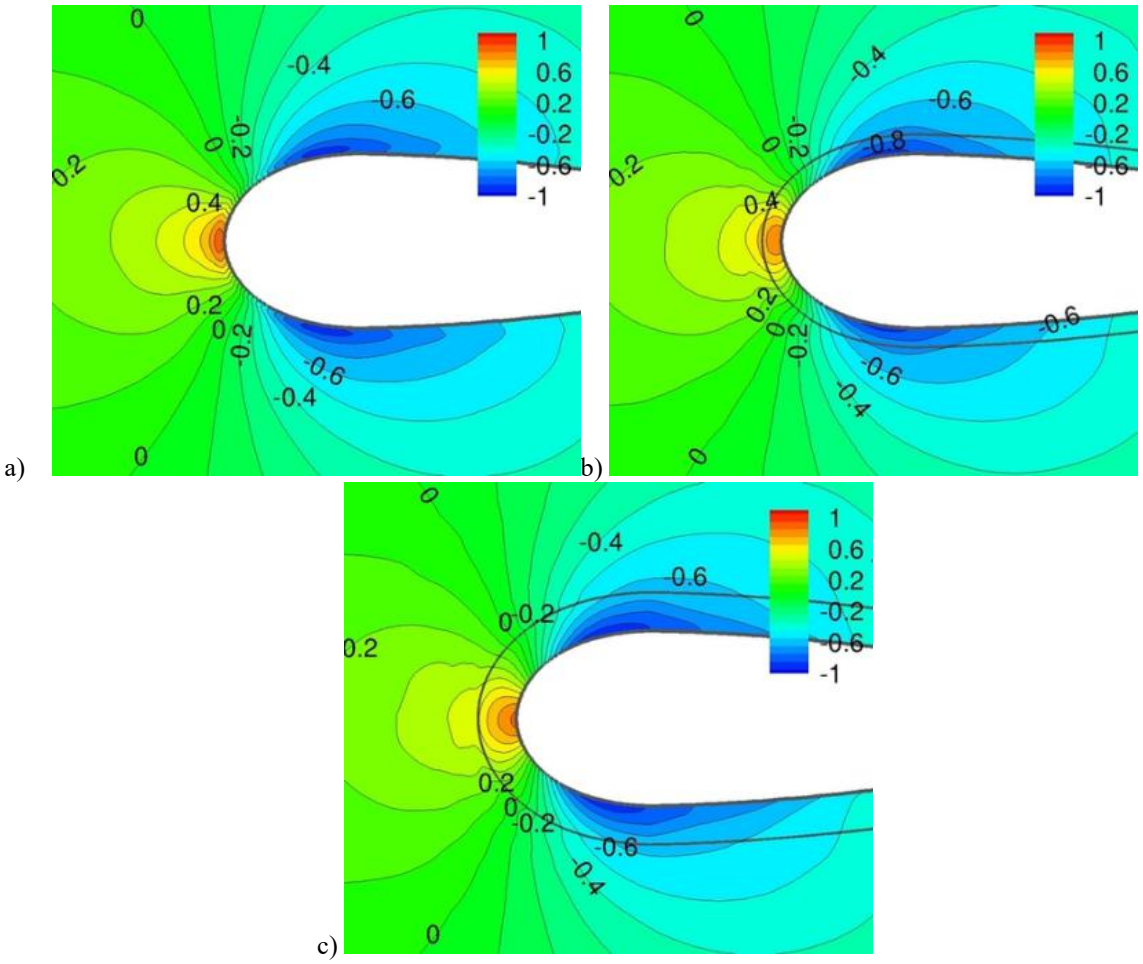


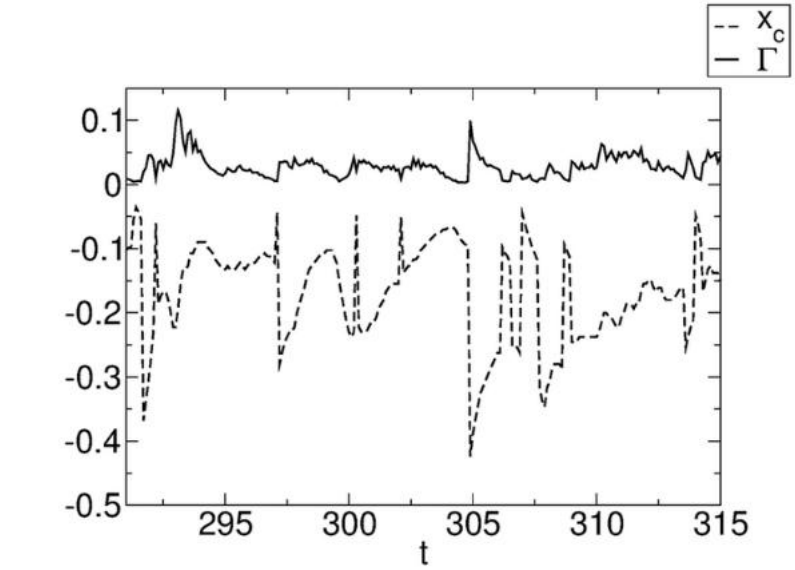
Figure 55: Iso-contours of wall pressure coefficient for cases a) NF, b) F1, and c) F2.

6.2 Effect of Fillet on Unsteady Flow

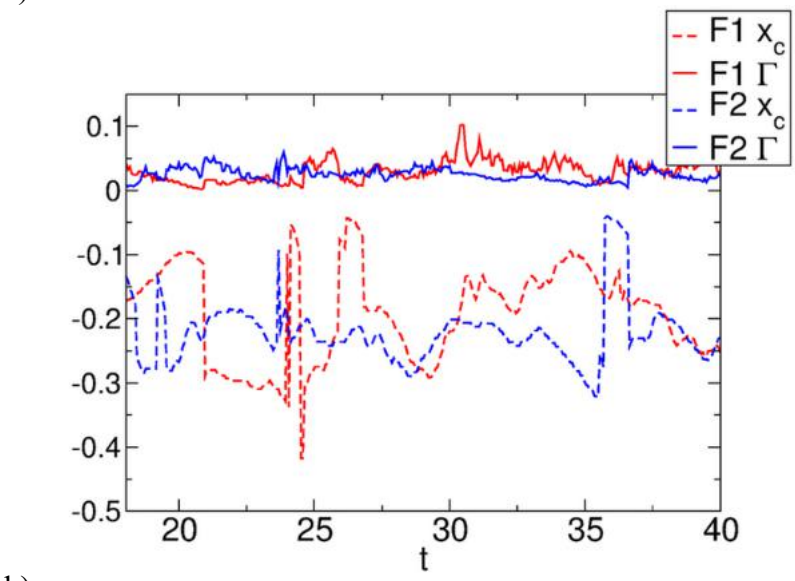
Using the same methods as before to quantitatively describe the behavior of the HV, the core location, x_c, and circulation, Γ, in the symmetry plane were extracted from the time-dependent flow data (Figure 57). Without fillet (case NF), the circulation fluctuates widely between 0 and a maximum value of 0.1. Sudden jumps of the vortex core location occur when the circulation is low. These jumps can be attributed to the vortex detection method which always picks the strongest vortex. For example, near t=305, a weakening vortex near the leading edge is replaced by a new stronger vortex far away from the leading edge. For fillet 1 (case F1) the circulation exhibits similar but less frequent fluctuations than for case NF. For fillet 2 (case F2) the unsteadiness is noticeably suppressed compared to the unfilleted airfoil. The mean HV core locations computed from the x_c-time-averages (Tab. 5) roughly agree with the core locations in Figure 53. The mean circulation is the largest for case F1, followed by cases NF and F2. As a measure for the overall flow unsteadiness, the standard deviations were computed as well. With increasing fillet radius, the standard deviations are noticeably lowered. Finally, the period of the circulation fluctuations was computed. Although the spectral resolution is poor, the present

DISTRIBUTION STATEMENT A. Approved for public release. Distribution is unlimited.

results indicate that the fillets reduce the HV unsteadiness and increase the associated frequencies.



a)



b)

Figure 56: Vortex core location and circulation for cases a) NF and b) F1 and F2.

Table 5: Mean and standard deviation of streamwise core location, x_c, and circulation, of horseshoe vortex as well as dominant period.

Case	*Mean*	*Std. dev.*	*Mean*	*Std. dev.*	*Mode switching period*
NF	0.1661	0.0757	0.0276	0.0177	9.5
F1	0.1926	0.0743	0.0301	0.0167	7.6
F2	0.2226	0.0484	0.0250	0.0099	5.7

DISTRIBUTION STATEMENT A. Approved for public release. Distribution is unlimited.

7 CONCLUSIONS

Turbulent junction flows exhibit a bimodal behavior that is characterized by the random switching between a zero-flow and a back-flow mode [3]. Although various different explanations for this behavior were offered, no consensus has been reached with regard to whether the mode switching is a consequence of upstream events in the turbulent approach boundary layer (BL) or the result of an inherent instability of the junction flow itself. Large-eddy simulations of a junction flow experiment at Penn State University (PSU) were carried out to obtain flow data with high resolution in space and time. The simulations were set up to match the experiments [16, 17, 18] with respect to the geometry (Rood wing), Reynolds number ($Re = 7{,}000$ based on freestream velocity and maximum profile thickness), approach flow BL properties (displacement and momentum thickness), and the wall heating. The mean flow in the symmetry plane ahead of the junction was found to be in good agreement with the PSU measurements.

The streamlines in the symmetry plane show a flattened horseshoe vortex (HV) as a result of a seemingly random back and forth motion of the HV that can be associated with the switching between the zero-flow and back-flow mode. The computed frequency of the mode switching based on the approach BL thickness is 0.11 and thus slightly outside the range $0.05 < f\delta/v_{in} < 0.1$ proposed by Gand et al. [21]. The variable-interval time-averaging method by Blackwelder and Kaplan [26] was employed to detect upstream BL events. The majority of the detected BL events were followed by a significant increase of the HV circulation. This observation is in agreement with Sabatino and Smith [15] who argue that "hairpin vortex packets" in the BL merge with and strengthen the HV and in disagreement with Escauriaza and Sotiropoulos [22] who argue that hairpin vortices wrap around and disorganize the HV.

Boundary layer events were forced with pulsed jets that were placed upstream of the leading edge. The jet location, forcing period, and blowing ratio as well as the number of jets were varied; The duty cycle was held constant at 4%. Downstream boundary layer events were detected with the VITA method by Blackwelder and Kaplan [26]. By computing the cross-correlation of the VITA value with the forcing signal, the effectiveness of the forcing could be quantified. The cross-correlation of the VITA value upstream of the interaction with the circulation of the HV was then computed to quantify the dependence of the junction flow behavior on the upstream boundary layer events. The strongest correlation between the junction flow behavior and the upstream boundary layer events was observed for a forcing period of 7.5 (which is close to the natural unsteadiness of the junction flow [25]) and a blowing ratio of 2 (both one and three jets). However, the correlation was relatively weak and more work needs to be done before conclusions can be drawn. In particular, the forcing of the boundary layer events has to be revisited and the simulations have to be continued to obtain longer time intervals for the analyses. A laminar Rood wing simulation with matched approach boundary layer momentum thickness but reduced Reynolds number of 1,000 was performed to investigate if the bimodal occurred for laminar interactions. For the laminar simulation, the junction flow did in fact become entirely steady. This does however not provide support for the argument that the bimodal behavior of turbulent junction flows is only a consequence of upstream boundary layer events and not related to an inherent instability of the junction flow. Finally, for the turbulent interaction at a Reynolds number of 7,000, the Rood wing geometry was filleted by adding a

DISTRIBUTION STATEMENT A. Approved for public release. Distribution is unlimited.

circular radius of 10% and 20% chord at the Rood wing endwall junction. In agreement with Devenport et al. [28], the fillets were found to suppress the bimodal behavior and reduce the junction flow unsteadiness.

DISTRIBUTION STATEMENT A. Approved for public release. Distribution is unlimited.

8 ACKNOWLEDGMENTS

High Performance Computing (HPC) resources were provided by the Department of Defense HPC Modernization Program.

DISTRIBUTION STATEMENT A. Approved for public release. Distribution is unlimited.

9 STUDENTS SUPPORTED BY GRANT

- Zachary Robison, New Mexico State University, Ph.D. student since 01/2017
- John-Paul Mosele, New Mexico State University, M.S. student since 08/2018

DISTRIBUTION STATEMENT A. Approved for public release. Distribution is unlimited.

10 PUBLICATIONS RESULTING FROM GRANT

10.1 Conference Publications (Attached)

- Robison, Z., Mosele J.-P., and Gross, A."Numerical Simulations of Turbulent Junction Flow with Upstream Disturbances," AIAA-2019-3714, AIAA Aviation Forum, 15-19 2019, Dallas, TX.
- Gross, A. and Robison Z., "Numerical Simulations of Turbulent Junction Flow," AIAA-2018-3866, AIAA Aviation Forum, 25-29 June 2018, Atlanta, GA.

10.2 Journal Publications

Two journal papers are in preparation.

DISTRIBUTION STATEMENT A. Approved for public release. Distribution is unlimited.

NOMENCLATURE

a_i	POD time coefficient
A_{ref}	Reference area
B	Blowing ratio
c	Chord length
c_f	Skin-friction coefficient
c_p	Pressure coefficient
C_{ax}	Axial chord length
c	Momentum coefficient
f	Frequency
FSTI	Inlet turbulence intensity, $\sqrt{\frac{2k}{3}}/v_{in}$
i, j, k	Azimuthal, radial and spanwise cell indices
H	Shape factor
k	Turbulent kinetic energy
l_T	Integral turbulence length scale
L	Length scale
M	Mach number
p	Static pressure
P r	Prandtl number
q	Dynamic pressure, heat flux, POD mode
Q	Vortex identification criterion
Re	Reynolds number
s_{ij}	Strain rate tensor
St	Stanton number
t	Time, airfoil maximum thickness
T	Temperature, period
u, v, w	Axial, pitchwise and spanwise velocity components
U, V, W	Mean flow velocity components
v	Velocity vector
V	Cell volume
x, y, z	Axial, pitchwise and spanwise coordinates
x	Coordinate vector
x_c	Streamwise core position
z_c	Spanwise core position
δ	Boundary layer thickness
δ^*	Displacement thickness
λ	POD eigenvalue
μ	Dynamic viscosity
u_τ	Friction velocity
ν	Kinematic viscosity
ρ	Density
τ	Friction, time coefficient, duty cycle
ε	Turbulent dissipation rate

DISTRIBUTION STATEMENT A. Approved for public release. Distribution is unlimited.

ϑ	Momentum thickness
ω	Vorticity

Subscripts

0	Inflow, stagnation conditions
2D	Two-dimensional
av	average
i	Mode number
in	Inlet condition
ref	Reference
RMS	Root mean square
T	Turbulent
w	At the wall
1	Freestream condition

Superscripts

+	In wall units
*	Dimensional quantity

Acronyms

2-D	Two-Dimensional
3-D	Three-Dimensional
AFOSR	Air Force Office of Scientific Research
AFRL	Air Force Research Laboratory
BL	Boundary Layer
CFD	Computational Fluid Dynamics
DNS	Direct Numerical Simulation
F1	Fillet 1 Case, r/t=0.1
F2	Fillet 2 Case, r/t=0.2
FSTI	Free Stream Turbulence Intensity
HPC	High Performance Computing
HV	Horseshoe Vortex
LDV	Laser Doppler velocimetry
ILES	Implicit Large Eddy Simulation
LES	Large Eddy Simulation
LPT	Low Pressure Turbine
LSWT	Low Speed Wind Tunnel
NF	No Fillet Case
NMSU	New Mexico State University
PIV	Particle Image Velocimetry
POD	Proper Orthogonal Decomposition

DISTRIBUTION STATEMENT A. Approved for public release. Distribution is unlimited.

PSU Penn State University
PV Passage Vortex
RANS Reynolds-Averaged Navier-Stokes
TKE Turbulent Kinetic Energy
VITA Variable interval time averaging
WALE Wall-Adapting Local Eddy-Viscosity
WENO Weighted Essentially Non-Oscillatory
WPAFB Wright-Patterson Air Force Base

DISTRIBUTION STATEMENT A. Approved for public release. Distribution is unlimited.

11 REFERENCES

[1] Lyall, M., Sondergaard, R., Mcquilling, M., Clark, J., and King, P., "An Investigation of Reynolds Lapse Rate for Highly Loaded Low Pressure Turbine Airfoils With Forward and Aft Loading." *Journal of Turbomachinery*, Vol. 134, No. 5, 2012, pp. 1-9

[2] Bear, P., Wolff, M., Gross, A., Marks, C.R., and Sondergaard, R., "Experimental Investigation of Total Pressure Loss Development in a Highly Loaded Low-Pressure Turbine Cascade," *Journal of Turbomachinery*, Vol. 140, No. 3, 2017, pp. 031003-1-9

[3] Devenport, W.J., and Simpson, R.L., "Time-Dependent and Time-Averaged Turbulence Structure Near the Nose of a Wing-Body Junction," *Journal of Fluid Mechanics*, Vol. 210, 1990, pp. 23-55

[4] Wang, H.-P., Olson, S.J., Goldstein, R.J., and Eckert, E.R.G., "Flow Visualization in a Linear Turbine Cascade of High Performance Turbine Blades," *Journal of Turbomachinery*, Vol. 119, No. 1, 1997, pp. 1-8

[5] Veley, E., Marks, C., Anthony, R., Sondergaard, R., Fletcher, N., and Wolff, M., "Unsteady Flow Mea-surements in a Low Pressure Turbine Passage using Surface Mounted Thin Film Sensors", *AIAA Paper* AIAA 2017-4825, 2017

[6] Veley, E., Marks, C., Anthony, R., Sondergaard, R., and Wolff, M., "Unsteady Flow Measurements in a Front Loaded Low Pressure Turbine Passage", *AIAA Paper* AIAA 2018-2124, 2018

[7] Fletcher, N., Marks, C., Petrie, R., Sondergaard, R., and Wolff, M., "Experimental Investigation of Endwall Flow Control for Front Loaded Turbine Blades", *AIAA Paper* AIAA 2018-4436, 2018

[8] Gross, A., Marks, C., and Sondergaard, R., "Numerical Investigation of Low-Pressure Turbine Junction Flow," *AIAA Journal*, Vol. 55, No. 10, 2016, pp. 3617-3621

[9] Mehta, R.D., "Effect of Wing Nose Shape on the Flow in a Wing Body Junction," *The Aeronautical Journal*, Vol. 88, No. 880, 1984, pp. 456-460

[10] Olcmen, S.M., and Simpson, R.L., "Influence of Wing Shapes on Surface Pressure Fluctuations at Wing-Body Junctions," *AIAA Journal*, Vol.32. No. 1, 1994, pp. 6-15

[11] Simpson, R.L., "Junction Flows," *Annual Review of Fluid Mechanics*, Vol. 33, 2001, pp. 415-443

[12] Agui, J.H., and Andreopoulos, J., "Experimental Investigation of a Three-Dimensional Boundary Layer Flow in the Vicinity of an Upright Wall Mounted Cylinder," *Journal of Fluids Engineering*, Vol. 114, No. 4, 1992, pp. 566-576

[13] Praisner, T.J., and Smith, C.R., "The Dynamics of the Horseshoe Vortex and Associated Endwall Heat Transfer-Part I: Temporal Behavior," *Journal of Turbomachinery*, Vol. 128, No. 4, 2006, pp. 747-754

DISTRIBUTION STATEMENT A. Approved for public release. Distribution is unlimited.

[14] Adrian, R. J., Meinhart, C. D., and Tomkins, C. D., "Vortex Organization in the Outer Region of the Turbulent Boundary Layer," University of Illinois at Urbana-Champaign Theoretical and Applied Mechanics Report No. 924, UILU-ENG-99-6026, 1999

[15] Sabatino, D.R., and Smith, C.R., "Boundary Layer Influence on the Unsteady Horseshoe Vortex Flow and Surface Heat Transfer," *Journal of Turbomachinery*, Vol. 131, No. 1, 2009, pp. 011015

[16] Elahi, S.S., Lange, E.A., and Lynch, S.P., "Experimental Measurements of Turbulent Junction Flow Using High Speed Stereo PIV and IR Thermography," *AIAA Paper*, AIAA-2017-3303, 2017

[18] Elahi, S.S., Moul, Z.K., Lange, E.A., and Lynch, S.P., "Unsteady Heat Flux Measurements of Junction Flow With Reynolds Number and Freestream Turbulence Effects," *AIAA Paper*, AIAA-2018-0358,20

[19] Lange, E.A., Elahi, S.S., and Lynch, S.P., "Time-resolved PIV Measurements of the Effect of Freestream Turbulence on Horseshoe Vortex Dynamics," *AIAA Paper*, AIAA-2018-0584, 2018

[20] Paik, J., Escauriaza, C., and Sotiropoulos, F., "On the Bimodal Dynamics of the Turbulent Horseshoe Vortex System in a Wing-Body Junction," *Physics of Fluids*, Vol. 19, No. 4, 2007, pp. 045107-1-20

[21] Allen, J.J., and Naitoh, T., "Scaling and instability of a junction vortex," *Journal of Fluid Mechanics*, Vol. 574, 2007, pp. 1-23

[22] Gand, F., Deck, S., Brunet, V., and Sagaut, P., "Flow Dynamics Past a Simplified Wing Body Junction," *Physics of Fluids*, Vol. 22, No. 11, 2010, pp. 115111-1-16

[23] Escauriaza, C., and Sotiropoulos, F., "Reynolds Number Effects on the Coherent Dynamics of the Tur-bulent Horseshoe Vortex System," *Flow, Turbulence, and Combustion*, Vol. 86, No. 2, 2011, pp. 231-262

[24] Schwänen, M., Meador, M., Camp, J., Jagannathan, S., and Duggleby, A., "Massively-Parallel DNS and LES of Turbine Vane Endwall Horseshoe Vortex Dynamics and Heat Transfer," Proc. ASME Turbo Expo, GT2011-45915, 2011

[25] Cui, J., Rao, V.N., and Tucker, P., "Numerical Investigation of Contrasting Flow Physics in Different Zones of a High-Lift Low-Pressure Turbine Blade," *Journal of Turbomachinery*, Vol. 138, No. 1, 2016, pp. 011003-1-10

[26] Gross, A., and Robison, Z., "Numerical Simulations of Turbulent Junction Flow," *AIAA Paper*, AIAA 2018-3866, 2018

[27] Blackwelder, R.F., and Kaplan, R.E., "On the wall structure of the turbulent boundary layer," *Journal of Fluid Mechanics*, Vol. 76, No. 1, 1976, pp. 89-112

[28] Smith, C.R., and Walker, J.D.A., "The Control of Junction Flows," Final report AFOSR grant no. F49620-93-1-0346, 1997

DISTRIBUTION STATEMENT A. Approved for public release. Distribution is unlimited.

[29] Devenport, W., Agarwal, N., Dewitz, M., and Simpson, R., "Effects of a leading edge fillet on the flow near and past an appendage body junction," *AIAA Journal*, Vol. 30, No. 9, 1992, pp. 2177-2183

[30] Johnson, M., Ravindra, K., and Andres, R., "Comparative study of the elimination of the wing fuselage junction vortex by boundary layer suction and blowing," *AIAA Paper*, AIAA-1994-293, 1994

[31] Seal, C. V., and Smith, C.R., "The control of turbulent endwall boundary layers using surface suction," *Experiments in Fluids*, Vol. 27, No. 6, 1999, pp. 484-496

[32] Olcmen, S.M., and Simpson, R.L., "Influence of Passive Flow-Control Devices on the Pressure Fluctuations at Wing-Body Junction Flows," *Journal of Fluids Engineering*, Vol. 129, No. 8, 2007, pp. 1030-1037

[33] Apsilidis, N., Diplas, P., Dancey, C.L., and Bouratsis, P., "Effects of wall roughness on turbulent junction flow characteristics," *Experiments in Fluids*, Vol. 57, No. 12, 2016, pp. 1-16

[34] Gross, A., and Fasel, H. F., "High-Order-Accurate Numerical Method for Complex Flows," *AIAA Journal*, Vol. 46, No. 1, 2008, pp. 204-214

[35] Gross, A., and Fasel, H., "Modification of Ninth-Order Weighted Essentially Nonoscillatory Scheme for Mixed Subsonic/Supersonic Flow," *AIAA Journal*, Vol. 48, No. 11, 2010, pp. 2698-2702

[36] Erlebacher, G., Hussaini, M.Y., Speziale, C.G., and Zang, T.A., "Toward the Large-Eddy Simulation of Compressible Turbulent Flows," NASA CR 187460, 1990

[37] Nicoud, F., and Ducros, F., " Subgrid-Scale Stress Modelling Based on the Square of the Velocity Gradient Tensor," *Flow, Turbulence and Combustion*, Vol. 62, No. 3, 1999, pp. 183-2

[38] Gross, A., and Fasel, H.F., 2008, "Multi-block Poisson grid generator for cascade simulations," *Mathematics and Computers in Simulation*, Vol. 79, No. 3, 2008, pp. 416-428

[39] Georgiadis, N.J., Rizzetta, D.P., and Fureby, C., "Large-Eddy Simulation: Current Capabilities, Recommended Practices, and Future Research," *AIAA Journal*, Vol. 48, No. 8, 2010, pp. 1772-1784

[40] Munters, W., Meneveau, C., and Meyers, J., "Shifted periodic boundary conditions for simulations of wall-bounded," *Physics of Fluids*, Vol. 28, 2016, pp. 025112-1-13

[41] Gross, A., and Fasel, H.F., "Characteristic Ghost-Cell Boundary Condition," *AIAA Journal*, Vol. 45, No. 1, 2007, pp. 302-306

[42] Lumley, J.L., "The Structure of Inhomogeneous Turbulent Flows," Atmospheric turbulence and radio wave propagation, Nauka, Moscow and Toulouse, France, eds. Yaglom and Tatarsky, 1967, pp. 166-178

DISTRIBUTION STATEMENT A. Approved for public release. Distribution is unlimited.

[43] Sirovich, L., "Turbulence and the dynamics of coherent structures, Part I-III," Quarterly of Applied Mathematics, Vol. 45, 1987, pp. 561-590

[44] Hunt, J.C.R., Wray, A.A., and Moin, P., "Eddies, stream, and convergence zones in turbulent Flows," Report CTR-S88, Center For Turbulence Research, Stanford, CA, 1988

[45] Hopkins, E.J., and Inouye, M., "An evaluation of theories for predicting turbulent skin friction and heat transfer on flat plates at supersonic and hypersonic Mach numbers," *AIAA Journal*, Vol. 9, No. 6, 1971, pp. 993-1003

DISTRIBUTION STATEMENT A. Approved for public release. Distribution is unlimited.